

Paritosh Vasava

APPLICATION OF COMPUTATIONAL FLUID DYNAMICS IN MODELLING BLOOD FLOW IN HUMAN THORACIC AORTA

Thesis for the degree of Doctor of Science (Technology) to be presented with due permission for public examination and criticism in the Auditorium1383 at the Lappeenranta University of Technology, Lappeenranta, Finland on the 19th of December, 2011, at noon.

Acta Universitatis
Lappeenrantaensis 465

- Supervisor Associate Professor Payman Jalali
Laboratory of Engineering Thermodynamics
LUT Energy
Lappeenranta University of Technology
Finland
- Reviewers Professor Dr.-Ing habil. Dieter Liepsch
Laboratory of Fluid Mechanics
Faculty of Engineering (Faculty 05)
Munich University of Applied Sciences
Munich, Germany
- Professor Akira Nakayama
Department of Mechanical Engineering
Faculty of Engineering
Shizuoka University
Hamamatsu, Japan
- Opponent Professor Dr. Ir F. N. van de Vosse
Department of Mechanical Engineering
Eindhoven University of Technology
Eindhoven, The Netherlands

ISBN 978-952-265-196-9
ISBN 978-952-265-197-6 (PDF)
ISSN 1456-4491
Lappeenranta teknillinen yliopisto
Digipaino 2011

Abstract

Paritosh R. Vasava

Application of Computational Fluid Dynamics in Modeling Blood Flow in Human Thoracic Aorta

Lappeenranta 2011

117 pages

Acta Universitatis Lappeenrantaensis 465

Diss. Lappeenranta University of Technology

ISBN 978-952-265-196-9, ISBN 978-952-265-197-6 (PDF), ISSN 1456-4491

The aim of this study was to simulate blood flow in thoracic human aorta and understand the role of flow dynamics in the initialization and localization of atherosclerotic plaque in human thoracic aorta. The blood flow dynamics in idealized and realistic models of human thoracic aorta were numerically simulated in three idealized and two realistic thoracic aorta models. The idealized models of thoracic aorta were reconstructed with measurements available from literature, and the realistic models of thoracic aorta were constructed by image processing Computed Tomographic (CT) images. The CT images were made available by South Karelia Central Hospital in Lappeenranta. The reconstruction of thoracic aorta consisted of operations, such as contrast adjustment, image segmentations, and 3D surface rendering. Additional design operations were performed to make the aorta model compatible for the numerical method based computer code. The image processing and design operations were performed with specialized medical image processing software. Pulsatile pressure and velocity boundary conditions were deployed as inlet boundary conditions. The blood flow was assumed homogeneous and incompressible. The blood was assumed to be a Newtonian fluid. The simulations with idealized models of thoracic aorta were carried out with Finite Element Method based computer code, while the simulations with realistic models of thoracic aorta were carried out with Finite Volume Method based computer code. Simulations were carried out for four cardiac cycles. The distribution of flow, pressure and Wall Shear Stress (WSS) observed during the fourth cardiac cycle were extensively analyzed.

The aim of carrying out the simulations with idealized model was to get an estimate of flow dynamics in a realistic aorta model. The motive behind the choice of three aorta models with distinct features was to understand the dependence of flow dynamics on aorta anatomy. Highly disturbed and non-uniform distribution of velocity and WSS was observed in aortic arch, near brachiocephalic, left common artery, and left subclavian artery. On the other hand, the WSS profiles at the roots of branches show significant differences with

geometry variation of aorta and branches. The comparison of instantaneous WSS profiles revealed that the model with straight branching arteries had relatively lower WSS compared to that in the aorta model with curved branches. In addition to this, significant differences were observed in the spatial and temporal profiles of WSS, flow, and pressure. The study with idealized model was extended to study blood flow in thoracic aorta under the effects of hypertension and hypotension. One of the idealized aorta models was modified along with the boundary conditions to mimic the thoracic aorta under the effects of hypertension and hypotension.

The results of simulations with realistic models extracted from CT scans demonstrated more realistic flow dynamics than that in the idealized models. During systole, the velocity in ascending aorta was skewed towards the outer wall of aortic arch. The flow develops secondary flow patterns as it moves downstream towards aortic arch. Unlike idealized models, the distribution of flow was non-planar and heavily guided by the artery anatomy. Flow cavitation was observed in the aorta model which was imaged giving longer branches. This could not be properly observed in the model with imaging containing a shorter length for aortic branches. The flow circulation was also observed in the inner wall of the aortic arch. However, during the diastole, the flow profiles were almost flat and regular due the acceleration of flow at the inlet. The flow profiles were weakly turbulent during the flow reversal. The complex flow patterns caused a non-uniform distribution of WSS. High WSS was distributed at the junction of branches and aortic arch. Low WSS was distributed at the proximal part of the junction, while intermedium WSS was distributed in the distal part of the junction. The pulsatile nature of the inflow caused oscillating WSS at the branch entry region and inner curvature of aortic arch. Based on the WSS distribution in the realistic model, one of the aorta models was altered to induce artificial atherosclerotic plaque at the branch entry region and inner curvature of aortic arch. Atherosclerotic plaque causing 50% blockage of lumen was introduced in brachiocephalic artery, common carotid artery, left subclavian artery, and aortic arch. The aim of this part of the study was first to study the effect of stenosis on flow and WSS distribution, understand the effect of shape of atherosclerotic plaque on flow and WSS distribution, and finally to investigate the effect of lumen blockage severity on flow and WSS distributions. The results revealed that the distribution of WSS is significantly affected by plaque with mere 50% stenosis. The asymmetric shape of stenosis causes higher WSS in branching arteries than in the cases with symmetric plaque.

The flow dynamics within thoracic aorta models has been extensively studied and reported here. The effects of pressure and arterial anatomy on the flow dynamic were investigated. The distribution of complex flow and WSS is correlated with

the localization of atherosclerosis. With the available results we can conclude that the thoracic aorta, with complex anatomy is the most vulnerable artery for the localization and development of atherosclerosis. The flow dynamics and arterial anatomy play a role in the localization of atherosclerosis. The patient specific image based models can be used to diagnose the locations in the aorta vulnerable to the development of arterial diseases such as atherosclerosis.

Keywords: CFD Simulations, Thoracic Aorta, Atherosclerosis, Shear Stress, Hypotension, Hypertension, Artery anatomy

UDC: 004.94:611.1:519.62/.64

Acknowledgements

The reported study was carried out at the Laboratory of Engineering Thermodynamics, Department of Energy and Environmental Technology at Lappeenranta University of Technology, Finland.

I would like to express my sincere gratitude to my supervisor Dr. Payman Jalali for introducing me to the topic and providing an opportunity to work in the area of Biomedical Engineering. I am also very grateful to my scientific instructor Dr. Mahsa Dabagh for her constant help and encouragement. Thank you for providing fundamental understanding of this study. I would also like to thank Dr. Tero Tynjälä for administrative help and support.

I am grateful for Prof. Liepsch (Munich University of Applied Sciences) and Prof. Nakayama (Shizuoka University) for reviewing and evaluating the thesis. Their valuable suggestions and comments helped in improving the manuscript.

This work was supported and funded by The Finnish Graduate School of Computational Fluid Dynamics (Laskennallisen Virtausmekaniikan Tutkijakoulu) and Academy of Finland (Grant No. 123938). I would also like to acknowledge financial support provided by LUT's research foundation Tukisäätiö during the finalization of the manuscript.

The medical data used in the study were obtained and used in accordance with the regulations set by the ethical committee of Lappeenranta University of Technology. The CT images used in this study were provided by the Radiology Department of the South Karelia Central Hospital in Lappeenranta. I would like to thank Senior Radiologist Dr. Matti Sauna-Aho for his help in obtaining the CT images and Mr. Pertti Kolari for administrative support for acquiring CT images. I would also like to thank Adam Klodowski (Department of Mechanical Engineering, LUT) and Adam Raczynski (Technical University of Lodz, Poland) for their guidance about CAD programs which made the use of realistic aorta models possible. The IT Center of Science-CSC provided computational code and computational recourses for some part of this study.

Thanks to my friends Arjun, Ashvin, Ehsan, Markku, Pani, Pekka, Safoora and Zuned who have encouraged me and uplifted my spirit when I was down. I would like to convey very special regards to Taisto and Eira.

Finally, none of these would have been possible without the support and love of my parents: Rasikbhai and Kapilaben Vasava. I express my deepest gratitude for being backbone of my life, educating and encouraging me to pursue my interests, even when it took me beyond boundaries of language, field and geography. Very special thanks to my lovely wife Hetal for her unconditional love, understanding and support.

Paritosh R. Vasava
December 2011
Lappeenranta, Finland

Be not ashamed of mistakes and thus make them crimes.
-Confucius

Contents

Abstract

Acknowledgements

Contents

List of publications	13
Nomenclature	15
1 Introduction	17
1.1 Pathogenesis and Localization of Atherosclerosis	17
1.2 Atherosclerosis in Human Aorta	19
1.3 Simulation of Blood Flow in Human Aorta	20
1.4 Objectives and Organization of the Thesis	23
1.5 Author's Contribution.....	24
1.6 Limitations of the Study	25
2 Reconstruction of Idealized and Realistic Models of Human Aorta	26
2.1 Reconstruction of Idealized Aorta Models	26
2.1.1 Idealized Aorta Model-1	26
2.1.2 Idealized Aorta Model-2	28
2.1.3 Idealized Aorta Model-3	28
2.1.4 Idealized Aorta Model-3 under hypotension and hypertension ..	29
2.2 Reconstruction of Realistic Human Aorta Model from CT Images	30
2.2.1 Computed Tomography Images	30
2.2.2 Image processing of CT Images	31
2.2.3 3D surface rendering and other CAD operations	34
2.2.4 Realistic Aorta Model-1	35
2.2.5 Realistic Aorta Model-2	37
3 Simulation Methodology	39
3.1 Mesh Grid for FEM and FVM Solvers.....	39
3.2 Physical Properties of Blood	39
3.3 Boundary conditions.....	40
3.3.1 Pressure Inlet Boundary conditions.....	40
3.3.2 Velocity Inlet Boundary conditions	41
3.3.3 Outlet Boundary conditions.....	42
3.4 Flow governing equations	44

3.5	FEM Based Solver.....	44
3.5.1	FEM Based Solver Setup	44
3.5.2	FVM Based Solver	45
4	Results from Idealized Models of Aorta	47
4.1	Distribution of Pressure in Idealized Aorta Models	47
4.1.1	Effect of Hypotension and Hypertension on the Distribution of Pressure in Idealized Aorta Models.....	48
4.2	Flow Distribution in Aorta Models	49
4.2.1	Effect of Hypotension and Hypertension on Flow Distribution in the Idealized Aorta Model G3	52
4.3	Distribution of WSS in Idealized Aorta Models	54
4.3.1	Effect of Hypotension and Hypertension on the Distribution of WSS in the Aorta Model G3	57
4.4	Discussion.....	61
5	Results from Realistic Models of Aorta	64
5.1	Results from Realistic Aorta Model-1	64
5.1.1	Velocity Distribution in Realistic Aorta Model-1	64
5.1.2	Pressure Distribution in Realistic Aorta Model-1	68
5.1.3	WSS Distribution in Realistic Aorta Model-1	69
5.2	Results from Realistic Aorta Model-2	72
5.2.1	Velocity Distribution in Realistic Aorta Model-2	72
5.2.2	Pressure Distribution in Realistic Aorta Model-2	75
5.2.3	WSS Distribution in Realistic Aorta Model-2	76
5.3	Discussion.....	78
6	Results from Thoracic Aorta Models with Artificial Stenosis	82
6.1	Atherosclerotic plaque in aortic arch and branches	82
6.2	Distribution of WSS in Aorta with Symmetric Stenosis in Branches	85
6.3	Distribution of WSS in Aorta with Asymmetric Stenosis in Branches	90
6.4	Effect of Stenosis Severity on Distribution of WSS.....	93
6.5	Distribution of WSS in Aorta Model with Stenosis in Aortic Arch	99
6.6	Discussion.....	102
7	Conclusions and Discussion	104
8	Future Work and Suggestions	109
	References	111

List of publications

This monograph contains unpublished material. During the course of the study two journal articles and five conference articles were published by the candidate. Some parts of the monograph refer to earlier published works for purpose of comparison or explanations. Following is the list of journal and conference articles published by the candidate.

Published Scientific Journal Articles

- I. Paritosh Vasava, Payman Jalali, Mahsa Dabagh, Pertti Kolari, 2011. Finite Element Modeling of pulsatile blood flow in idealized model of human aortic arch: The study of hypotension and hypertension, Computational and Mathematical Methods in Medicine, *Article in the press*.

Submitted Scientific Journal Articles

- II. Mahsa Dabagh, Paritosh Vasava, Matti Sauna-Aho, Payman Jalali, 2012. Hemodynamics in human aorta with the severity and location of stenosis. Journal of Biomechanics.

Refereed Conference Articles

- III. Vasava, P., Dabagh, M., Jalali, P., 2008. Pulsatile blood flow simulations in aortic arch: Effects of blood pressure and the geometry of arch on wall shear stress. IFMBE proceedings, 22, 1926-1929.
- IV. Vasava, P., Dabagh, M., Jalali, P., 2009. Effect of aortic arch geometry on pulsatile blood flow: Flow pattern and wall shear stress. IFMBE proceedings, 25, 1198-1201.
- V. Vasava, P., Dabagh, M., Jalali, P., 2009. Computational study of pulsatile blood flow in aortic arch: Effect of blood pressure. IFMBE proceedings, 25, 1206-1209.

Other Conference Articles

- VI. Paritosh Vasava, Zuned Mansuri, Payman Jalali, Mahsa Dabagh, Computational fluid dynamics simulations of pulsatile blood flow in human aortic arch reconstructed from computed tomographic images: Study of flow profiles and wall shear stress, 23rd European Conference on Biomaterials (ESB 2010), 11-15 September 2010, Tampere, Finland.

- VII. P. Vasava, P. Jalali, M. Dabagh, Simulation of Blood Flow in CT Image Based Models of Human Aortic Arch with Normal and Stenosed Branches: Study of Velocity and Local Wall Shear Stress, 6th international symposium on Biomechanics in Vascular Biology and Cardiovascular Disease. April 14-15, 2011, Rotterdam, The Netherlands.

Author's contribution to publication and relation to the manuscript

The research work reported in this monograph and published articles were conducted in three parts. The first part consisted of experiments with three idealized models of the human aorta. Publications I, III, IV and V are based on the first part of the research work. The second part consisted of experiments with two CT image based models of the human aorta. Publications VI and VII are based on the second part of the research work. The third part consisted of experiments with CT image based models of aorta with artificial stenosis introduced at the branch entry regions of three major branches. Publications II and VII are based on the third part of the research work.

The numerical simulations reported in publication I, II, IV-VII were performed by the candidate.

The image processing and CAD operations for the CT image based models of the aorta used in publications II, VI and VII were performed by the candidate.

The candidate wrote parts of the manuscript for publications I, III-VII with Dr. Payman Jalali and Dr. Mahsa Dabagh.

Nomenclature

Latin alphabet

3D	Three Dimensional	
C	Coefficient of the pressure pulse	-
D_{before}	Diameters of artery before and after stenosis	-
D_{after}	Diameters of artery before and after stenosis	-
G1	Idealized Thoracic Aorta model-1	-
G2	Idealized Thoracic Aorta model-2	-
G3	Idealized Thoracic Aorta model-3	-
R1	Realistic Thoracic Aorta model-1	-
R2	Realistic Thoracic Aorta model-2	-
A	Area	m^2
p	Pressure	Pa
u	Velocity vector	m/s
t	Time	s
m	Total number of small surfaces	-
k	Total number of images in a DICOM stack	-
n	Total number of cardiac cycles	-

Greek alphabet

ρ	Density	kg/m^3
μ	Viscosity	Pa·s

Subscripts

i	Number of cardiac cycle	-
j	image in the DICOM stack	-

1 Introduction

Human cardiovascular system consists of heart, arteries, and veins. The diseases of heart, arteries, and veins are classified as Cardiovascular Diseases (CVDs) which are the major cause of deaths in Europe, United States of America, and also some developing countries today. According to a prediction by World Health Organization (WHO), by year 2030 approximately 24 million people will die from CVDs. The major risks influencing CVDs include high blood pressure, diabetes, obesity, smoking, excessive use of alcohol, abnormal blood lipids, and inadequate exercise. Continuous exposure to these risk factors may increase the risk of CVDs and may lead to faster growth of the diseases. CVDs can be avoided by modifications in life style and diets. However, the cure for some of the CVDs is still under active research.

1.1 Pathogenesis and Localization of Atherosclerosis

Ischemic heart disease and coronary arterial disease are amongst the most common CVDs which are caused by the disruption in the blood supply due to narrowed or hardened arteries, commonly referred as atherosclerosis. Atherosclerosis is a progressive arterial disease characterized by the building of fatty plaque within arterial walls. The most accepted hypothesis about pathogenesis of atherosclerosis is that it develops as a response to the injury of endothelium. Atherosclerosis is primarily believed to be a chronic inflammatory response against harmful factors acting on the vascular wall.

An artery wall consists of several layers. The endothelium is the innermost layer of an artery and known to play an important role in regulating blood flow and is also known to have only selected permeability towards lipids and blood cells. Atherosclerosis begins when the endothelium of an artery is injured or damaged. The injury of endothelium is often referred as endothelium dysfunction. The endothelium dysfunction results in the increased permeability of endothelium. The damaged endothelium allows fats, cholesterol, macrophages, and other cellular material to pass through it. The accumulation of these materials through the permeable endothelium stimulates complex reactions within the tunica intima and tunica medial layers of the artery wall. The reactions involve endothelial cells, blood platelets, monocytes (which are activated after penetrating endothelium), macrophages, and smooth muscle cells. As a result of these complex reactions, a fatty plaque (also referred as Atherosclerotic plaque) is built within the arterial wall. The atherosclerotic plaque contains a fibrous cap and a lipid-rich core. The growing atherosclerotic plaque within the artery reduces the arterial lumen and causes irregular supply of blood, oxygen, and vital nutrients. The plaque within

the artery walls gradually calcifies and hardens the artery walls. This may lead to the stiffening of the artery and loss of elasticity of artery walls. On the other hand, the plaque is also known to be unstable and liable to rupture, leading to thrombosis. The atherosclerosis primarily affects elastic arteries. It is common in the aorta including the aortic arch and descending aorta, carotid arteries, iliac arteries, and renal arteries.

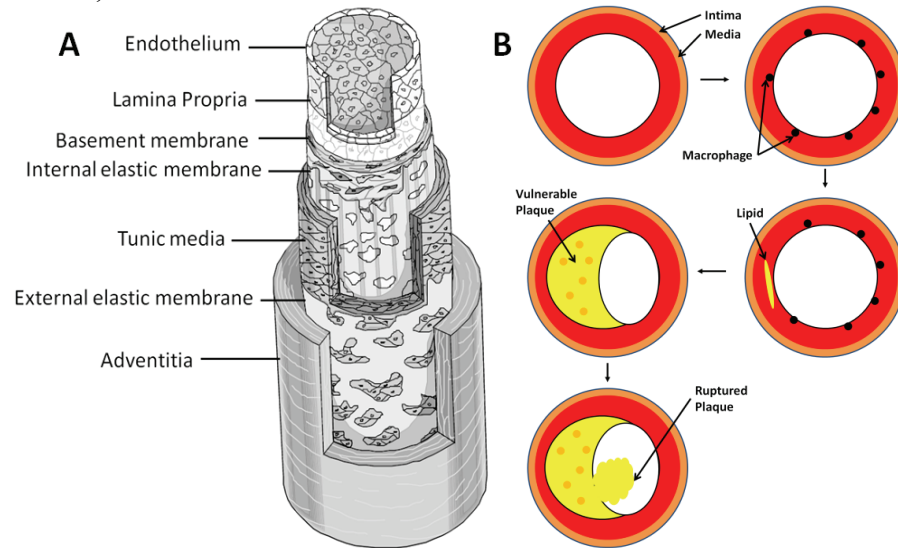


Figure 1.1: (A) Diagrams of typical artery wall with layers of tissues and, (B) schematic diagram illustrating the progress of atherosclerosis in a typical artery.

The atherosclerosis is known to be triggered by the endothelium. There is evidence that altered flow dynamics leads to endothelial dysfunction. Wall Shear Stress (WSS) which is the force applied by flowing fluid on the boundary, is known to stimulate the endothelial cells. Fry (1968) deduced that endothelial surface deteriorates when exposed to a variable velocity field. Later in 1969, Fry showed that the exposure to pressure and stress may increase the permeability of endothelium layer. Caro et al. (1969) revealed that the complex arterial flow mechanics promote the development of early atherosclerosis. In this work, it was deduced that the early development of atherosclerosis is localized in areas with locally low shear stress. In his review of influence of fluid mechanics in blood vessels, Texon (1972) blamed low pressure, increased shear stress, and increased velocity gradient as cause for localization of atherosclerosis. Leveseque et al. (1986) showed that the shape of endothelial cells is altered in response to changes in local shear stress distributions. In region with high wall the endothelial cells are elongated and aligned in the direction of the flow, while the arrangement of polygonal endothelial cells is haphazard. Liepsch et al. (1988) studied blood flow in true-to-scale silicon model of dog aorta. The experimental study revealed that

even minor modification in wall shear stress distribution has significant influence on the orientation of the endothelial cells. Asakura and Karino (1990) postulated that the alteration in the alignment of endothelial cells may influence the permeability of the endothelial layer for the lipoprotein particles. Gibson (1993) also determined significant correlation between low shear stress and increased rate of atherosclerosis in coronary artery. Thus, there is sufficient evidence that the localization of atherosclerosis is correlated with complex flow dynamics, especially with low and oscillating shear stress.

1.2 Atherosclerosis in Human Aorta

The atherosclerosis lesions tend to localize in certain regions of an artery, e.g. curvature, bifurcation, and tapering. Caro et al. (1969) and later DeBaakey et al. (1984) categorized coronary arterial bed, major branches of aortic arch, abdominal aorta, celiac arteries, and renal arteries as the most susceptible sites for the localization of atherosclerosis. Based on these studies, the human aorta may be considered as one of the most vulnerable arteries for the occurrence of atherosclerosis, mostly because of the specific geometry of the aorta highlighting the effect of the fluid dynamics in the creation of the atherosclerosis.

Mitchell and Schwartz (1965) shown that the atherosclerotic plaque in arteries is localized in the region with low Wall Shear Stress (WSS). Under an acute elevation of shear stress, the endothelial layer of arterial wall may damage and increase its permeability for lipids (Fry 1968 and 1969). The atherosclerosis lesion may also develop in regions where average WSS is low and fluctuating during the cardiac cycle (Caro et al. 1971). Seed and Wood (1971) observed secondary flow patterns in the axial sections of aorta of a dog, using hot film in their experiments. Later, Friedman 1983 observed helical and retrograde types of flow patterns prevailing in the human aorta arch. In both of the studies, the curvature of the aortic arch was thought to be the reason for the helical nature of the flow in aorta. Thus, besides hemodynamics, arterial anatomy also plays a role in the localization of atherosclerosis lesions. Utepov (1997) demonstrated that the tapering of descending aorta is correlated with the deposition of atherosclerosis lesions in the descending aorta. The occurrence of atherosclerosis lesions in certain geometric configurations indicates the influence of flow distribution and WSS. Therefore, the association of arterial diseases with altered fluid dynamics highlights the role of the blood flow in the localization of atherosclerosis.

The local anatomy of artery significantly influences the local hemodynamics and plays a role in the initialization and localization of the atherosclerosis.

1.3 Simulation of Blood Flow in Human Aorta

Aorta is the largest in human body which extends from the left ventricle of heart and runs through the lower abdominal region where it branches into iliac arteries. Other branches of the aorta supply blood to important organs, e.g. renal arteries supply blood to kidneys and the branches in aortic arch supply blood to brain and arms. Being the first artery from heart and also the largest artery in the human body, it plays a very important role in supplying blood and oxygen to organs and other organ systems. Aorta is also the artery with the most complex anatomy amongst all the arteries. Aorta has curvature in aortic arch, several large and mid-sized branches, tapering of lumen, and hyper elastic arterial walls. The complex anatomy of aorta causes complex patterns of blood flow inside it. The earlier studies have established that atherosclerosis is prone to develop in arteries with complex anatomies and hemodynamics. Therefore, the aorta with complex anatomy is thought to be one of the most vulnerable arteries for the occurrence of atherosclerosis. It has also been shown that the dynamics of the blood flow and the distribution of shear forces heavily depend on the local and global anatomy of arteries. Thus, the use of realistic models close to actual arteries has been emphasized and encouraged by many studies.

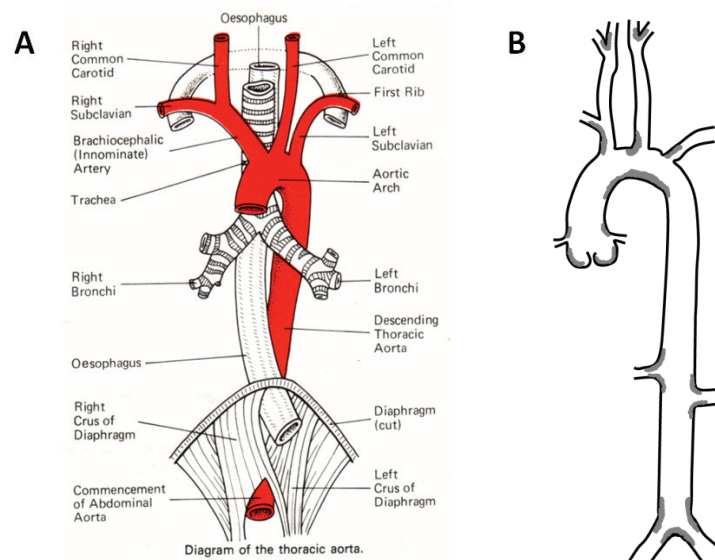


Figure 1.2: (A) labeled diagram of human thoracic aorta¹, and (B) sites in thoracic aorta (marked with gray) vulnerable to the localization of atherosclerotic plaque.

¹ With permission from www.arthurcliparts.org.

Blood flow dynamics have been under active research for several decades. Over the time, several studies about blood flow in arteries have been conducted theoretically (Kamiya and Togawa 1972, Zamir 1976, Avolio 1980, Van De Vosse 2003), experimentally (Padmanabhan 1984, Liepsch 1986a, Liepsch 1986b, Khodadari 1988, Gharib and Beizaie 2003, Lu et al. 2003, Matthys et al. 2007, and Pekkan et al. 2008), and numerically (Khodadari 1988, Shahcheraghi et al. 2002, Kim et al. 2004, Mori et al. 2002, Morris et al. 2005, Kim et al. 2009, Liu et al. 2010, Wen et al. 2010, Zhou et al. 2010). In earlier years when computational codes were not available, mathematical modeling and laboratory experiments were widely used to study blood flow. While the theoretical works were quantitative and based on fundamental physics and mathematics principles, the experimental works were laboratory experiments performed with the replicas of arteries. The mathematical modeling also included solving simplified flow equations in 2D and 3D cylindrical domains. The mathematical modeling gave useful information on the general flow behavior and quantities like compliance of an artery. However, it failed to reveal vital details on the local flow dynamics. The laboratory experiments conducted with the replica of arteries provided more details of flow dynamics inside the arteries. However, conducting these experiments required accurate settings of apparatus and conducting such experiments could be expensive, as well. The numerical methods based Computational Fluid Dynamics (CFD) packages have proved to be resourceful in providing accurate details of local and general flow dynamics, although they require heavy computational power to obtain accurate details. In the absence of computer based codes, simplified flow equations were solved in simplified artery models, e.g. straight or 180 curved pipe. Over the time period there has been significant development in CFD codes in terms of accuracy and capability of handling complex geometries. Hoogstraten et al. (1996) conducted numerical simulations with an idealized model of femoral artery with two successive bends. The computational codes and the computers at that point of time were not fast, and thus compromises had to be made in terms of mesh elements and blood flow models. This limitation of computational power restricted the work of Hoogstraten et al. (1996) to only steady state numerical simulations with mere 6000 mesh elements. Later, Ishikawa et al. (1998) studied the effect of non-Newtonian properties of blood in an idealized axisymmetric model of a stenosed artery with 7000 mesh elements. In the same year, Taylor et al. (1998) performed a time dependent finite element simulation of blood flow in an idealized model of descending aorta of human. While the experiments of Hoogstraten et al. (1996) were steady state with a coarse grid, Taylor et al. solved time dependent equations with a very fine mesh grid with almost 270000 elements.

The significant improvements in CFD codes have enabled researchers to obtain more accurate and reliable results and allowed the use of complex and realistic

artery models for numerical simulations. Earlier works have shown that the dynamics of the blood flow and distribution of shear forces heavily depend on the local and global anatomy of arteries. Thus, the use of realistic and detailed models of arteries have been emphasized and encouraged by many studies. Earlier the use of medical imaging techniques such as X-ray, Magnetic Resonance (MR), and CT were limited to the diagnosis with visual assessment. Since late 1990's, the number of studies based on medical imaging has increased significantly. Today, medical imaging is considered as one of the most prominent application fields of image processing. Some of the principles of image processing have also been extended to medical images. As a result, commercial medical image processing codes such as 3D-Doctor and Mimics are available today. Such medical image processing codes can process medical images and produce exact 3D models of internal organs. With the help of any Computer Aided Design (CAD) software, the 3D models can be made compatible with CFD codes. Such an application has already been successfully used to conduct a structural analysis of bones.

The improved capabilities of CFD codes have allowed the use of realistic models of arteries in several CFD based studies. Zhao et al. (2000) was amongst the first studies where a realistic model of an artery reconstructed from MRI angiogram was used to simulate pulsatile blood flow. As a result, the flow dynamics were more realistic in comparison to the earlier works with idealized models. Mori et al. (2002) used CT image based aortic arch model to simulate blood flow. Later, Morris et al. 2005 used the same model of aortic arch without branching arteries to study the effect of geometry on flow dynamics. Shacheraghi et al. (2002) simulated blood flow in human aortic arch using aorta model based on CT images, although the model had a uniform area of cross-section. In reality, the arteries are neither planar nor symmetric. The major cause of complex flow dynamics in the arteries is the complex anatomy.

Along with the realistic artery models, researchers are now also focusing on including more complex conditions in the simulations. Park et al. 2007 used pseudo organ type of a boundary condition to mimic the interaction between arteries and organs. Lee et al. (2008) used Direct Numerical Simulation (DNS) to simulate the blood flow in carotid bifurcation. DNS is known to be expensive in terms of time and computational resources, but it can provide very accurate results. Kim et al. (2009) simulated the blood flow in aortic arch using CFD techniques coupled with the lumped parameter model of heart. Liu et al. 2010 studied the effect of spiral flow on the transport of oxygen through the artery walls with different models of aortic arch. Today, CFD codes are playing an important role in the study of dynamics of blood flow in arteries. Due to the increased computational power and higher reliability, more accurate results can be obtained with the use of CFD codes.

The aim of the present study is to investigate the dynamics of the blood flow through the thoracic aorta with CFD codes. This study will help to understand the role of the flow dynamics in creation and localization of atherosclerosis.

1.4 Objectives and Organization of the Thesis

The numerical simulations of a pulsatile blood flow in the thoracic aorta of human and the results obtained are reported in this thesis consisting of six chapters. The thesis begins with the introduction to arterial diseases and a brief history of related works. The introduction chapter concludes with a brief summary of numerical simulations with idealized and realistic aortic arch models.

The introduction is followed by Chapter 2 which describes the reconstruction of thoracic aorta models. Five aorta models were used in this study. Three models were idealized aorta models and reconstructed from the measurements from literature. Two other aorta models were constructed from CT images. Chapter 2 begins with sub-sections describing idealized aorta models. This is followed by a brief description of image processing and Computer Aided Design (CAD) operations. The Chapter concluded with comments on the accuracy of results obtained with the use of a realistic model of aorta. Chapter 2 is followed by Chapter 3 which contains the details of simulation methodology for numerical simulations. The chapter begins with the description of the mesh grid used for numerical simulations. The physical properties of blood and boundary conditions deployed at inlet and outlet are discussed then. Then, the governing equations for blood flow are described briefly. The chapter concludes with the description of Finite Element Method (FEM) and Finite Volume Method (FVM) based solvers.

The results obtained from the blood flow simulations with FEM and FVM based solvers are discussed in Chapters 4 and 5, respectively. Chapter 4 contains sub-sections on the distribution of pressure, flow, and WSS in three idealized aorta models. Each of these sections consists of sub-sections on the effect of pressure, flow, and WSS, respectively. The chapter concludes with discussion on the effect of aorta anatomy and pressure on flow dynamics. Chapter 5 contains two main sub-sections containing results from two realistic aorta models respectively. Each of these sections is divided into three sub-sections about the distribution of velocity, pressure, and WSS in the idealized aorta models. The chapter concludes with discussion on differences in flow dynamics due to differences in the anatomy of aorta models.

The thesis concludes chapters with conclusions and future work. The conclusion chapter summarizes the study. The numerical simulations and results obtained

from the study are reviewed in this chapter. The significance of the work and suggestions for future work are discussed in the last chapter.

1.5 Author's Contribution

In recent years, biomedical engineering has emerged as one of the leading research disciplines. In this engineering field, fundamental engineering principles are used to understand the physiological phenomena, e.g. blood flow in large arteries and air flow in lungs. Biomedical engineering is highly interdisciplinary and it requires expertise from several engineering disciplines.

The main aim of the presented research is to understand the blood flow in human thoracic aorta and investigate the role of flow dynamics in the localization and development of atherosclerosis. The analysis of blood flow in large arteries will provide a better understanding of mechanism of development of arterial diseases. The computational investigation of blood flow in idealized geometries of human aortic arch has been carried out and results from these investigations have been reported in this thesis. These investigations have helped us understand the behavior of the blood flow in aortic arch. In order to increase the accuracy and reliability of the computational results, we used CT or MRI scans to feed our computational study. The radiology department of the South Karelian hospital at Lappeenranta has already provided us with three sets of CT scan images. The availability of a CT scan and other radiological data will enhance co-operation between Lappeenranta University of Technology and South Karelian hospital in expanding the research into a wider range of biomedical applications while a more clinical usage of results can be possible as well. The use of CT or MRI images will benefit physicians and researchers in performing patient-specific data analysis. For example, with a patient-specific geometry we can assess the risk of development of an arterial disease such as aneurysm or atherosclerosis. As the CT scans will allow us to look into the local details of arterial wall surface, the usage of CT data will significantly improve the quality of results obtained from computational software. The computational results with the use of CT data will be more reliable and accurate. In summary, the major contribution of the author in the current thesis was to create a bridge between medical imaging available clinically and the CFD software, in order to perform a detailed analysis of blood flow in arteries which was linked to the risk of the development of atherosclerosis. The technique developed in this thesis can be conveniently extended to further clinical applications of CFD simulations.

1.6 Limitations of the Study

In the first part of the study, idealized models of thoracic aorta were used for investigating the blood flow. The flow dynamics obtained from these models could be far from reality. This is due to the fact that local details of the realistic aorta such as successive curvature of descending aorta or the blunt corners at the branching could not be included. As mentioned in the text, the idealized models were used to obtain an estimate of the real flow in an aorta. To understand the role of artery anatomy, several models were used to simulate the blood flow. The flow profiles were compared to understand the role of artery anatomy and extent of idealization on the flow dynamics. This limitation could be overcome by using CT image based aorta models.

The other limitation with the CT image based aorta model was the assumption of rigid artery wall. Aorta walls are thick and elastic in nature. During the systole part of the cardiac cycle, a large amount of blood is pumped from the left ventricle of heart to the aorta. The ascending aorta walls expand to accumulate the large amount of blood pumped by the left ventricle of heart. To simulate such a complex phenomena, a special computational code is required that offers to solve the fluid flow as well as the structural deformation. Since the computational code used during the course of the work did not offer such calculations, the aorta walls were assumed to be rigid. However, that limitation will be resolved in our future works to achieve more precise results. The details of the work in progress are briefly described in the last chapter of the thesis.

2 Reconstruction of Idealized and Realistic Models of Human Aorta

This chapter describes the idealized models of aorta used for numerical simulations for the first part of the studies. The construction of each human aorta model and their features are described in this chapter. The main aim with the use of idealized models of aorta was to obtain an estimate of flow dynamics in the actual human aorta. The aorta models were assumed to be under the mean blood pressure of 100 mmHg for the normal blood pressure range, i.e. 80-180 mmHg. The aorta model-3 was modified to study the flow dynamics in the aorta under the conditions of hypertension and hypotension. This chapter concludes with the description of modification of aorta model-3.

2.1 Reconstruction of Idealized Aorta Models

The aorta is the largest artery in the human circulatory system starting from the left ventricle of the heart. It then makes a 180° arch and descends towards the abdominal region where it bifurcates into iliac arteries. The aortic arch branches into three major branches of aortic arch namely the brachiocephalic artery, left common carotid artery, and left subclavian artery which lead to the arms and neck region. The anatomy of the branching can vary in humans, e.g. in the location of branching arteries, size of arteries, and length of arteries. The curvature in the aorta and branching arteries are highly non-planar and three dimensional. The aorta models used in this study were constructed in four parts: ascending aorta, aortic arch, descending aorta, and three major branches. The features of each of the aorta models are distinct. This was done in order to compare and understand the effect of artery anatomy on the dynamics of blood flow. Figure 4.3 shows the schematic diagram of the three aorta models used for numerical simulations. The following sub-sections describe the features of the aorta models.

2.1.1 Idealized Aorta Model-1

This model of aorta was constructed with the measurements from Gao et al. (2006). The descending aorta runs upwards for 14.5 mm and makes an angle of 10° with sagittal plane. The aortic arch is curved at 190° with the radius of curvature being 28 mm. The descending aorta runs for 50 mm towards the abdominal region making an angle of 10° with sagittal plane. The major branches were neglected in the aorta model used by Gao et al. (2006). The three major branches were introduced in the aortic arch section. The left common carotid artery in the model was located at the top of the aortic arch. The Brachiocephalic artery and left subclavian artery were assumed to be symmetric to each other with

the same radius of curvature in respective directions. The schematic diagram of the model is shown in Figure 2.1A.

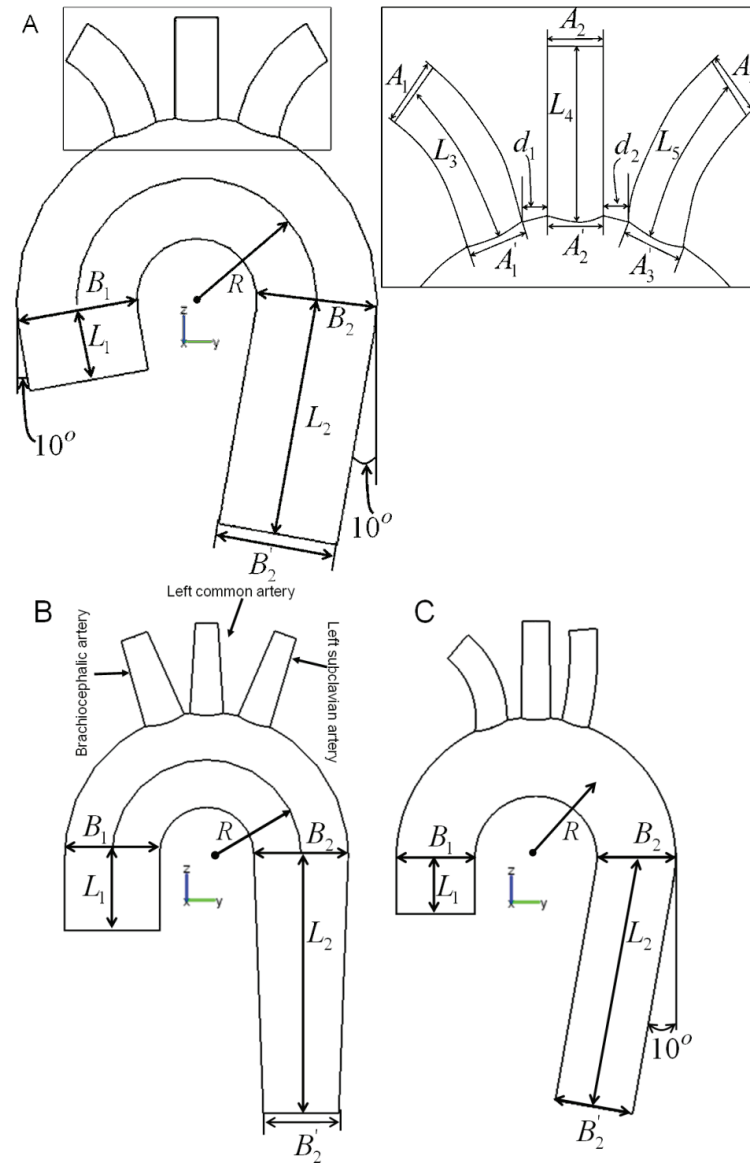


Figure 2.1: Schematic diagrams of idealized models of the human aorta (A) model-1, (B) model-2, and (C) model-3. The inset shows the branches and reference alphabets.

The aorta model was planar in coronal plane. The main aorta trunk was assumed to have uniform area of cross-section. The major branching arteries were also assumed to have uniform areas of cross-section. The model will be referred to as G1 in the following sections.

2.1.2 Idealized Aorta Model-2

The second model of human aorta was reconstructed using the measurements from Park et al. (2007). In this model, the descending aorta is straight and runs upwards for 20 mm. The aortic arch bends for 180° with the radius of curvature of 25 mm. The descending aorta is 68 mm long and includes the effects of tapering. The tapering coefficient was calculated to be 0.0813 for the length of 0.68 mm. The three branching arteries were straight from their respective points of orientation. The tapering effect was also introduced in branching arteries.

The original model used in the work by Park et al. (2007) included other minor branches. Park et al. (2007) used porous media as the outlet boundary condition for their experiments. In order to achieve this, additional porous cuboids were attached to the outlets of each branching artery. Since the aim of this study was to simulate the blood flow in the main trunk of aorta and three major branches, the additional branches were neglected in the model used in this work. The additional porous media cuboids were also neglected in the aorta model. This aorta model was also planar in coronal plane. The descending aorta and aortic arch were assumed to have uniform areas of cross-section. The model will be referred to as G2 in the following sections.

2.1.3 Idealized Aorta Model-3

The third idealized model of human aorta was reconstructed with measurements from Kim et al. (2004) and Shahcheraghi et al. (2007). As in model G2, the descending aorta in this model is also straight. It runs upwards only for 18 mm. The aortic arch bends for 190° with the radius of curvature of 32 mm. The descending aorta is 75 mm long and makes an angle of 10° with sagittal plane. The Brachiocephalic artery which is placed at the top of the aortic arch is the only part of this model with the effect of tapering. The main trunk of aorta, left common carotid artery, and left subclavian artery were assumed to have a uniform area of cross-section. The original model used by Kim et al. (2004) and Shahcheraghi et al. (2007) had two curvatures in the descending aorta. This feature was neglected in our model. This model of aorta is the closest approximation of the real aorta since the original model was based on the measurements from the CT image. The model will be referred to as G3 in the following sections.

2.1.4 Idealized Aorta Model-3 under hypotension and hypertension

The aorta models G1, G2, and G3 were assumed to be under the mean blood pressure of 100 mmHg for the normal blood pressure range, i.e. 80-180 mmHg. The aorta model G3 was modified to mimic aorta under the mean blood pressure of 80 mmHg (Hypotension) and 140 mmHg (Hypertension). The lumen of the aorta and its branching arteries were modified according to the pressure-lumen area relation given in the work of Towfiq et al. (1986). Figure 2.2 shows the relation of lumen aorta and pressure used for modifying the aorta models. The aorta models were constructed using the same procedure which was used for the normal aorta models. Along with the geometry of the aorta, the boundary conditions were also modified for hypertension and hypotension. The changes in the flow dynamics due to the changes in the pressure will be discussed in the results section.

The major and minor differences in the aorta models G1, G2, and G3 will allow the comparison of local and global flow dynamics. The main aim of these numerical simulations was to obtain an estimate of flow dynamics in the real aorta and compare the flow dynamics in the different models of human aorta. The shape, size, and orientation of branches would give an estimate of the flow dynamics in the branches under various orientations. The modification in the aorta model G3 under hypotension and hypertension will also provide an estimate of the flow dynamics under the condition of hypotension and hypertension.

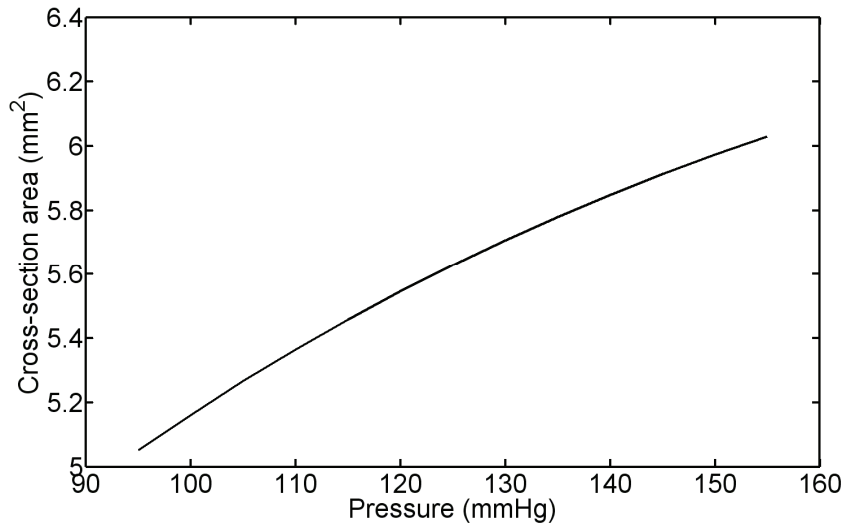


Figure 2.2: The plot of pressure versus luminal cross-sectional area of ascending aorta estimated from Towfiq et al. (1986).

The aorta models described in this chapter were constructed using the CAD design module available in the FEM based code Comsol Multiphysics V3.5a. The additional experimental setups, boundary conditions, and numerical solver are discussed in Chapter 4 of this thesis.

2.2 Reconstruction of Realistic Human Aorta Model from CT Images

In this chapter, the method for the reconstruction of a 3D human aorta model from CT images is presented. The chapter begins with a brief introduction to the CT imaging technique. This is followed by a step-by-step description of the reconstruction of the realistic human aorta model from CT images. This includes the pre-processing of images, fundamental image processing operations, and CAD operations used for the surface and solid rendering.

2.2.1 Computed Tomography Images

CT is a non-invasive medical image technique used to obtain 2D X-ray images of the inside of a body. The CT imaging technique is mostly used for medical examination and diagnosis. With specialized equipment and software the diseases such as cancers, tumors, and other physical disorders can be easily diagnosed. With this modality it is possible to obtain high resolution images of inside of a body with a very thin slice thickness. These images also have a high contrast which makes it possible to see each organ and part of body distinctly by a slight adjustment of contrast. For example, by enhancing and adjusting the contrast, the regions such as arteries filled with blood or lungs filled with air can be made distinct from the rest of the image. In CT images, unlike in X-ray images, the organs' images are not superimposed over each other. These features enable radiologists to get precise information on diseases and assess the severity of the disease.

A typical CT image is a grayscale cross-sectional image of the inside of a body. The image is created based on the amount of X-ray absorbed by tissues and organs. The organs with a high density, e.g. bones, are visible with brighter white color while the organs with a low density, e.g. artery walls, appear with a darker color. The CT images are generated in DICOM format, which is a standard for the image exchange in digital formats. The images in DICOM format have vital information such as voxel width, voxel height, pixel width etc. embedded within the images. This information is embedded with the imaging equipment which produces the images.

For the present study, two sets of CT images were made available by the South Karelia Central Hospital in Lappeenranta City in Finland. The CT data included images starting from the neck region running till the abdominal region. The obtained grayscale CT images were processed with advanced medical image processing code 3D-Doctor V4.0. Additional Computer Aided Design (CAD) operations were performed using CAD program Solidworks 2008 and Catia V6R2009. The following sub-sections contain the description of the image processing and CAD operations performed for the reconstruction of the real human aorta model.

2.2.2 Image processing of CT Images

The CT images are grayscale images, and can thus be treated with fundamental image processing operations. The following image processing operations were performed with the medical image processing code 3D-Doctor. To begin the image processing operations, the set of CT images are imported in 3D-Doctor. The image processing operations used in the treatment of CT images are described below.

- **Image Calibration:** The image data such as voxel width, voxel height, and slice thickness are adjusted. This operation ensures the correct scale of the output model. The DICOM set of images have their own calibration data.
- **Contrast Adjustment:** As a pre-processing, the contrast of the CT images is adjusted in order to make the arteries brighter and distinctly visible. This is done by limiting the grayscale values of image pixels. By adjusting contrast, we also suppress the visibility of other organs.
- **Object definition:** The ‘objects’ are defined within the image processing code prior to the segmentation of image. The ‘objects’ are groups of pixels which later will be identified based on grayscale threshold limits. In the later stage of the processing, each ‘object’ will have its own range of grayscale values. This helps in distinguishing and recognition of various organs and tissues. For example, the CT images of abdominal region may have objects such as ‘intestine’, ‘kidney’, ‘spine’, and ‘arteries’. The object named ‘aorta’ was defined during the image processing of case-1 for extracting aorta surface.
- **Selecting region of interest:** A region of interest (ROI) is an area of the image where the organ or tissue of interest (aorta in our case) is expected to lie. The selection of ROI limits the image processing operations to ROI. This operation saves a lot of time since we can avoid processing the entire CT image. The ROI for a set of data can be selected in two ways. A single ROI can be used for the whole set of image data, or each image can have its own ROI.

The operations of contrast adjustment, selection of ROI, and object definition can be performed in any sequence. Once these operations are performed, the CT images are ready for further image processing operations.

- Grayscale threshold selection: For grayscale images, a typical grayscale threshold is a grayscale pixel value which is an upper or a lower limit for identifying 'objects'. In a CT image, the tissue in different organs appears with pixels with a grayscale value. The grayscale thresholds are selected in such a way that the 'object' of interest can be extracted from the rest of the image. The selection of threshold heavily depends on how well the tissues are illuminated. Like ROI, the grayscale thresholds can also be selected in two ways. A single upper and a lower threshold can be used for the entire set of CT images, or several thresholds can be selected for each image individually.

The thresholds are to be precisely selected as the shape of the final 'object' depends on the threshold selection. The grayscale thresholds are also vital in obtaining local microscopic details of the artery surface.

- Image segmentation: Based on the upper and lower grayscale thresholds, the 'object' is segmented from the image. The object boundaries are extracted in the form of a closed contour surrounding the group of pixels recognized as 'object'. The additional boundaries which are wrongly identified as 'objects' are carefully removed. With the threshold selection and image segmentation, several contours representing lumen of aorta are generated for each CT image.

The threshold selection and image segmentation can be performed either on all the images at the same time or on each image individually. The image processing operations listed above are demonstrated in Figure 2.3B-F. Figure 2.3F shows the 3D surface rendered from 2D contours obtained with image processing operations. The following section contains a brief description of 3D surface and 3D volume rendering procedure.

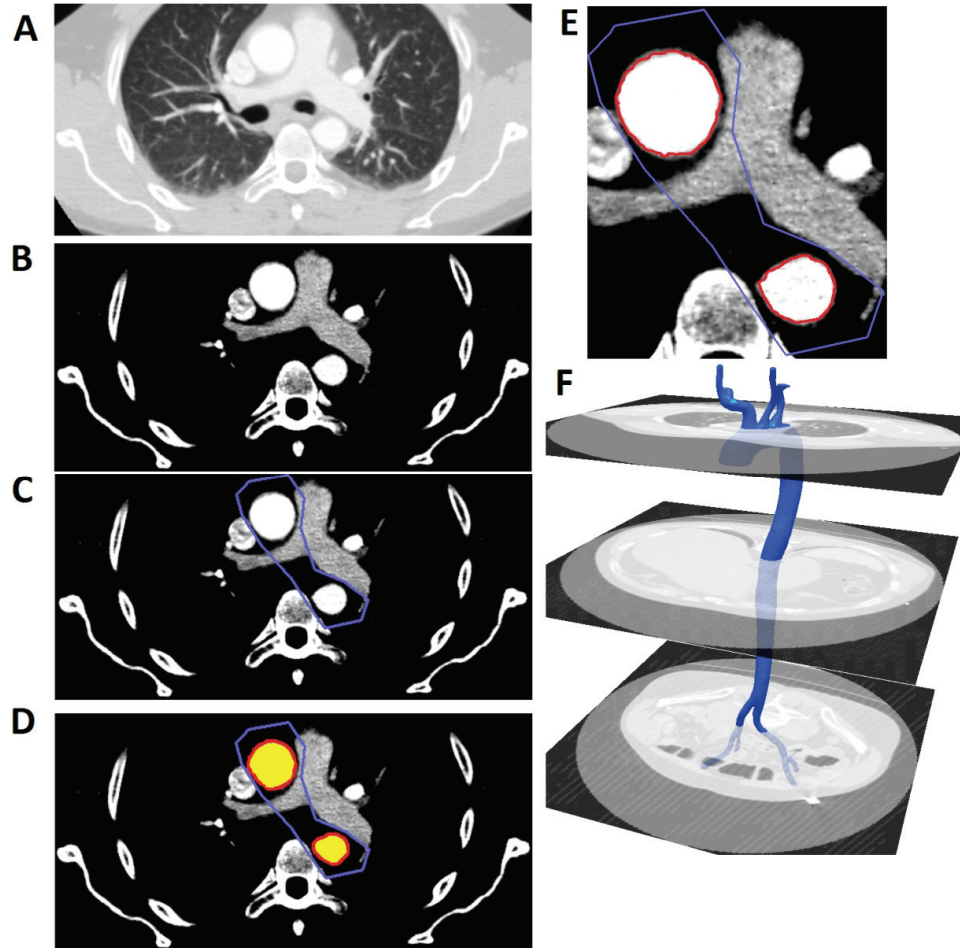


Figure 2.3: (A) A typical CT image sampled from data provided by South Karelia Central Hospital. The image processing operations of (B) contrast adjustment, (C) Selection of ROI, (D) image segmentations (area in yellow is segmented as artery lumen), (E) artery lumen contour generation, and (F) 3D surface rendering performed with medical image processing code 3D-Doctor.

2.2.3 3D surface rendering and other CAD operations

The image processing operations are followed by two CAD operations, namely the surface rendering and volume rendering. The surface rendering generates a 3D surface representing the lumen of the aorta and respective branches, while the volume rendering is a step-by-step procedure to convert the rendered surface to a 3D volume which will be the computational domain. The surface model generated by the image processing code 3D-Doctor is not compatible with the numerical solver Fluent V12 directly. Thus, these operations are essential to make the aorta models compatible with the mesh generating code Gambit and the numerical code Ansys Fluent.

- 3D surface rendering: An algorithm based on the region growth method was used for 3D surface rendering. Additional information of the surface texture is also used for this purpose. A complex 3D surface is generated based on the boundary details obtained with image processing operations mentioned in the sections above. With complex surfaces, details such as branching and local curvatures can be precisely included in the model. The generated complex surface is made up of polygons and tetrahedral elements. The size of these elements is kept as small as possible to construct a model with exact details.

As the final output, a 3D smooth hollow surface representing the aorta is generated. The model is refined repeatedly to make the aorta surface smooth and optimizing the number of polygon elements. The 3D surface model is then exported to a mechanical design program Catia V6R2009 for further operations.

- 3D solid volume rendering: With the volume rendering procedure, the 3D surface model of aorta is converted to a 3D solid model using mechanical design program Catia V6R2009. This subsection presents the steps for the conversion in brief.
 - The 3D hollow surface is imported as digitized points on the surface of the aorta.
 - The digitized points are sampled to avoid processing a large number of points. The sampling is carried out in such a way that the sample points represent the aorta surface with 99% accuracy.
 - Number of sub-surfaces (m) is chosen. Sub-surfaces are smaller simple surfaces which will constitute the final 3D surface enclosing the volume of aorta.

- The digitized points are then divided into m groups of points where each group of points is associated with one of the m surfaces.
- The number of points in each group depends on the complexity of the surface: a less complex surface would have a smaller number of associated points while a more complex surface would have a larger number of associated points.
- m new sub-surfaces are generated based on the points in the group.
- The m surfaces are stitched together to form a volume representing the lumen of thoracic aorta.

Figure 2.4 shows the flow chart with the operations of image processing and CAD operations, while Figure 2.5 shows the sample aorta model with sub-surfaces and a sample of mesh grid used for computation.

Table 2.1: Information of image data provided by South Karelia Central Hospital

Information	Case-1 (R1)	Case-2 (R2)
Patient Sex	Female	Male
Age	55 Year	56 Years
Number of CT slices (k)	710	450
Image Resolution	512×512	512×512
Pixel Width	0.628	0.628
Slice Thickness	0.5 mm	1 mm

The details of the aorta models are given in following two sections.

2.2.4 Realistic Aorta Model-1

The patient was reported to have no arterial diseases in the main aortic arch during the acquisition of CT images. The patient had a minor stenosis in the descending aorta which was corrected during the image processing operations. The large number of CT images in this case allowed the reconstruction of the aorta with precise details. However, due to the limitations with the data made available, three major branching arteries turned out to be shorter. This model will be referred to as R1 in the further discussions. Since the study is focused on blood flow in aortic arch and three major branches, the iliac, renal and other smaller arteries are ignored.

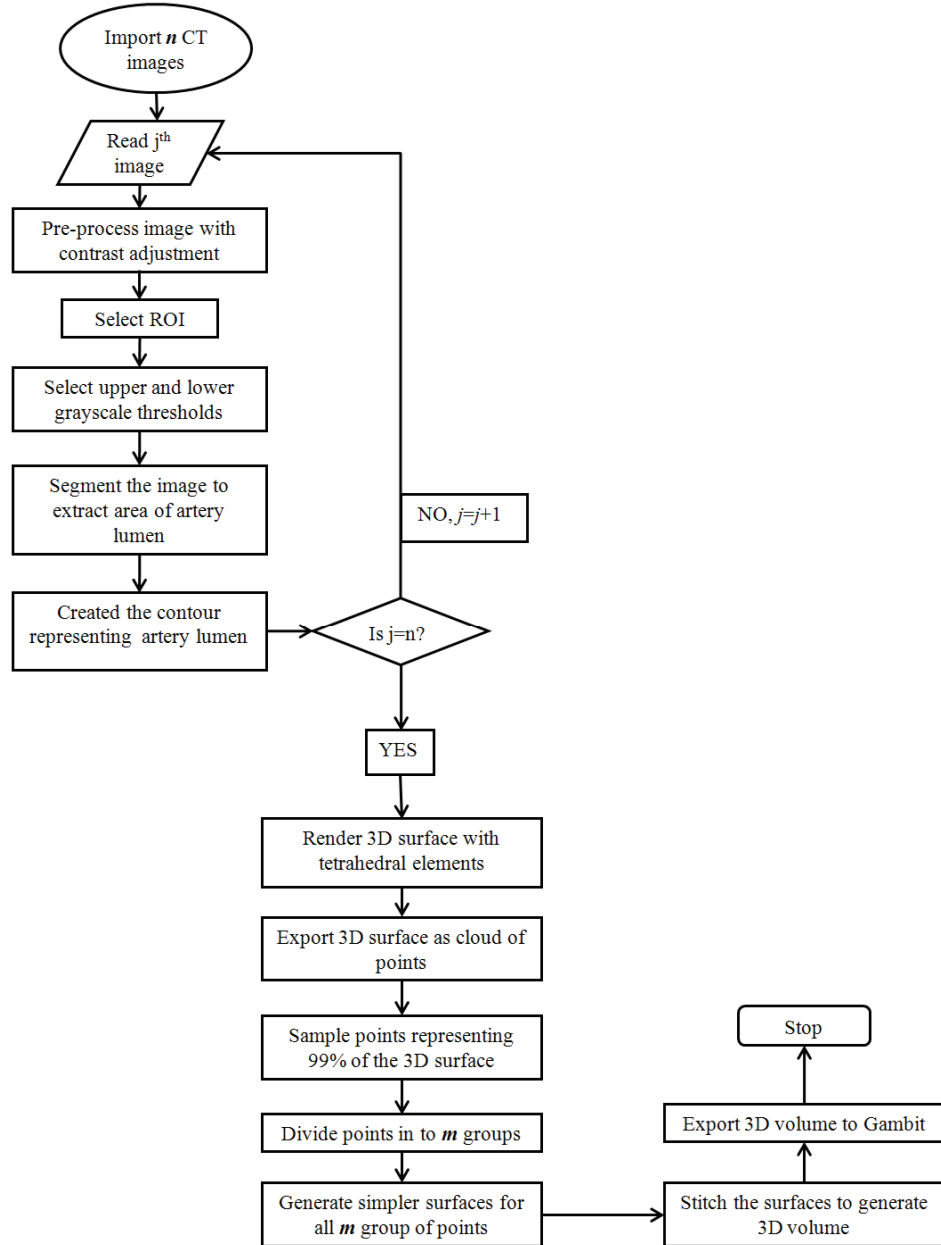


Figure 2.4: The flow chart of procedure to reconstruct 3D solid aorta model from 2D CT images.

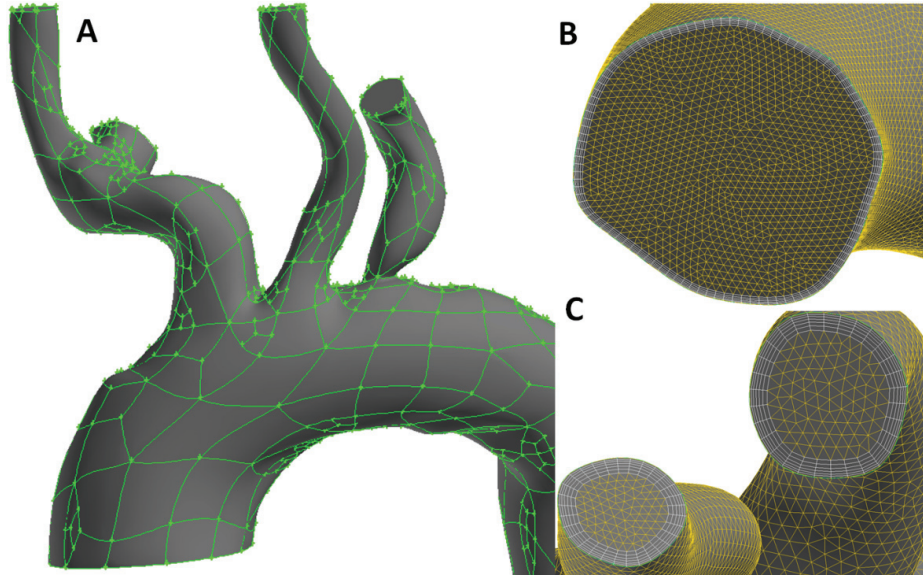


Figure 2.5: (A) A 3D aorta model generated in the mechanical design code Catia VR2009 and (B, C) a sample of mesh grid generated with Gambit V2.4.

For the current study, two sets of CT images were obtained from the Radiology Department of South Karelia Central Hospital in Lappeenranta, Finland. Both sets of images were processed with image processing and CAD operations described in the previous sections. The details of CT images are given in Table 2.1.

2.2.5 Realistic Aorta Model-2

The patient was reported to have no arterial diseases of thoracic aorta during the acquisition of CT images. Since the CT images in second set were fewer than in the first case, the CT images were re-sliced. Re-slicing is an operation in the medical image processing to adjust the slice thickness. The operation of re-slicing is vital in obtaining a precise and detailed representation of internal organs. The CT images in second data were re-sliced to achieve a higher accuracy in the final 3D model. The re-sliced data had 700 images with the slice thickness of 0.5 mm. This model will be referred to as R2 in the further discussions.

3 Simulation Methodology

In this chapter, the experimental setup for FEM and FVM based solvers are presented. The chapter begins with the description of the mesh grid used for numerical simulations followed by a brief discussion about the physical properties of blood. The chapter also includes information of the boundary conditions and governing equations. The chapter concludes with remarks to the reliability of the results on the mesh grid, numerical method, and the use of realistic aorta model for numerical simulations.

3.1 Mesh Grid for FEM and FVM Solvers

The aorta geometries G1, G2, G3, and variants of G3 were reconstructed using the design module in a FEM based code Comsol Multiphysics 3.4a. The mesh for these aorta models were made with the mesh module of the FEM based code. The computational mesh utilized in the simulations consists of nearly 35000 to 42000 tetrahedral elements varying for different geometries of simulations.

The mesh grids for the realistic aorta models were generated using Gambit V.2.4.6. Gambit is a design and mesh generating code for FVM based computational code Ansys Fluent. The mesh grid had nearly 2000000 hybrid grid elements (tetrahedral and hexahedral). Thin boundary layers were used for precise calculations close to the aorta walls.

For both, FEM and FVM, experiments the mesh grids were refined to achieve precise solutions. Several steady state simulations were performed with different mesh grids to ensure the mesh independence of the results. Although the FVM based solver could easily handle 2 million elements, the mesh for FEM based solver could not be refined. However, for the FEM based solver, the finest possible mesh grid was used to ensure that the solutions obtained are independent of the mesh.

3.2 Physical Properties of Blood

Blood is a complex mixture of plasma, red blood cells, white blood cell, and platelets. The primary content of blood is plasma which is a Newtonian fluid (Morris et al. 2005, Taylor et al. 1998). The blood cells and platelets are of different sizes and weights. Thus, the physical properties of blood depend on its constituents. The local behavior of blood depends on the viscosity of blood and the volume fraction of blood cells in the plasma (Kim et al. 2008). The blood acts as a non-Newtonian fluid in small size arteries where diameters of arteries are in

the scale of size of blood cells (Li 2004), but in large and medium sized arteries, the blood is a homogeneous mixture of plasma and blood cells. In large and medium sized arteries blood acts as a Newtonian fluid [Fung 1997, Pedley 1980]. For the numerical simulations with both idealized and realistic aorta models, the blood was assumed to have the density of 1060 kg/m³ and the viscosity of 0.0035 Pa-s.

3.3 Boundary conditions

The pressure and velocity pulse have been used as inlet boundary conditions for blood flow simulations in several earlier research works. The pressure type boundary condition was deployed at the inlet for the numerical simulations with the idealized models of aorta. For the numerical simulations with the realistic models of aorta a time dependent flat velocity profile was used as inlet boundary condition.

3.3.1 Pressure Inlet Boundary conditions

The heart generates the pressure gradient which drives blood in the circulatory system. The pressure gradient is the driving force for the blood flow within the arteries. For the set of simulation conducted with the idealized models of human aorta, pressure inlet and pressure outlet boundary conditions were used. A 9th degree polynomial was used to estimate the pressure pulse used as the inlet boundary condition.

$$f(x) = \begin{cases} \sum_{i=1}^9 C_i (t - 0.85n)^i + 79.202 & \text{when, } t \in [0.85n, 0.85(n+1) - 0.34] \\ -61.4952(t - 0.85n) + 131.4730 & \text{when, } t \in [0.85(n+1) - 0.34, 0.85(n+1)] \end{cases} \quad (3.1)$$

where n is the number of cycles taken as $n=1, 2, 3$, and 4. The equation coefficients are given in Table 1.

Table 3.1: Values of coefficients C_i 's ($\times 10^5$) for polynomial given in equation 4.1 used as pressure waveform

Coefficient	C_1	C_2	C_3	C_4	C_5	C_6	C_7	C_8
Value	-5.6	0.0018	-0.014	-0.43	0.66	-0.005	-0.0004	0.987

The polynomial was sampled from Conlon et al. (2006). The pulsatile pressure profile used as the inlet boundary condition is shown in Figure 3.1A. The pulse is divided into ventricular systole and ventricular diastole. The aortic valve closes causing a rise in the pressure in the left ventricle of heart. When the pressure in the left ventricle exceeds the pressure in the aorta, the aortic valve opens and blood flows from the left ventricle to aorta. This is followed by the closing of the aortic valve for a very short period of time, which causes a rapid rise in the pressure in the left ventricle. Although the aortic valve is closed, there is no change in the volume of blood in the left ventricle. The pressure in the aortic valve only rises so that both the pulmonary and aortic valves open. When the aortic valve opens, the pressure in the left ventricle falls rapidly. When the pressure in the left ventricle is lower than the aortic pressure, the aortic valve closes. The aortic valve closes for three times within a cardiac cycle. The event between the first two closings of the valves is called the systole and the event between the last two closings of the valves is called the diastole. The pulsatile pressure cycle used in the numerical simulations lasts 0.85 s with a systole of 0.35 s and a diastole of 0.5 s.

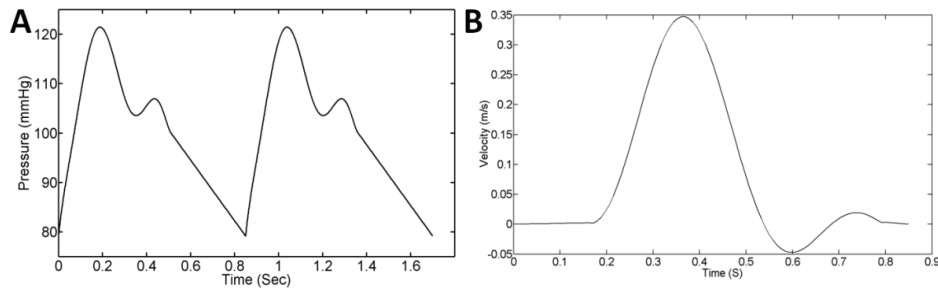


Figure 3.1: (A) The pulsatile pressure profile (Pa) and (B) the pulsatile velocity (m/s) used as the inlet boundary condition for numerical simulations with the idealized and realistic models of human aorta respectively.

3.3.2 Velocity Inlet Boundary conditions

A time dependent, flat and pulsatile velocity profile was used as the inlet boundary condition for numerical simulations with the realistic models of aorta. Since the flow data for the patient were unavailable, the velocity profile was sampled from Morris et al. (2005). A smooth curve (as shown in Figure. 3.1B) was fitted to the data points sampled from Morris et al. (2005). The acceleration during initial 0.15 s is very low. The flow accelerates rapidly in the time range from 0.15 s to 0.36 s achieving the maximum velocity at 0.36 s. The flow then decelerates to zero in the time range from 0.36 s to 0.55 s. In the time range from

0.55 s to 0.65 s the flow is negative due to the closing of the aortic valve. The flow then retains a positive velocity at the end of the cycle. Pedley (1980) observed a plug velocity profile close to the aortic valve region with experiments with thin film. The velocity profile has also been used as the inlet boundary condition by Shahcheraghi et al. (2002).

3.3.3 Outlet Boundary conditions

The boundary conditions such as velocity pulse or pressure waveform have been successfully used as inlet boundary conditions. However, boundary conditions deployed at the outlets have been a topic of debate. Some of earlier works such as Mori et al. (2002) have used pressure as the boundary condition at outlets. Shahcheraghi et al. (2002) have used outflow conditions coupled with zero pressure deployed at outlet. However, pressure and velocity profiles may not be known at the exact locations but are to be calculated by numerical simulations (Park et al. 2007). As an alternate to deploying boundary conditions at outlet, Park et al. (2007) used an innovative approach by using an integrated model of arteries along with pseudo organs. A solid porous media with permeability equivalent to respective organs were attached at each branching outlet. With an iterative procedure, the permeability of each of the pseudo organs was corrected via 2D experiments. The precise permeability of each organ was then deployed in the final 3D experiment. Zhou et al. (2010) have used the three-element Windkessel model to determine the boundary conditions at outlets in a full-scale model of the entire system of arteries. In both the works the aorta models were full-scale including most of the minor branching arteries. Thus, the boundary conditions used by these works may be limited to the full scale modeling. Thus, the porous media or Windkessel type boundary conditions may not be applied to 3D models with relatively short branches. In recent works, Wen et al. (2010) constructed both a prototype and a 3D CAD model of an aorta. The boundary conditions for their numerical simulations were the velocity and pressure profiles obtained from the in vitro experiments with the prototype model. This approach cannot be used in cases with realistic arteries as it is very difficult to obtain precise flow dynamics at exact locations in an artery.

In the study with idealized models of aorta, the boundary conditions at the outlet were set as spatially constant pressures over the cross sections but time dependent. Shahcheraghi et al. (2002) applied a constant flow rate condition coupled with zero pressure at outlets so that five percent of the flow rate was diverted to each branch. However, this condition may not precisely represent the reality as the flow rate may vary slightly in time. Instead, the ratio of inlet to outlet instantaneous pressures can be assumed as constant. It means that the value of pressure in each outlet is given as a certain fraction of the inlet pressure at the corresponding

instant. These fractions are obtained by simulating the steady state with the flow rates across the outlet sections, each given 5 percent of the flow rate across the inlet section. They are obtained as 0.9917 for the descending aorta outlet, 0.9955 for the Brachiocephalic artery outlet, and 0.9947 for the left common carotid and left subclavian arteries outlets.

The pressure inlet and outlet boundary conditions were also used for the preliminary experiments with realistic models. However unusual distribution of WSS was observed in our early experiments with idealized models and pressure drop applied as a boundary condition, extreme flow dynamics was observed at the outlets. To avoid specifying the pressure condition at the outlets, outflow boundary conditions were deployed at the outlets. According to Middleman (1972), approximately 5% of the blood flows out through each of the major branches at the aortic arch. The percentage outflow boundary condition was also used by Shahcheraghi et al., (2002) and Kim et al., (2004) in their respective works. The outflow percentages were recalculated based on the outlet area of each branch. According to the new calculations, approximately 11, 3, 2, and 5 percent of the flow flows through the right subclavian artery, right common carotid artery, left common carotid artery, and left subclavian artery respectively.

The assumption of the no-slip condition is valid in large arteries (Li 2004), as in large arteries the blood is a homogeneous mixture of plasma and blood cells. For all the numerical simulations, the artery walls were assumed to be rigid and a no slip condition was applied on the artery walls. Although it is indicative that the assumption of rigid wall in blood flow simulations may underestimate the temporal and spatial flow and wall motion, the aorta walls were assumed to be rigid for flow simulations under all three pressure regimes. Long term hypertension can cause the thickening of the arterial wall and the loss of elasticity of arterial wall (Ku 1997). Thus, the aorta walls can be assumed to be rigid under hypertensive flow regime. The assumption of rigid artery wall in the other two cases is acceptable as earlier works such as those of Khanafer (2006), Moayeri and Zehdehudi (2003), Zeng et al. (2000) and, Zhao (2000) have demonstrated that the arterial compliance does not influence the general characteristics of flow and WSS significantly. Moayeri and Zehdehudi (2003) compared the hemodynamic characteristics of the blood flow through the arterial stenosis with and without distensible walls numerically. The comparison revealed no difference between WSS distributions for the rigid and deformable walls during systole and diastole. Zhao et al. (2000) studied the influence of the wall distensibility on WSS numerically and did not find any significant difference between the WSS in rigid and compliant models. It is of notice that Zhao et al. (2000) used an angiogram based model of carotid bifurcation for their experiments. The atherosclerosis is often localized in the regions of low and oscillating WSS, flow

stagnation or recirculation. The elongation of separated flow region and local migration of recirculation or stagnant flow region may influence the localization of atherosclerosis only locally.

3.4 Flow governing equations

The blood flow is assumed to be governed by the momentum and mass balance equations. The maximum Reynolds number in the human aortic arch is 1500 (Peterson and Bronzino (P 195)), which is well below the critical limit of 2300 for the occurrence of turbulence. For all the numerical simulations the blood flow in the human aorta was assumed to be laminar and incompressible. The time dependent Navier-Stokes equations for the incompressible flow were used as governing equations are

$$\nabla \cdot \mathbf{u} = 0 \quad (3.2)$$

$$\rho \frac{\partial \mathbf{u}}{\partial t} + \rho(\mathbf{u} \cdot \nabla) \mathbf{u} = -\nabla p + \mu \nabla \cdot (\nabla \mathbf{u} (\nabla \mathbf{u})^T) \quad (3.3)$$

where \mathbf{u} is the velocity vector of the flow, p is the pressure, ρ is the density of blood and μ is the dynamic viscosity of blood.

The governing equations along with the boundary conditions were solved using two solvers. For the idealized models of aorta, G1, G2, and G3 FEM based code Comsol Multiphysics V3.5a was used, while for the realistic models, the FVM based code Ansys Fluent V12 was used. Following sub-sections describe the setup of the above mentioned solvers.

3.5 FEM Based Solver

For carrying out numerical simulations FEM base solver Comsol Multiphysics V3.4a and FVM based solvers Ansys Fluent V12.1 were used. The FEM based solver was used to simulate blood flow in idealized models G1, G2 and G3 of aorta while FVM based solver was used to simulate blood flow in realistic models of aorta reconstructed from CT images. Following sub-sections are brief discussions about the setup of solvers used during the numerical simulations.

3.5.1 FEM Based Solver Setup

The FEM based code was used for the numerical simulations with the idealized models of aorta. For these experiments, the governing equations are discretized

with Backwards Difference Method which is known to be a very stable method for decartelization. The discretized system of linear equations was solved using the iterative solvers Generalized Minimal Residual (GMRES) and Flexible GMRES (FGMRES). These iterative solvers deconstruct large numerical problems into simpler and manageable forms which can be solved using small memory. The solutions from smaller calculations are then recombined sequentially by GMRES to obtain the final solution. To improve the accuracy of the results, the local variations of flow variable in the computational grid elements were predicted by quadratic piecewise functions. A direct numerical solver such as GMRES and FGMRES would need a large computer memory for obtaining the solution as these direct solvers attempt to invert a very large matrix at once. Thus, the use of direct solver was avoided.

Steady state simulations were performed with the pressure of 80 mmHg deployed at the inlet of all three aorta models. The results of this experiment were used as an initial guess for the time-dependent numerical simulation of respective aorta models. The time-dependent experiments were initially performed with a coarse mesh grid as the FEM solver needed a large memory to obtain the initial solution. The mesh grid was subsequently modified and refined until a mesh independent solution was obtained. The residual for the solution of Navier-Stokes equations was kept at 1×10^{-4} and the experiment progressed with a time step of 0.001s. The simulations were allowed to proceed for four cycles of inlet boundary conditions. This was in order to ensure the periodic nature of the flow dynamics. The results from the fourth cardiac cycle are discussed in the results sections of this thesis. The distributions of velocity and WSS are investigated as these physical quantities are known to play a role in the development of arterial diseases, such as atherosclerosis.

The FEM based experiments were performed with an office computer with a 3 GHz Core 2 Duo processor with 3GB of RAM. The average calculation time for each cardiac cycle was varying from 0.75 to 1 hour.

3.5.2 FVM Based Solver

Despite the accuracy of the results, the FEM solver had several limitations. The first was the limitation of memory available for computation. The limited memory of the computer did not allow large calculations. Although the limitation of memory could be overcome with the use of iterative solvers, the solver could not handle a mesh grid larger than 65000 elements. In addition, the solver did not offer parallel computing for larger calculations. Above all, the solver environment was incapable of importing the real aorta model. Thus, the FVM based solver

which could overcome these restrictions was used for the calculations with the realistic models of aorta.

The governing equations were solved along with velocity inlet boundary conditions and mass flow outlet conditions. The SIMPLE algorithm was chosen for the solving of the pressure-velocity coupling. The residual errors for flow variables were kept limited to 1×10^{-4} . The time-dependent simulations were run for four inlet velocity cycles. This was to accomplish periodic spatial and temporal flow dynamics and make the final solution free from the influence of initial conditions. The results from the fourth velocity cycle are discussed in the results sections.

The accuracy and reliability of these numerical simulations is limited to the model used as the computational domain and solving algorithms. During this work, we wanted to quantify the reliability of these solvers via the comparison of results obtained from both the solvers. However, the limitations of FEM to import the realistic model of aorta to the solver did not allow that comparison. Significant improvements in the results were also expected and observed with the use of the realistic models of aorta.

4 Results from Idealized Models of Aorta

The results obtained from the numerical simulations with the idealized models of aortic arch using FEM are discussed in this chapter. The idealized aorta model G3 was modified according to the pressure-lumen area relation from work by Towfiq et al. (1986). The time-dependent simulations were performed for four cardiac cycles, and the results from the 4th cardiac cycle are discussed in this chapter. The distribution of pressure, wall shear stress and flow in the aorta model under the influence of normal pressure, hypotension, and hypertension are discussed. The flow, pressure, and WSS distributions are compared to understand the role of artery anatomy and pressure on the flow dynamics in three aorta models. The chapter begins with two subsections containing a brief description of the pressure distribution in the aorta models. The chapter continues with a detailed description of axial flow profiles. Further, the WSS distributions on the walls of aorta are discussed in the following subsections. The axial flow profiles and WSS distributions are discussed in more detail since WSS is known to be most important factor in determining vulnerable sites for atherosclerosis. The chapter concludes with remarks on the use of realistic models for numerical simulations of blood flow. In this chapter, the brachiocephalic artery, left common carotid artery, and right subclavian artery will be referred to as branch-1, branch-2, and branch-3, respectively.

4.1 Distribution of Pressure in Idealized Aorta Models

The distribution of pressure in the aorta models G1, G2, and G3 are shown in Figure 4.1. Because of the deployed boundary conditions, the pressure drop is positive towards downstream in all three aorta models. The distribution of pressure is qualitatively similar in all aorta models. In the ascending aorta, the pressure is uniformly distributed. In the proximal aortic arch region, high pressure is distributed towards the outer wall, while low pressure is distributed towards the inner aortic arch wall. Similar distribution of pressure is also observed in the distal aortic arch region. At the branch entry regions, low pressure is distributed in the proximal branching region and high pressure is distributed in the distal branching region. The distribution of pressure is uniform in the descending aorta.

Although the pressure distributions in all aorta models were qualitatively similar, there is a significant difference in the magnitude of the pressure. The maximum pressure observed in G1, G2, and G3 is 16275 Pa, 16132 Pa, and 16252 Pa, respectively. The maximum pressure in G1 and G2 is observed at the distal part of the junction of B3 and the aortic arch. In G3, the maximum pressure is observed at the distal part of the junction of B1 and the aortic arch. In G3, the pressure on

branches is relatively lower than that in G1 and G2. The distribution of pressure during the other parts of the cardiac cycle remained the same during the entire cardiac cycle, with the exception that the overall magnitude of pressure changed with inlet boundary conditions.

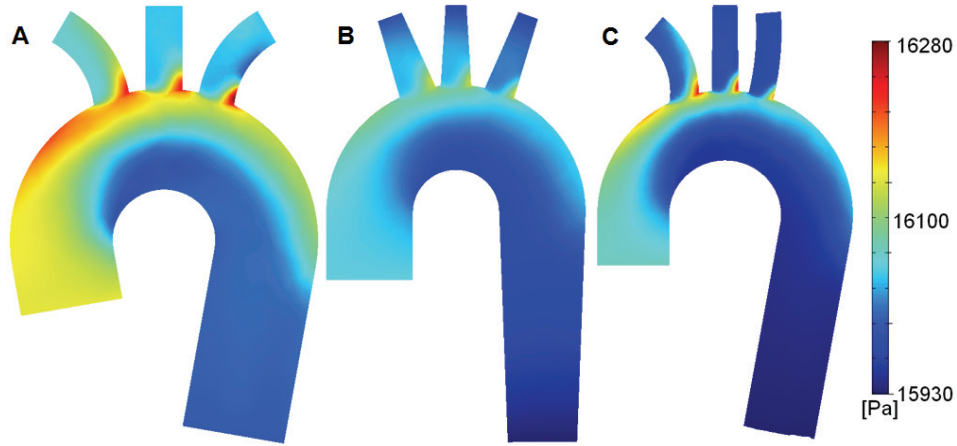


Figure 4.1: Frontal view of (A) G1, (B) G2, and (C) G3 showing the distribution of pressure (Pa) across the aorta models at $t=0.18$ s (systolic peak pressure).

4.1.1 Effect of Hypotension and Hypertension on the Distribution of Pressure in Idealized Aorta Models

The aorta models used for the simulations were assumed to be under the mean blood pressure of 100 mmHg for the normal blood pressure range, i.e. 80-180 mmHg. The aorta model G3 along with the inlet and outlet boundary conditions was modified to mimic the aorta under the mean blood pressure of 80 mmHg (Hypotension) and 140 mmHg (Hypertension). In all three cases, the distribution of pressure varied in accordance with the inlet boundary condition during the cardiac cycle. Thus, the distribution of pressure in respective pressure cases did not show a significant qualitative change. Figure 4.2 shows the distribution of pressure in the aorta model G3 under the influence of hypotension, normal pressure, and hypertension.

The distribution of pressure in G3 under normal pressure and hypotension is identical. However, under hypertension the distribution of pressure is amplified with the elevated magnitude of pressure. In the proximal aortic arch region, a higher pressure region is observed on the outer wall of the aortic arch for normal pressure and hypotension cases. This high pressure region on the outer wall of the proximal aortic arch shrinks and shifts towards the brachiocephalic artery in the

hypertension case. No other significant differences between the pressure distributions were noticed. The variations in the pressure distributions due to the modifications in geometry and boundary conditions are expected to affect the velocity and WSS distributions and mass flow through the branch outlets as well. The velocity distribution, WSS distributions, and mass flow through the branch outlets are discussed in the following sections.

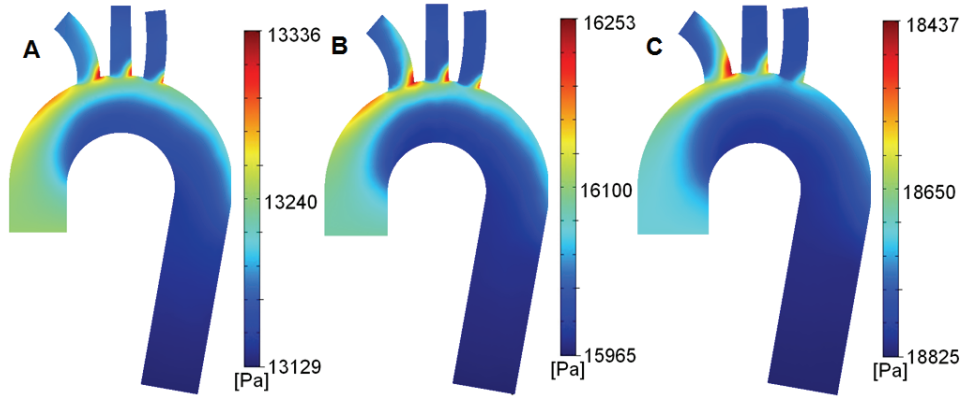


Figure 4.2: Frontal view of the aorta model G3 showing the distribution of pressure (Pa) across the aorta model at $t=0.18$ s (systolic peak of the fourth cycle) under (A) hypotension, (B) normal pressure, and (C) hypertension.

4.2 Flow Distribution in Aorta Models

The axial velocity profiles were captured at the symmetry plane, four axial cross-sections in the aortic arch, and two sections in each branch (Brachiocephalic artery, left common carotid artery, and right subclavian artery). The flow profiles were captured at peak systolic time instances $t=0.18$ s in the fourth cardiac cycle. The development and orientation of flow profiles in each aorta model are discussed in this section. This will be followed by a sub-section where the effects of hypotension and hypertension on the flow are discussed.

Figure 4.3 shows the velocity distributions in the symmetry plane of geometries G1, G2, and G3 at peak systolic pressure time $t=0.18$ s. In the ascending aorta in G1 and G2 the velocity distribution is skewed towards the outer wall of the aortic arch, while in G3 the flow in the ascending aorta is uniform and parabolic-like. In the proximal aortic arch of G1 and G2 skewness retains. It can be noticed in Figure 4.3 that in G1 and G2, the maximum is flow distributed in the centre of the arch, while in G3, the flow diversion to branch B1 has a significant effect on the

flow distribution within the aortic arch. Despite the differences in the flow distributions, flow stagnation occurs at the inner wall of the aortic arch in all three aorta models (Figure 4.4 A1-A3). The flow stagnation is caused by the secondary flow patterns in the aortic arch (Figure 4.4 B1-B3 and C1-C3). The flow from the centre of the arch moves towards the upper wall and then towards the side walls causing a c-shaped velocity distribution.

In the distal aortic arch of all three aorta models, the flow remains skewed towards the inner wall as the flow diversion towards the branches and secondary flow patterns dominate the flow (Figure 4.4 C1-C3). In G1, the flow distribution gains parabolic profiles close to the outlet, while in G2 and G3, the skewness in the flow distribution persists till the lower descending aorta. At the entry region of the branches, high velocity is observed in the proximal side of the entry regions. In G1 and G3, the high velocity is more pronounced, while in G2 the velocity magnitude is relatively lower than that in G1 and G3. The skewness of flow and the secondary flow patterns also persist in the branch arteries as well. The flow profiles captured at the entry region of the branches are compiled in Figure 4.4 D1-J3. It can be observed that the flow distribution close to the branch entry region is highly non-uniform (sections D1-D3, F1-F3, and I1-I3), while the flow distribution in the vicinity of the outlet retains the secondary flow patterns.

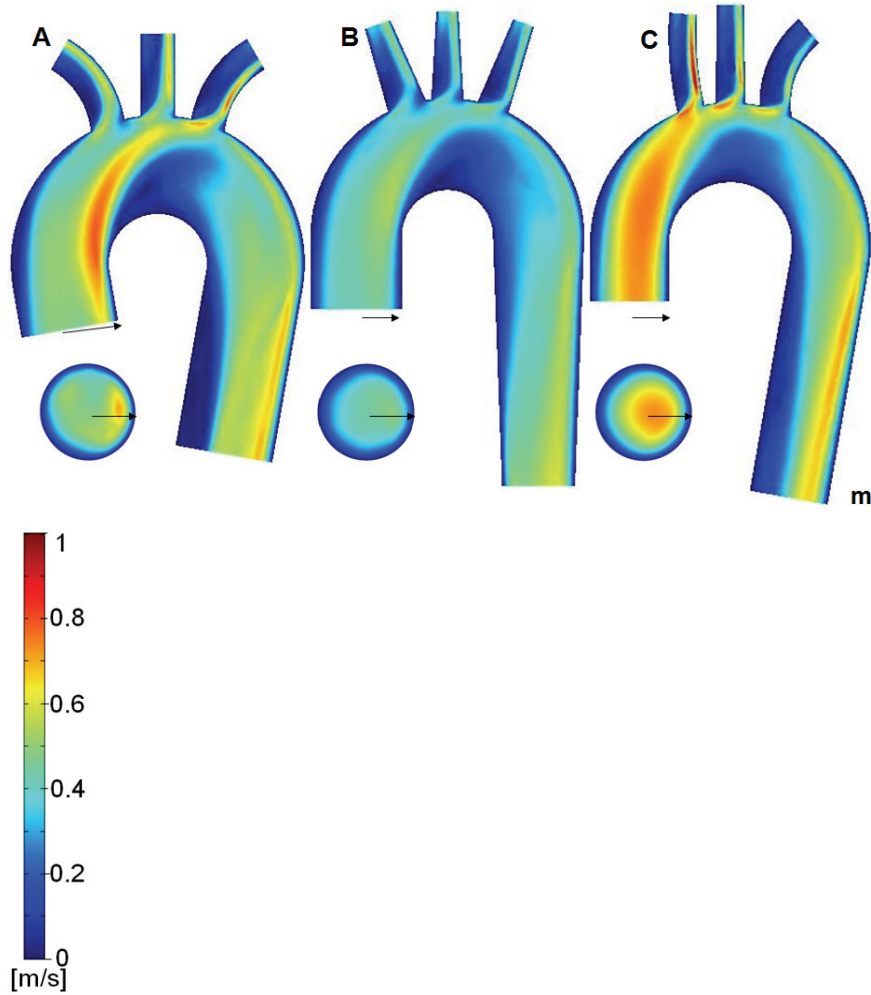


Figure 4.3: Velocity distribution across the symmetry plane of the aorta for the geometries (A) G1, (B) G2, and (C) G3 at $t = 0.18$ s (systolic peak of the fourth cycle in simulations).

The distribution of flow through the branching arteries has a significant effect on the mass flow rate through respective branches. The distribution of mass flow rate at the outlet of the branches during the cardiac cycle follow the distribution similar to the pressure condition imposed at the inlet. It was observed that for G1 and G3, the highest mass flow is through the branch B2 of the respective models, while for G2, the highest mass flow is through the branch B3. Amongst three

aorta models, the least amount of mass flow flows through the branches of model G2.

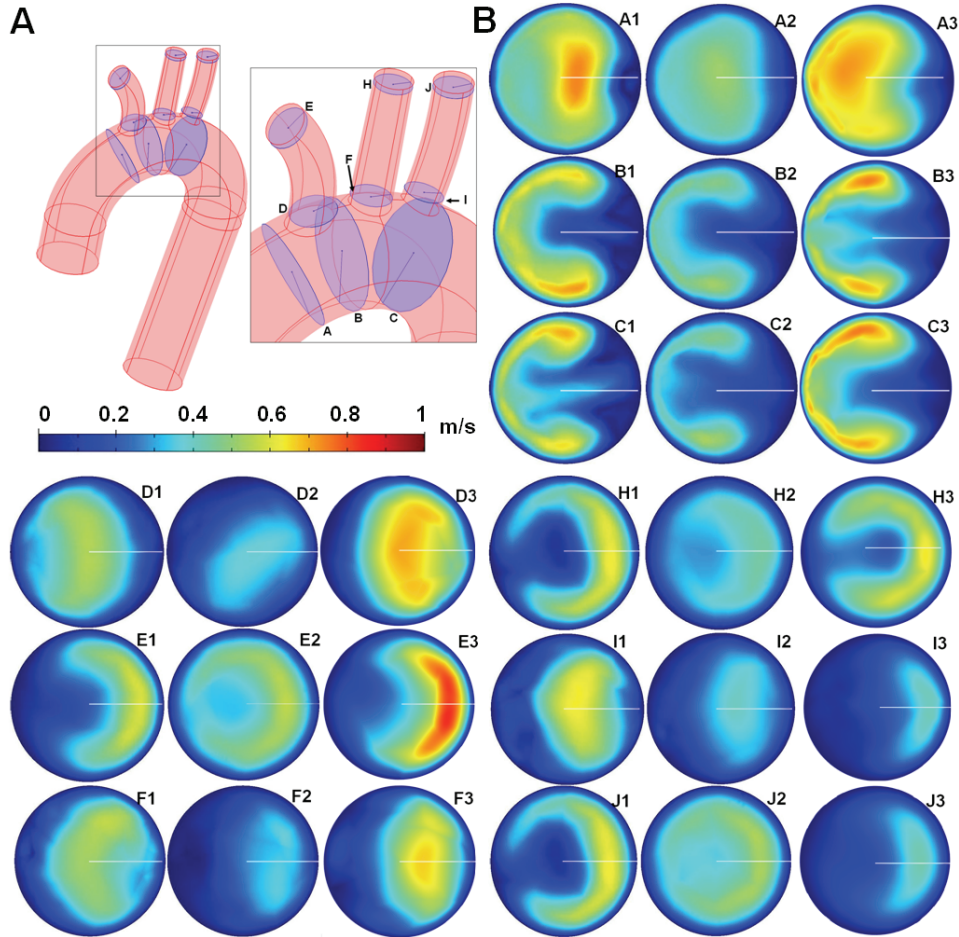


Figure 4.4: (A) Axial cross-sections within the aortic arch and branches, (B) Velocity profiles across different cross-sections in the geometry G1 (A1-J1), G2 (A2-J2), and G3 (A3-J3), respectively. Velocity profiles were captured at peak systolic time $t=0.18$ s.

4.2.1 Effect of Hypotension and Hypertension on Flow Distribution in the Idealized Aorta Model G3

The velocity distributions at the symmetry plane and axial cross-sections are compiled in Figures 4.5 and 4.6 respectively for the aorta model G3 under the

influence of hypotension, normal pressure, and hypertension at the peak systole time instance. It can be observed in Figure 4.6 that as the pressure increases in G3, the velocity profiles are amplified. It is of note that during hypertension, the velocity magnitude is exceptionally high. Under hypertension, normal pressure, and hypotension, the maximum velocity magnitudes are 0.56 m/s, 0.78 m/s, and 1 m/s respectively. The amplification of velocity profiles can also be observed in the axial sections A, D, and F in Figure 4.6 (A1-A3, D1-D3, and F1-F3). The secondary flow patterns persisted in the axial sections B, C, E, and H. With hypertension, the maximum velocity magnitude increased by 27%, while with hypotension, the maximum velocity magnitude dropped by 18%.

The modification in the aorta models G3 and the imposed pressure condition had a significant effect on the mass flow through the branches. The hypertension causes a rise in the mass flow through the branches B1, B2, and B3 by 55%, 61%, and 78% respectively. With hypotension, the mass flow through the branches B1, B2, and B3 dropped by 37%, 38%, and 60% respectively. The elevation and drop in the velocity magnitude is expected to have a significant effect on the WSS distribution on the wall of the aorta.

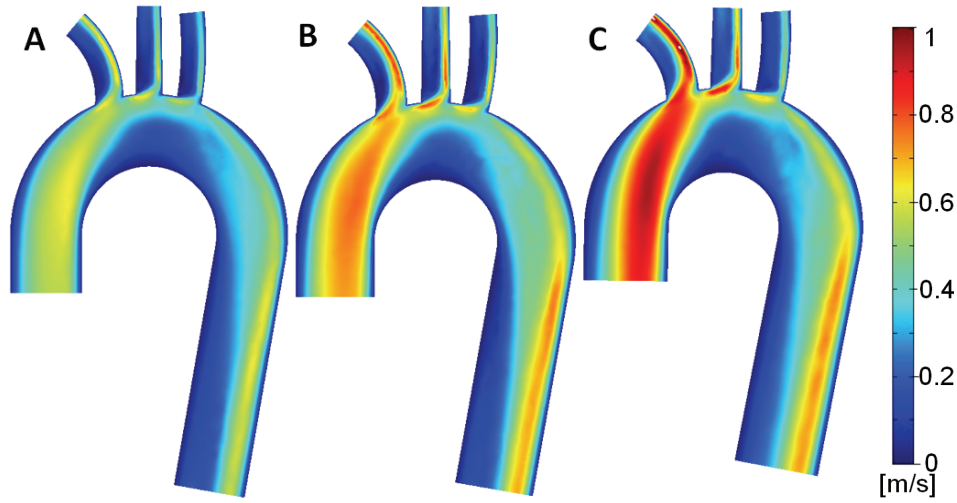


Figure 4.5: Velocity distribution across the symmetry plane of the aorta model G3 under (A) hypotension, (B) normal condition, and (C) hypertension at $t=2.73$ s.

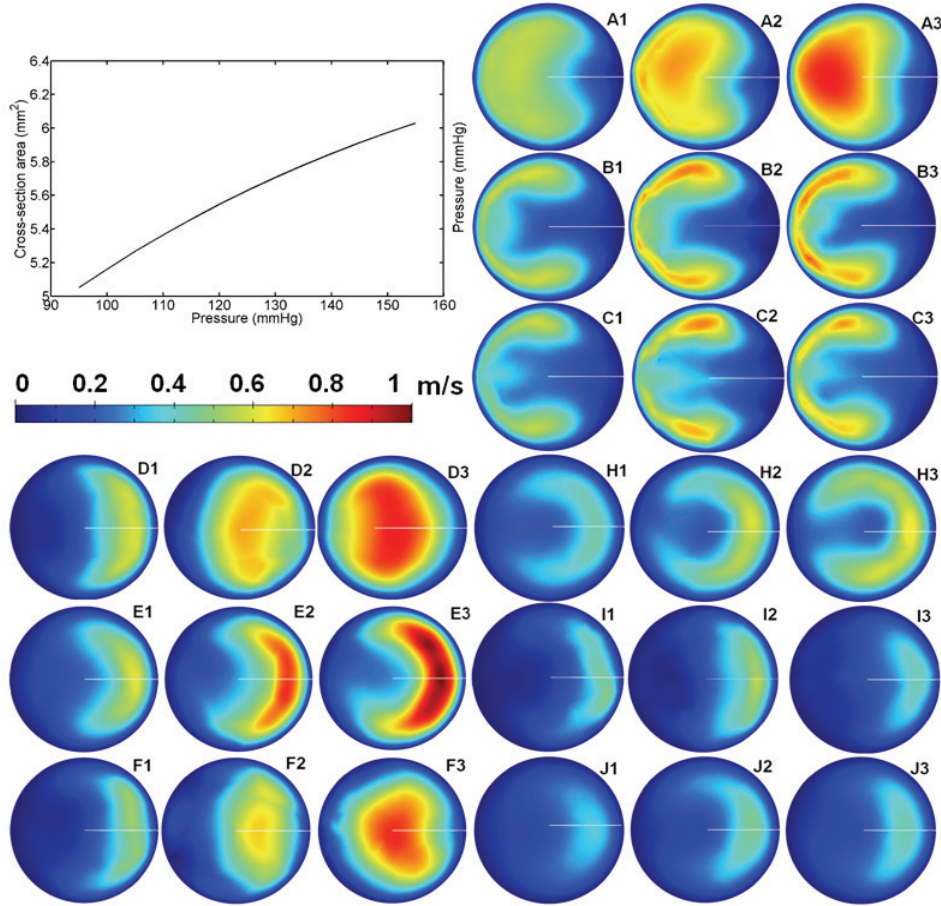


Figure 4.6: The plot of luminal cross-sectional area of ascending aorta versus the pressure sampled from Towfiq et al. (1986). Velocity profiles in the axial cross-sections (see Figure 4.4A) through the aorta and the branches in the geometry G3 at time $t=0.18$ s. Cross-sections A1-J1 correspond to hypotension, A2-J2 to normal pressure, and A3-J3 to hypertension conditions.

4.3 Distribution of WSS in Idealized Aorta Models

Figures 4.7 and 4.8 show the distribution of WSS in the upper aortic arch and the branches of aorta models G1, G2, and G3 at peak systole. It can be noted in Figure 4.9 that at the peak systolic pressure, the distribution of WSS is highly non-uniform in the upper aortic arch and branching region. High WSS was distributed between the branches and on the distal walls of branches. High WSS

can be observed in the proximal part of the branch entry region of respective branches.

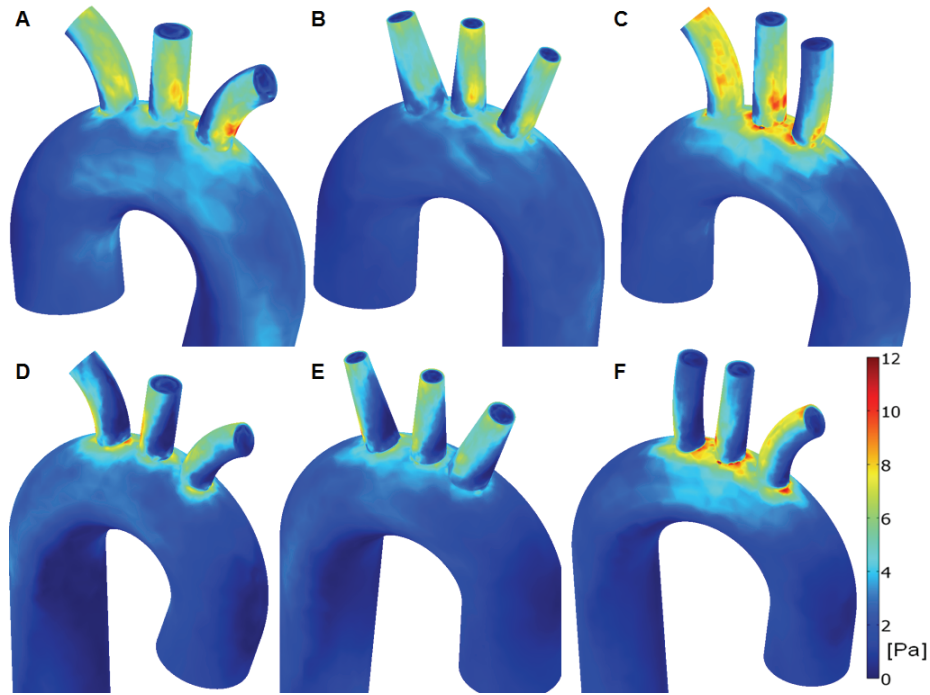


Figure 4.7: Anterior and posterior views showing WSS distribution over the aortic arch and branches for the aorta model G1 (A, D), G2 (B, E), and G3 (C, F) at the maximum systolic pressure time instance $t=0.18$ s.

In Figure 4.8, the posterior view of the aorta models suggests extremely low WSS distributed on the outer wall of the ascending aorta, inner wall of aortic arch, and descending aorta. Extremely low WSS is also distributed on the proximal walls of the branches. The regions of low WSS in the branches are in coincidence with the region where flow stagnation was observed in Figure 4.3. Figure 4.9 contains the polar plots of the circumferential WSS at the axial cross-section for the aorta model G3 at the peak systolic pressure of 120 mmHg. In all the sections, high values of WSS are distributed in quadrants 1 ($0-90^\circ$) and 4 ($270-360^\circ$) and low WSS is distributed in quadrants 2 ($90-180^\circ$) and 3 ($180-270^\circ$). At sections D, F, and I, the distribution of WSS is non-uniform, while at sections E, H, and J, the distribution is smooth and shaped cardioids-like. The non-uniform WSS distribution in sections D, F, and I correspond to the non-uniform distribution of velocity observed in the same sections (see Figure 4.4 D3, F3, and I3). The uniform cardioids shaped WSS profile observed in the sections corresponds to the

C shaped velocity profiles observed in the same sections (see Figure 4.4 E3, H3, and J3). In section J3, the overall magnitude of WSS was lower than observed in sections E3 and H3.

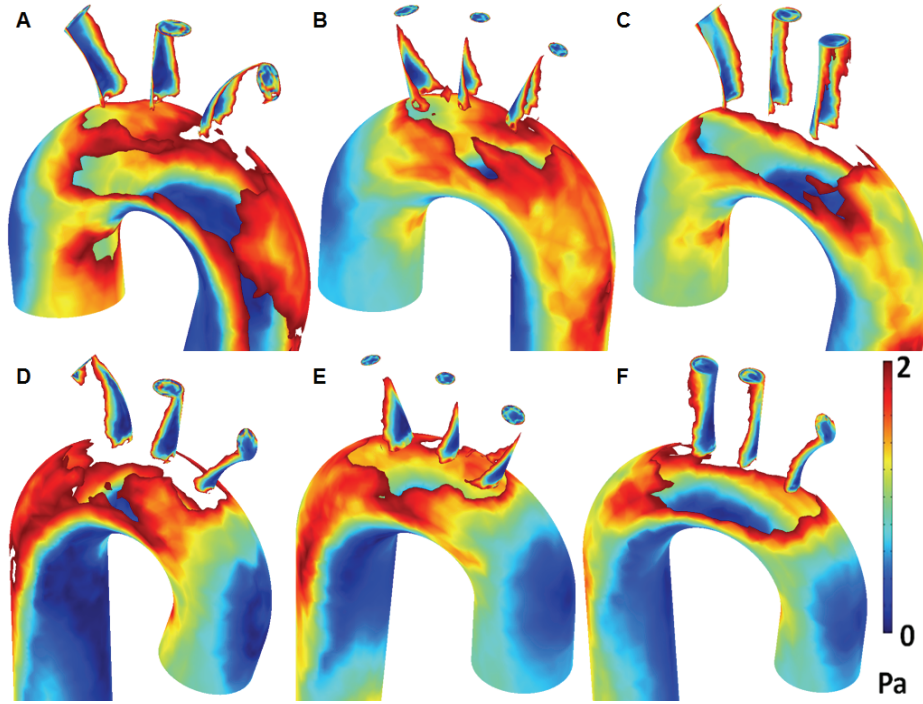


Figure 4.8: Anterior and posterior views showing WSS distribution over the aortic arch and branches for the aorta model G1 (A, D), G2 (B, E), and G3 (C, F) at the maximum systolic pressure time instance $t=0.18\text{ s}$.

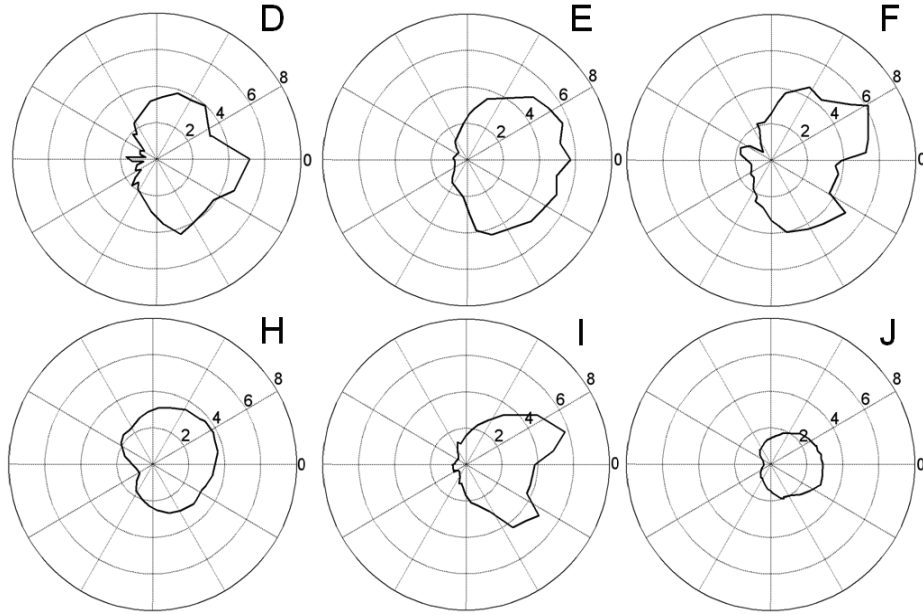


Figure 4.9: Polar plot of peripheral WSS distribution over the sections of the branches of the geometry G1 (D1-J1), geometry G2 (D2-J2), and geometry G3 (D3-J3).

4.3.1 Effect of Hypotension and Hypertension on the Distribution of WSS in the Aorta Model G3

Figure 4.10 shows the distribution of WSS for the aorta model G3 under hypotension, normal pressure condition, and hypertension at the peak systolic pressure time instance $t=0.18$ s. The distribution of WSS is similar in all three cases with high WSS distributed in the upper aortic arch and distal walls of the branches. Figure 4.10 D-I show the details of lower WSS. The anterior view suggests that in all three cases, low WSS is distributed in the outer wall of the ascending aorta and at the inner curvature of the aortic arch.

The circumferential WSS profiles at the axial cross-sections (as shown in Figure 4.4A) are shown in Figure 4.11. It can be noticed that in all the WSS distributions, except D3, higher WSS was distributed in quadrants 1 and 4, and low WSS distributed in quadrants 2 and 4. The WSS distributions at the sections E, H, and J were quantitatively similar. The magnitude of WSS at the sections D2-J2 is higher than that observed at the sections D1-J1. However, the same is not observed for the sections D2-J2 and D3-J3. At the section D3, the WSS is symmetrically distributed on the left and right quadrants. This corresponds to the uniform and

parabolic-like velocity distribution observed in the section D3 in Figure 4. In order to get stable values, WSS is averaged over several sections in each branch of the aorta model G3. Figure 4.12 shows the comparison of average WSS in brachiocephalic, left carotid, and left subclavian branches of the aorta model G3 under hypotension, normal pressure condition, and hypertension. It can be observed that although under hypertension the WSS increases marginally, the overall WSS remains in the same scale and range than under normal pressure conditions. In the brachiocephalic artery and the left carotid artery, the average WSS under hypertension is lower than that under the other two pressure conditions. However, for subclavian artery the average WSS under all the cases is similar. Note that the hypertensive wall is under a higher strain while its shear stress is either unchanged or lower than what normally exists. This can potentially boost the penetration of LDL macromolecules across the arterial wall (Dabagh et al., 2009).

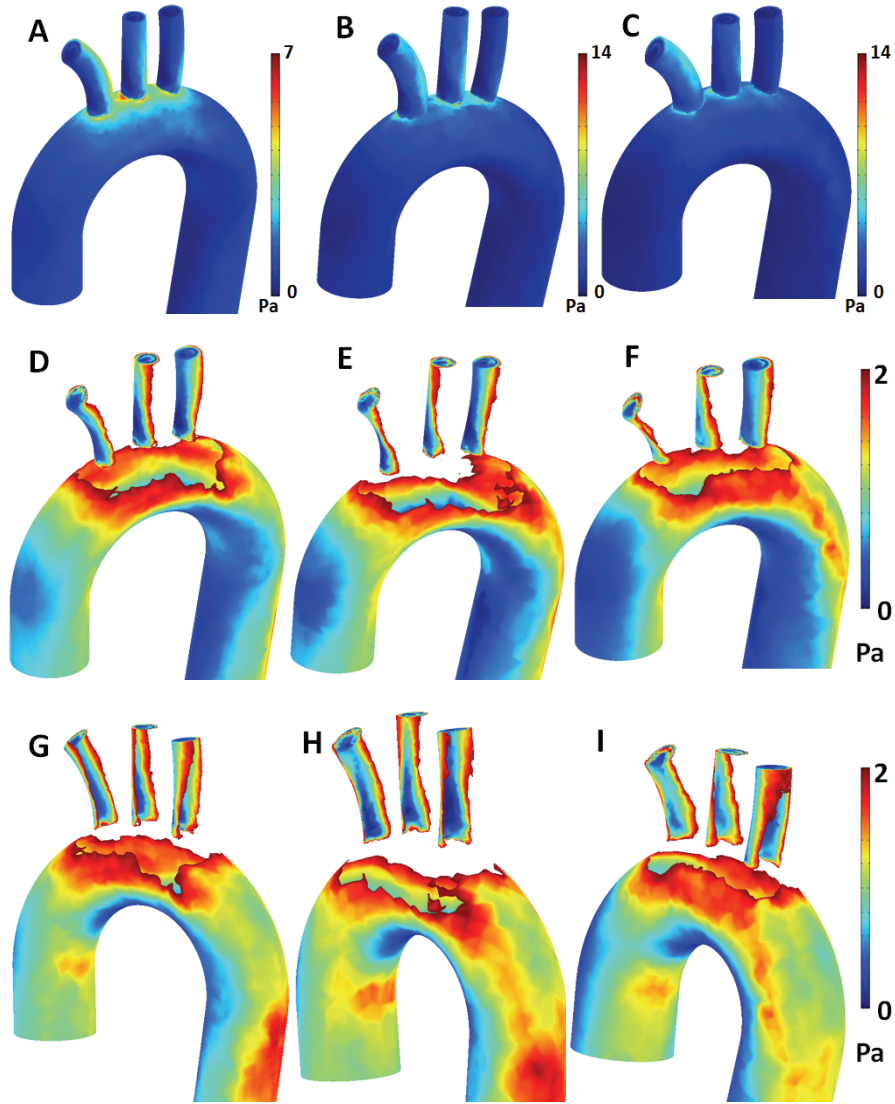


Figure 4.10: Lateral views of the aorta showing WSS distribution over the aortic arch and branches for the aorta model G3 under (A, D, G) hypotension, (B, E, H) normal condition, and (C, F, I) hypertension at $t=0.18$ s.

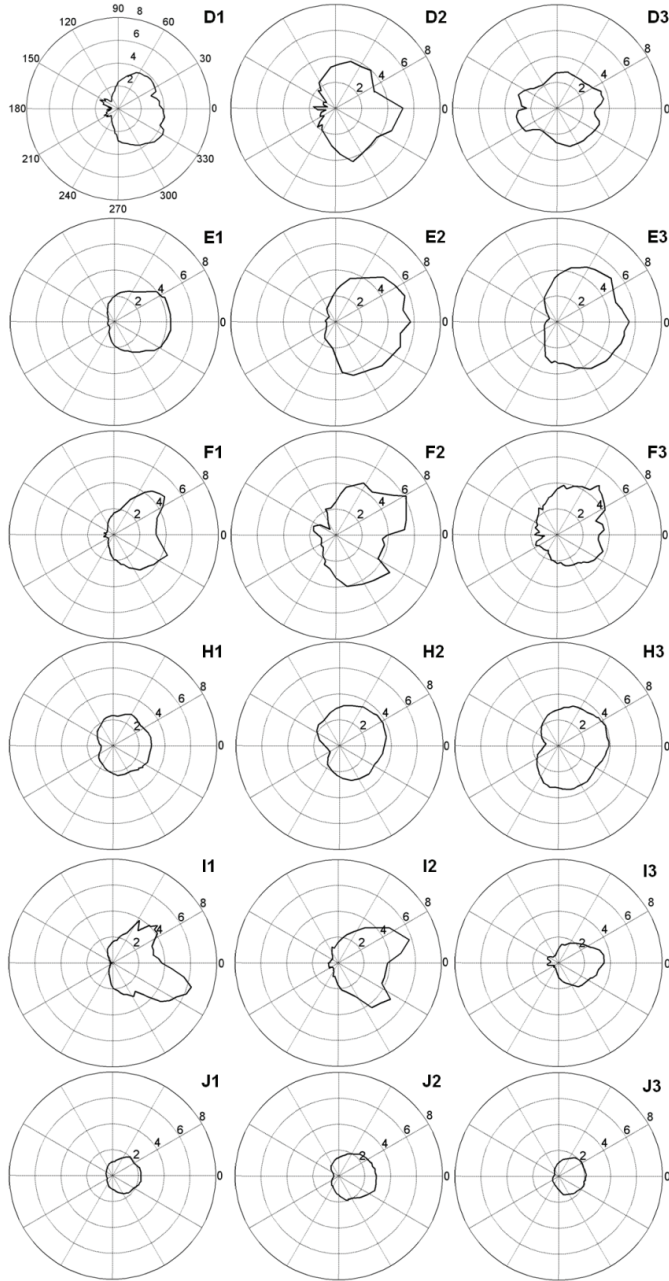


Figure 4.11: Polar plots of peripheral WSS distribution over the sections (D-J) of geometry G3. Cross-sections D1-J1, D2-J2, and D3-J3 correspond to normal pressure, hypotension, and hypertension conditions respectively.

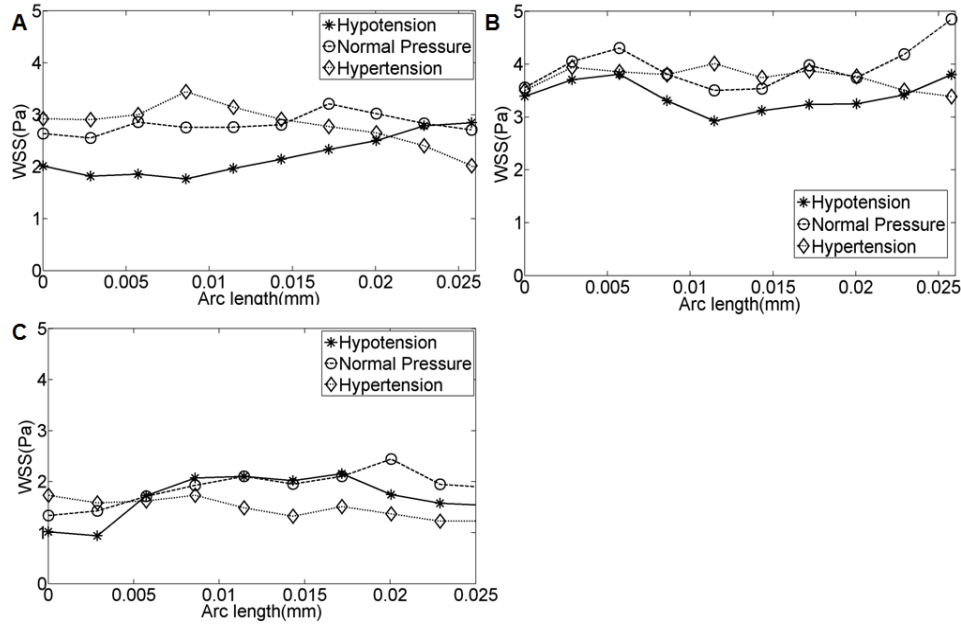


Figure 4.12: The average WSS along the (A) brachiocephalic, (B) left carotid, and (C) left subclavian branches of the geometry G3 at the peak systolic pressure of 80 mmHg (hypotension), 100 mmHg (normal), and 130 mmHg (hypertension) conditions.

4.4 Discussion

Three idealized models of the thoracic aorta were reconstructed using measurements available from the literature. The thoracic aorta models were chosen in such a way that each model has a distinct anatomy in terms of size, aortic arch curvature, and shape of branches, as well as the arch. The aim of this part of the study was to get an estimate of dynamics of blood flow in the real aorta, and understand the characteristics of blood flow dynamics and its dependence on the aorta anatomy and blood pressure. Earlier Towfiq et al. (1986) and Dabagh et al. (2008) have suggested that the aorta size is subjected to the change with blood pressure. However, no attention has been made on studying the corresponding influence on the blood flow features. The idealized aorta model G3 was modified to simulate the flow dynamics in human aorta under the influence of hypotension and hypertension. Though the transient variation of blood pressure within a cardiac cycle causes instantaneous deformation of the aorta wall, which in turn may affect the blood flow features (two-way coupling between the wall

deformation and blood flow), such effects are ignored in this study. With available computational resources the transient simulations with fluid-structure interactions could not be performed. However, the wall deformation relations suggested by Towfiq et al. (1986) could be incorporated by modifying the aorta model G3. Thus, this study seeks the role of aortic arch geometry (with branches) and the mean blood pressure on the resulting transient blood flow only when the wall of aorta is rigid. However, one should note that the corresponding results might be different from what we observed in reality due to the flexibility of the real wall and the complexity of geometry. Nonetheless, we let the wall deform steadily as the mean blood pressure changed.

It has been revealed that atherosclerosis occurs in the regions of low mean shear stress (near separation and reattachment points) where spatial gradients and temporal oscillations of the shear stress are colocalized (Tarbell, 2003). These regions are associated with the curvature and branching in arteries. On the other hand, Dabagh et al. (2008) have considered the aortic wall as a deformable elastic structure with stresses dependent on transmural pressure. It has been also suggested that the deformation of the arterial wall is significant under higher pressures, and assuming the aortic wall as a rigid wall leads to considerable errors in numerical simulations. The intent of this study was to investigate how the differences in the diameter of aortic arch and branches and the curvature of branches affect the distribution of shear stress.

Figure 4.3 shows the distribution of velocity in the symmetry plane in the three aorta models at the maximum systolic pressure of 120 mmHg. In aorta models G1 and G2 the radius of the curvature of the aortic arch is larger than in the aorta models G3. This feature in model geometries of the aorta models G1 and G2 causes skewed flow in the ascending aorta and proximal aortic arch regions. In aorta model the flow bifurcation at the branches dominate the flow with the global maximum velocity observed at the root of B1. The magnitude of velocity at the branch entry region of B1 in G3 is 19% more than that observed in G1 and G2, while the magnitude of the maximum velocity at the entry region of branch B3 of G1 is more than that observed in G2 and G3. Despite the differences in the flow distributions in the aortic arch, the flow stagnation at the inner curvature of the aortic arch and branches are common features in all three aorta models. In G2, the branches and the descending aorta have a tapering effect as a result of which the flow streamlines are overlapping close to the outlets. This can also be observed in the axial flow profiles at sections E2, H2, and J2 in Figure 4.4 where the flow profiles are o-shaped. In G1 and G3, the descending aorta is at an angle of 10 degrees with sagittal plane which offers an additional curvature to the distal aortic arch. This feature of geometry causes the flow in the distal aortic arch to skew towards the inner walls. Figures 4.8 and 4.9 demonstrate the distribution of WSS

in the aorta models G1, G2, and G3, while Figure 4.10 shows the circumferential WSS distributions at the axial cross-sections demonstrated in Figure 4.4A. Despite the differences in the anatomy in all three aorta models, the highest WSS is distributed in the upper aortic arch and branches. It can be noticed in Figure 4.8 that the magnitude of WSS in G2 is the lowest amongst all three aorta models, while the WSS magnitude is the highest in G3. This corresponds to the flow profiles illustrated in Figure 4.3 where in G3, the flow in the upper aortic arch is dominated by the flow bifurcated towards branches. The skewing of velocity in the branches causes the skewness of WSS distribution, as well as the low WSS distributed in the proximal side and the higher WSS distributed in the distal side.

The deformation of the aortic arch and the branches under the hypertension and its influence on the flow dynamics are investigated by the comparison of the velocity and WSS profile under hypotension, normal pressure, and hypertension conditions. Figure 9 show that the pressure affects the WSS distribution and magnitude in the root and outlet of branches in different ways. In the outlets, particularly in cross-sections E and H, the increasing of the pressure raises the WSS significantly. The considerable feature in the results is that WSS decreases under hypertension, at the roots of branches (cross-sections D, F, and I). This in turn highlighted the role of hypertension in the localization of atherosclerosis. The velocity profiles in different cross-sections for three pressure conditions are shown in Figure 4.5. Results reveal that increasing the pressure raises the velocity magnitude in all cross sections. Moreover, the mass flow rate at the outlet of branches increases under higher pressures. A comparison of the mass flow rates reveals that the influence of high pressure on the mass flow rate is greater in the first branch than in the two others. However, the mass flow rate is highly affected by the geometry in the second branch. The deviation of fluid shear stress and other fluid mechanical characteristics from their normal spatial and temporal distribution patterns in straight vessels were observed in the curvature and branching regions. It has been revealed that the aorta is one of the most probable places for arterial wall diseases. The complex geometry of the aortic arch with three branches (brachiocephalic artery, left common carotid arteries, and left subclavian artery) changes the hemodynamic forces locally leading to circumstances associated with the high risk of arterial wall diseases.

5 Results from Realistic Models of Aorta

The results obtained from the numerical simulations of blood flow within realistic models of human thoracic aorta reconstructed from CT images are discussed in this chapter. The time-dependent simulations were performed for four cardiac cycles with FVM based solver Fluent. The results from the 4th cardiac cycle are discussed in this chapter. The distributions of flow, pressure, and WSS are briefly discussed. The chapter concludes with remarks on the use of realistic artery models and differences between flow dynamics observed in the idealized and realistic models of thoracic aorta. The conclusion also contains remarks on the possible gender based risk of atherosclerosis.

5.1 Results from Realistic Aorta Model-1

With an objective of investigating the role of flow dynamics in the localization of atherosclerosis, the distributions of flow, pressure, and WSS are captured at four time instances $t=0.1$ s (Early systole), $t=0.281$ s (Accelerating phase), $t=0.365$ s (Peak Systole), and $t=0.6$ s (Flow reversal) in the cardiac cycle. The numerical simulations were performed with the assumption of rigid arterial walls.

5.1.1 Velocity Distribution in Realistic Aorta Model-1

Figure 5.1 shows the pathlines coloured with the velocity magnitude captured at five time instances. To obtain complete details of the flow fields, axial flow profiles were captured at four axial cross-sections. The axial section-a is in the distal part of the ascending aorta close to the brachiocephalic artery. The second section, i.e. section-b, is located in the aortic arch between the brachiocephalic artery and the left carotid artery, while the section-c is located in the aortic arch between the left carotid artery and the left subclavian artery. The axial flow distribution is resolved into the normal and tangential directions of the aorta trunk. The tangential component represents the motion of fluid within the axial section, i.e. the secondary flow. The normal and tangential components of the flow profiles are displayed separately to investigate the secondary flow motion within the axial cross-sections. The axial velocity profiles at the axial cross-sections are presented in Figure 5.2.

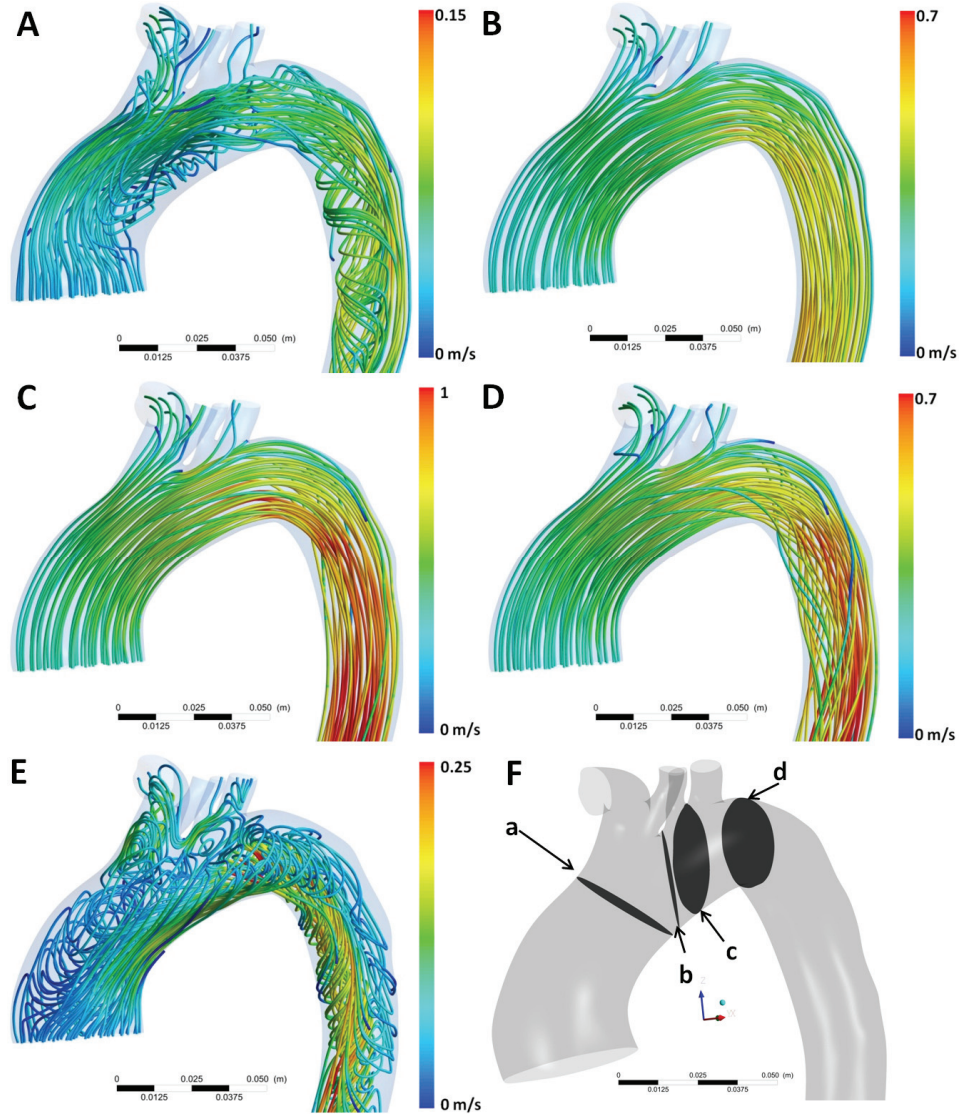
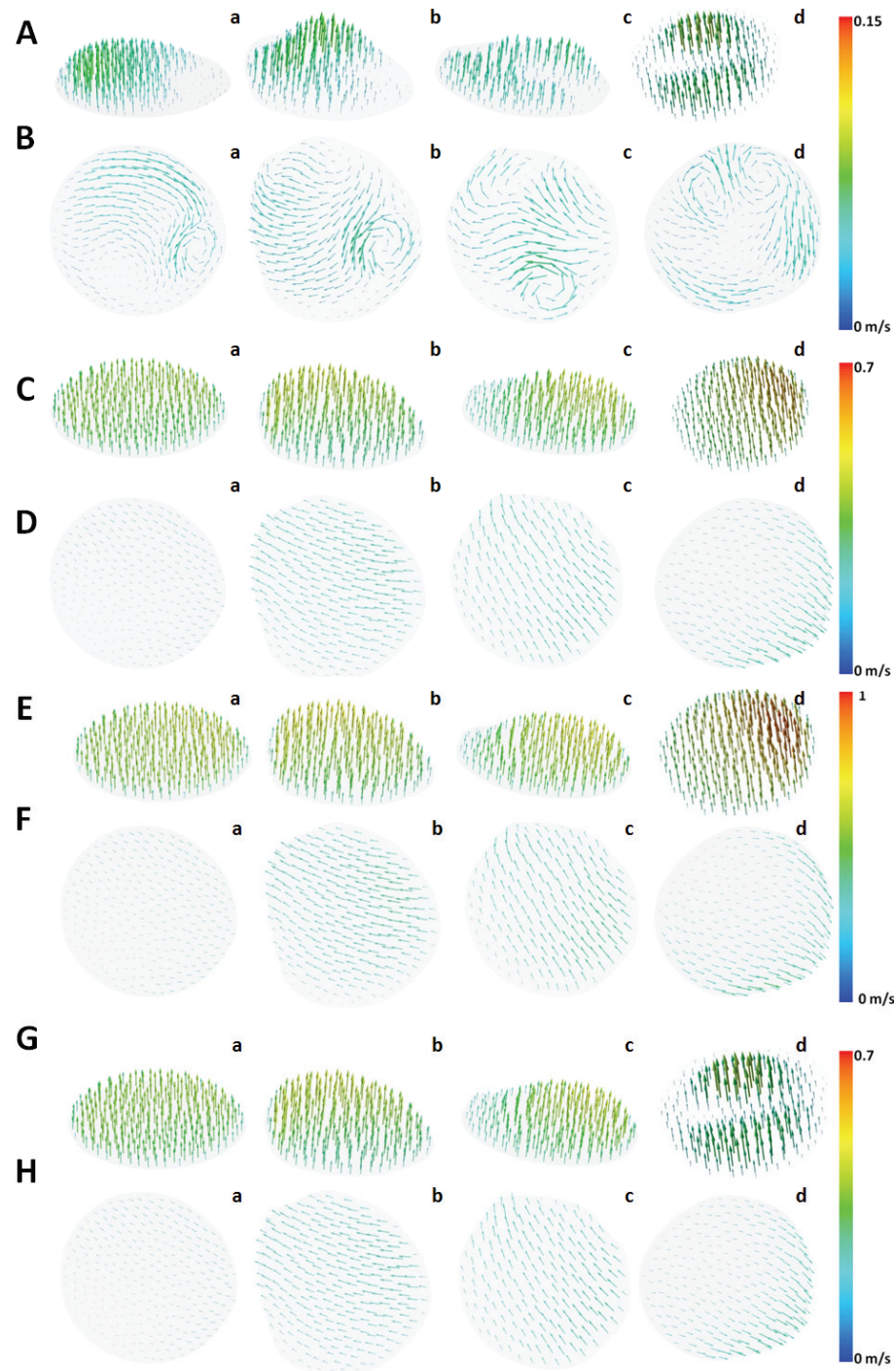


Figure 5.1: The anterior views of R1 showing the pathlines coloured with velocity magnitude at (A) Early systole, (B) Accelerating phase, (C) Peak Systole, (D) Decelerating phase, and (E) Flow reversal. (F) Axial cross-sections in aortic arch of the realistic aorta model R1 where axial flow profiles are captured.

During early systole, the flow in the ascending aorta and the proximal aortic arch is skewed towards the inner wall of the aortic arch with a higher magnitude of velocity localized at the outer curvature of the arch.

The axial flow profiles in Figures 5.2A and B suggests more pronounced secondary flow patterns within axial cross-sections. Two non-identical vortices can be observed in the axial sections in Figure 5. These vortices correspond to the flow circulation in the inner curvature of the aortic arch despite the dominant axial flow. The flow stagnation occurs at the inner wall of the aortic arch and close to the entry region of the brachiocephalic artery. Also helical flow of flow patterns is observed in the distal aortic arch and the descending aorta. During the acceleration phase due to the high accelerations of inflow from the ascending aorta, the secondary flow patterns dissipate and the axial velocity dominates the flow. The axial flow distribution in Figures 5.2 C and D also suggests that though in sections b, c, and d the flow profiles are skewed, the secondary flow motion is negligible. The flow accelerates in the post-branching aortic arch, while downstream at the descending aorta; the flow distribution is almost parabolic. The flow gains a parabolic-like profile which persists through the distal aortic arch and the descending aorta. At the peak systole, the velocity distribution amplifies. The comparison of the axial velocity distribution in Figure 5.2 C with E and D with F respectively suggests that there are no qualitative changes in the flow distributions. During the decelerating phase, the flow distribution in the ascending aorta and the aortic arch is comparable with the flow distribution during the acceleration, but during the deceleration, the helical flow patterns in the descending aorta re-appear. During the flow reversal, the flow distribution is highly non-uniform. The flow in the ascending aorta and the proximal aortic arch is skewed towards the outer wall of the aortic arch with high velocity distributed at the inner wall of the aortic arch. The axial flow profiles in Figures 5.2 I and J suggest secondary flow motion and also reversal in the direction of axial flow. Both the secondary flow patterns and skewness of the flow towards the outer wall of the aorta persist in the descending aorta.



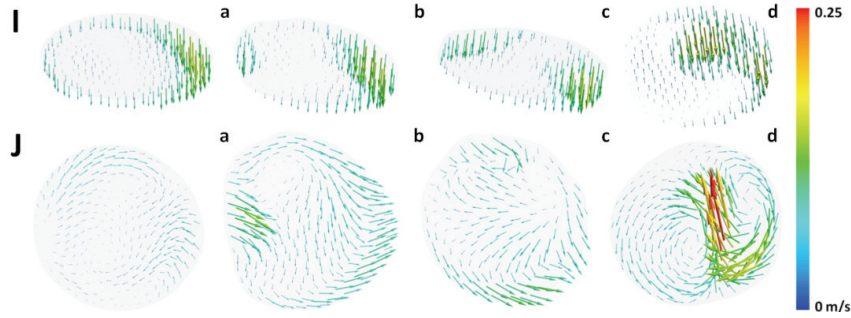


Figure 5.2: The components of the velocity distributions resolved in normal and tangential captured at axial cross-sections demonstrated in Figure 5.1E at time (A, B) Early systole, (C, D) Accelerating phase, (E, F) Peak Systole, (G, H) Decelerating phase, and (I, J) Flow reversal.

5.1.2 Pressure Distribution in Realistic Aorta Model-1

The distribution of pressure in the aorta model R1 captured at five times time instances is illustrated in Figure 5.3. The magnitude of the reported pressure distributions is relative to zero pressure. The pressure drop between the inlet at the ascending aorta and the outlet (at branches and descending aorta) remain positive during the early systole, the acceleration phase and the peak systole. The positive pressure gradient facilitates flow from the ascending aorta to the branching arteries and descending aorta. The distributions of pressure during the deceleration and flow reversal are identical. The pressure gradient is at the maximum during the acceleration phase.

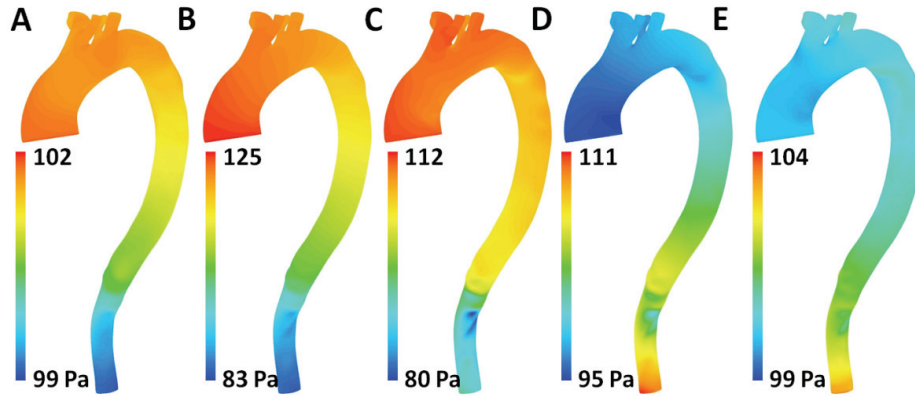


Figure 5.3: The distribution of pressure in the realistic aorta model R1 at (A) Early systole, (B) Accelerating phase, (C) Peak Systole, (D) Decelerating phase, and (E) Flow reversal.

5.1.3 WSS Distribution in Realistic Aorta Model-1

The distribution of WSS in the aorta model R1 captured at mentioned five time instances are shown in Figure 5.4. The WSS distribution is shown via both anterior and posterior views. The overall magnitude of WSS is low during the early systole with the maximum WSS of 1 Pa. The spiral and helical flow distributions in the descending aorta cause the highly non-uniform distribution of WSS in the descending aorta region. During the accelerating phase, maximum WSS is distributed at the root of brachiocephalic artery and the inner wall of the aortic arch. Also during the accelerating phase, minimum WSS is distributed at the branch entry region of all the branching arteries. The magnitude of WSS rises and attains the maximum WSS magnitude during the peak systole. The distribution of WSS remains identical to that during the acceleration. However, like the velocity distribution, the distribution of WSS during the peak systole amplifies. The maximum WSS of 19.8 Pa was observed at the inner aortic arch. The posterior views of the acceleration phase and peak systole also suggest high WSS distributed in the inner wall of the descending aorta. In the proximal aortic arch, higher WSS is observed in the inner aortic arch, while low WSS is distributed on the outer wall. Unlike the flow profiles, the distributions of WSS during the deceleration and the acceleration are not identical. The effect of helical flow patterns on the distribution of WSS is clearly visible in Figure 5.4G. At the flow reversal time, the distribution of WSS is highly non-uniform. The anterior and posterior views suggest high WSS distributed at the proximal part of the junction of branching arteries and aortic arch, while low WSS is distributed at the proximal part of the junction of branching arteries and aortic arch. However, the

scale of the WSS is much lower compared to the WSS during the accelerating phase and the peak systole. Highly non-uniform distribution of WSS is observed in the upper aortic arch and branching regions. The anterior view suggests that the minimum WSS occurs at the inner curvature of aortic arch, branching of arteries and the inner curvature of the descending aorta. The posterior view suggests that the minimum WSS occurs at the bifurcation of the right common carotid artery and right subclavian artery, as well as on the outer curvature of right subclavian artery. The maximum WSS is observed at the inner curvature of aortic arch and all branches. The regions' maximum and minimum WSS migrate locally with variation in pressure indicating fluctuation of local WSS with time. The sites with low and fluctuating WSS are vulnerable for the development of arterial diseases, such as atherosclerosis.

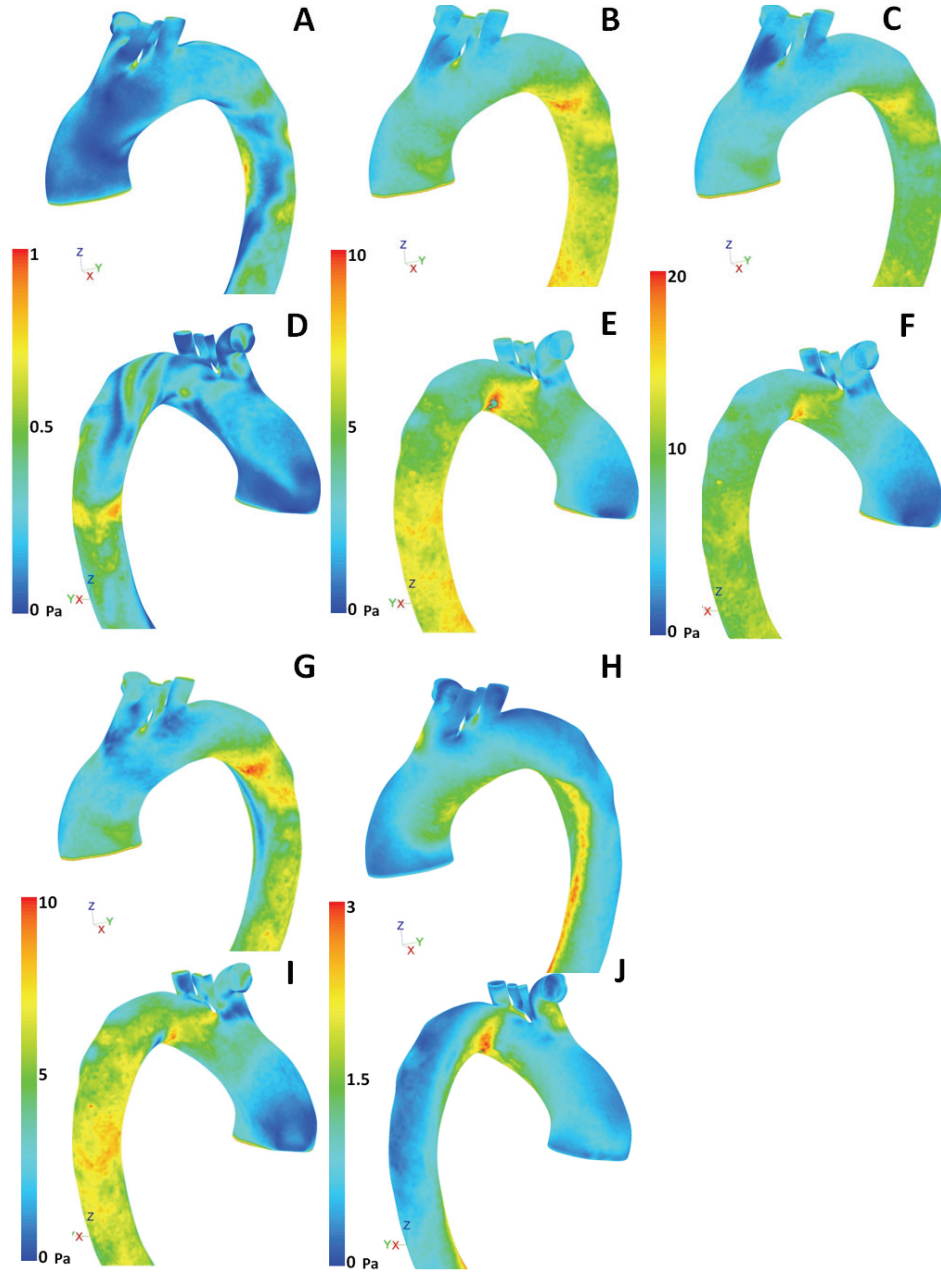


Figure 5.4: The anterior and posterior views of R1 showing the distributions of WSS at (A, D) Early systole, (B, E) Accelerating phase, (C, F) Peak Systole, (G, I) Decelerating phase, and (H, J) Flow reversal.

5.2 Results from Realistic Aorta Model-2

In the following sections, the distributions of flow, pressure, and WSS captured at five time instances $t=0.1$ s (Early systole), $t=0.281$ s (Accelerating phase), $t=0.365$ s (Peak Systole) and $t=0.6$ s (Flow reversal) during the cardiac cycle are discussed briefly. The numerical simulations with the real aorta model R2 were also performed with the assumption of rigid arterial walls.

5.2.1 Velocity Distribution in Realistic Aorta Model-2

The streamlines and axial velocity distributions captured at five time instances are illustrated in Figures 5.5 and 5.6, respectively. The streamlines captured during the early systole suggest a skewed velocity distribution in the ascending aorta and the aortic arch. This feature of the flow is also observed in the axial flow distribution shown in Figures 5.6 A and B. The axial flow pattern shows high velocity distributed towards the outer wall of the aortic arch and low WSS distributed at the inner wall of the aortic arch.

The tangential projections of the axial flow also implicate flow circulation within the axial sections a, b, and c. In addition to the secondary flow patterns, flow stagnations occur at the inner aortic arch and in the vicinity of branch entry regions of all three branching arteries. At the peak systole, helical type of flow is observed in the descending aorta. Similar to R1, the flow distributions during the acceleration amplifies. The axial velocity distributions are uniform without the effect of secondary flow within the axial sections. The effect of secondary flow patterns vanishes while the flow in the descending aorta gains a uniform parabolic shape, although minor skewness in the flow distributions is observed at axial sections a, b, c, and d located in the aortic arch trunk. The distribution velocity further amplifies during the peak systole. The axial flow distributions show that the flow distribution is parabolic like with high velocity distributed in the centre of the sections. The helical flow patterns in the descending aorta reappear during the decelerating phase. The flow distribution in the rest of the aorta remains qualitatively similar to that during the peak systole.

The flow distribution during the flow reversal is almost turbulent. The picture of streamlines suggests high velocity distributed in the inner wall of the aortic arch. The flow circulation occurs at the outer wall of the distal aortic arch and in the proximity of the branch entry region of all the branches. Despite the low magnitude of the velocity, the highly disturbed flow is expected to significantly affect the WSS distribution.

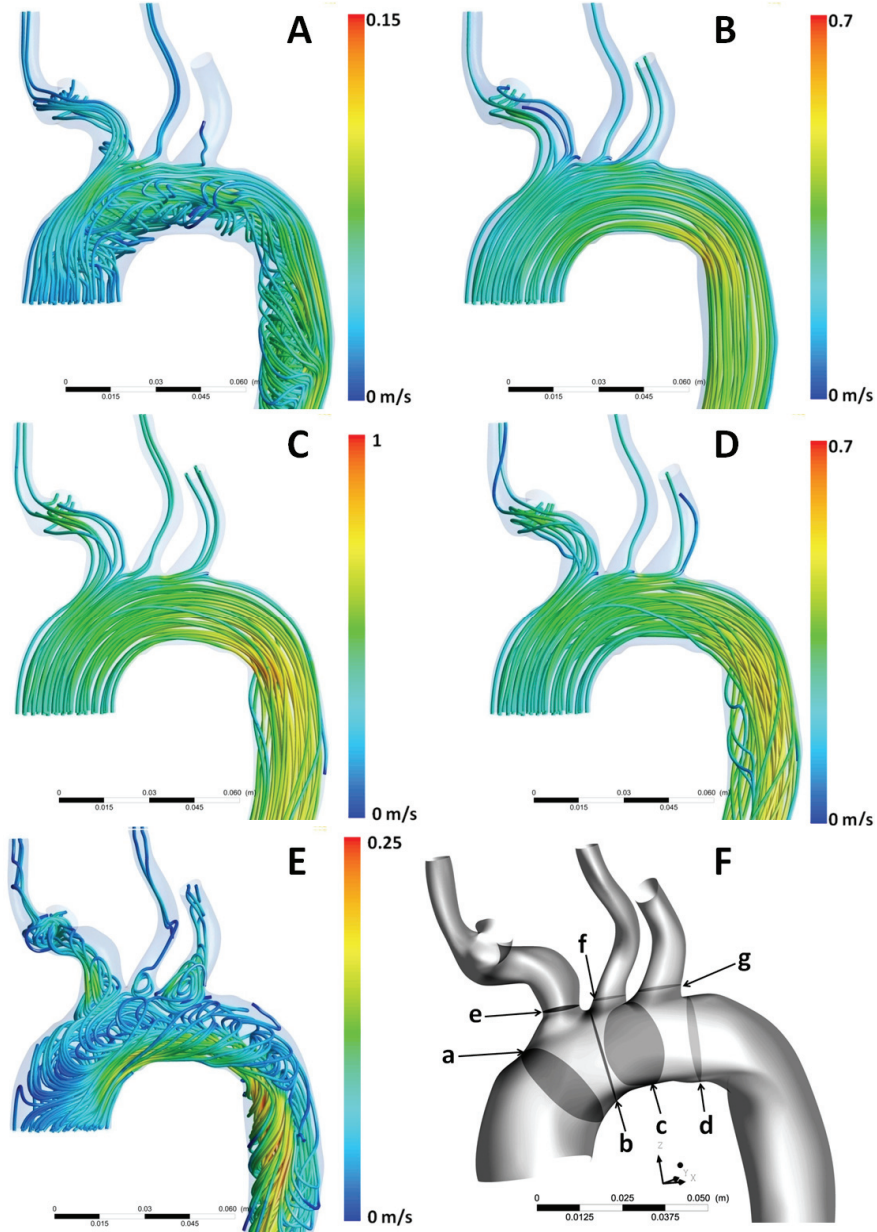
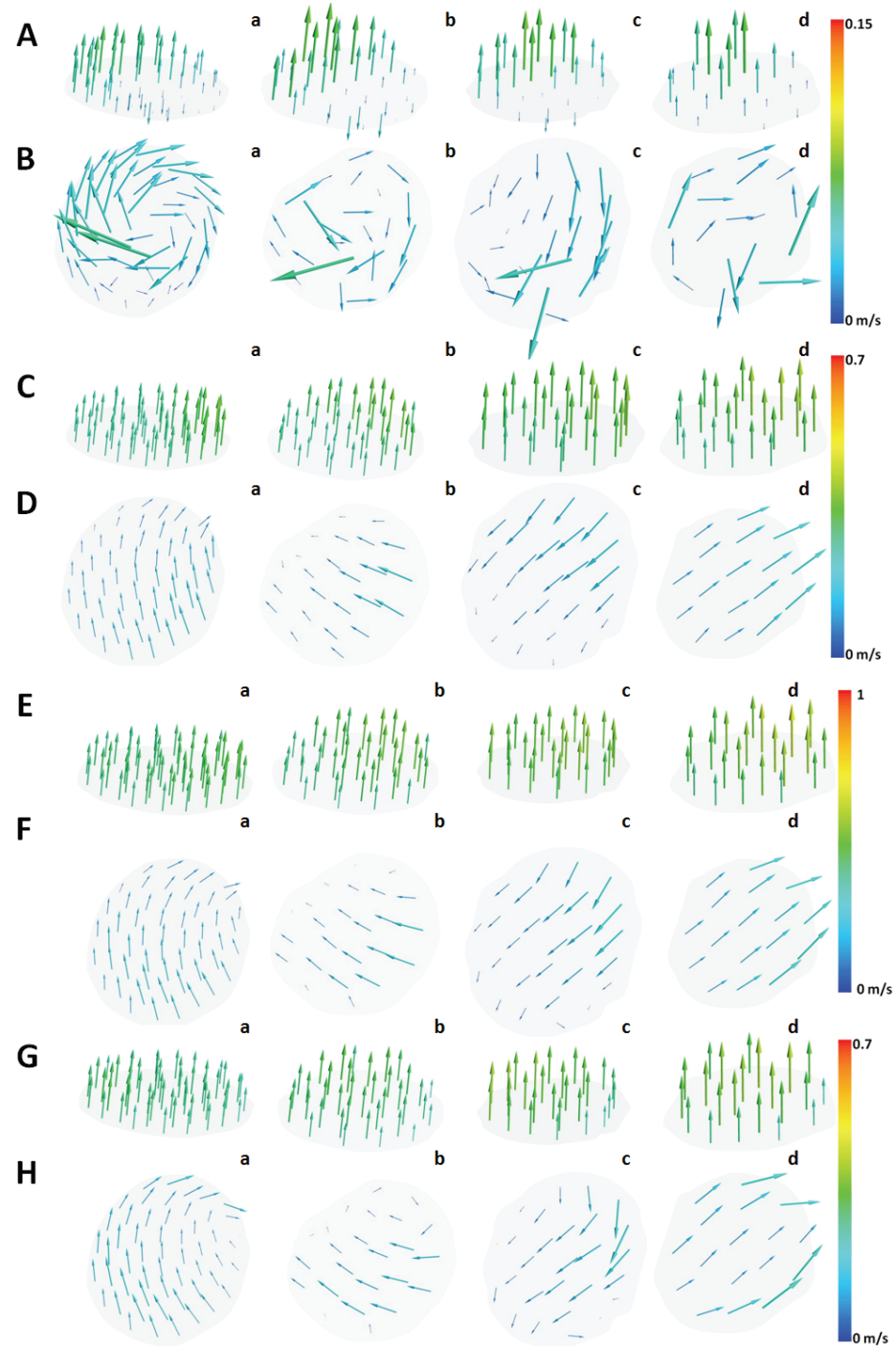


Figure 5.5: The anterior views of R2 showing the pathlines coloured with velocity magnitude at (A) Early systole, (B) Accelerating phase, (C) Peak Systole, (D) Decelerating phase, and (E) Flow reversal. The axial cross-sections where the flow profiles were captured.



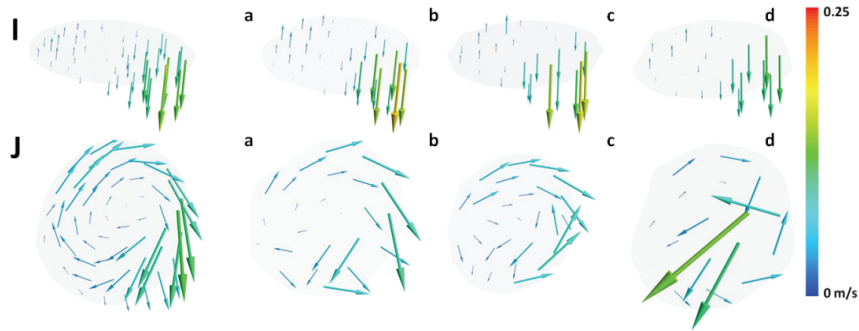


Figure 5.6: The components of the velocity distributions resolved in normal and tangential captured at the axial cross-sections at time (A, B) Early systole, (C, D) Accelerating phase, (E, F) Peak Systole, (G, H) Decelerating phase, and (I, J) Flow reversal.

5.2.2 Pressure Distribution in Realistic Aorta Model-2

The distributions of pressure at five time instance in a cardiac cycle are shown in Figure 5.7. The magnitude of the reported pressure distributions is relative to zero pressure. The distributions of pressure in R2 are comparable to the pressure distributions in R1 at respective time instances. During the early systole, the acceleration phase, and the peaky systole, the pressure drop is positive from upstream towards downstream, due to the positive and accelerating inflow from the ascending aorta, while during the deceleration and flow reversal, the direction of pressure gradient alters, due to the decelerating flow and flow reversal.

The pressure drop between the inlet and outlets during the early systole is negligible due to the low amount of inflow from the ascending aorta. The pressure gradient during the acceleration elevated to facilitate the acceleration. The pressure gradient reduces by 13 Pa during the peak systole. During the accelerations phase, the pressure gradient between the ascending aorta and outlets at branches and the descending aorta is negative to facilitate the acceleration. During deceleration, the direction of pressure gradient is reversed and also the pressure gradient drop. The pressure drop observed in R2 is smaller than that observed in the respective time instances in R1.

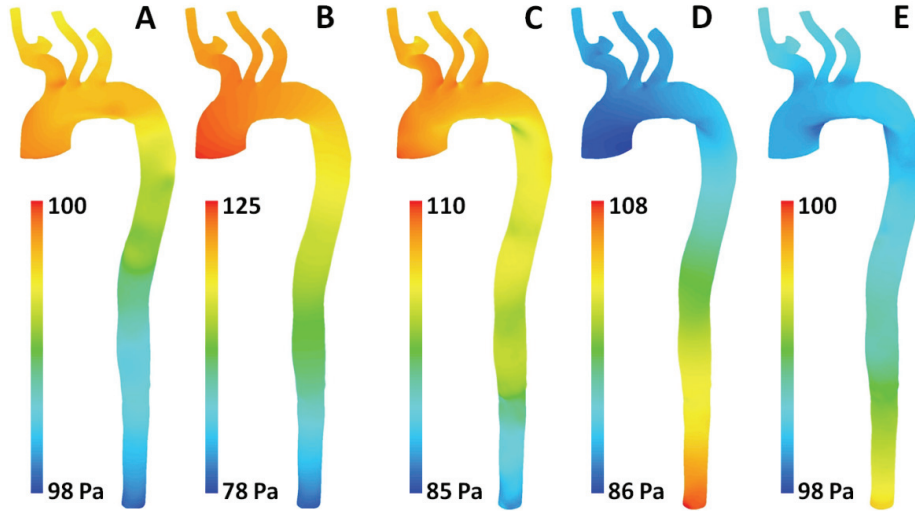


Figure 5.7: The distribution of pressure in the realistic aorta model R1 at (A) Early systole, (B) Accelerating phase, (C) Peak Systole, (D) Decelerating phase, and (E) Flow reversal.

5.2.3 WSS Distribution in Realistic Aorta Model-2

The distribution of WSS in the aorta model R2 captured during the cardiac cycle is shown in Figure 5.8. The distribution of WSS is expected to be different from the realistic aorta model R1 due to variations in the aorta geometry and also variations in flow dynamics. The branches of the aorta model R2 are longer, and thus more details will be made available for the analysis of flow through the branches. The brachiocephalic artery makes an almost 90 degrees angle after branching from the aortic arch. This feature is expected to influence the flow especially in the brachiocephalic artery, left common carotid artery, and left subclavian artery.

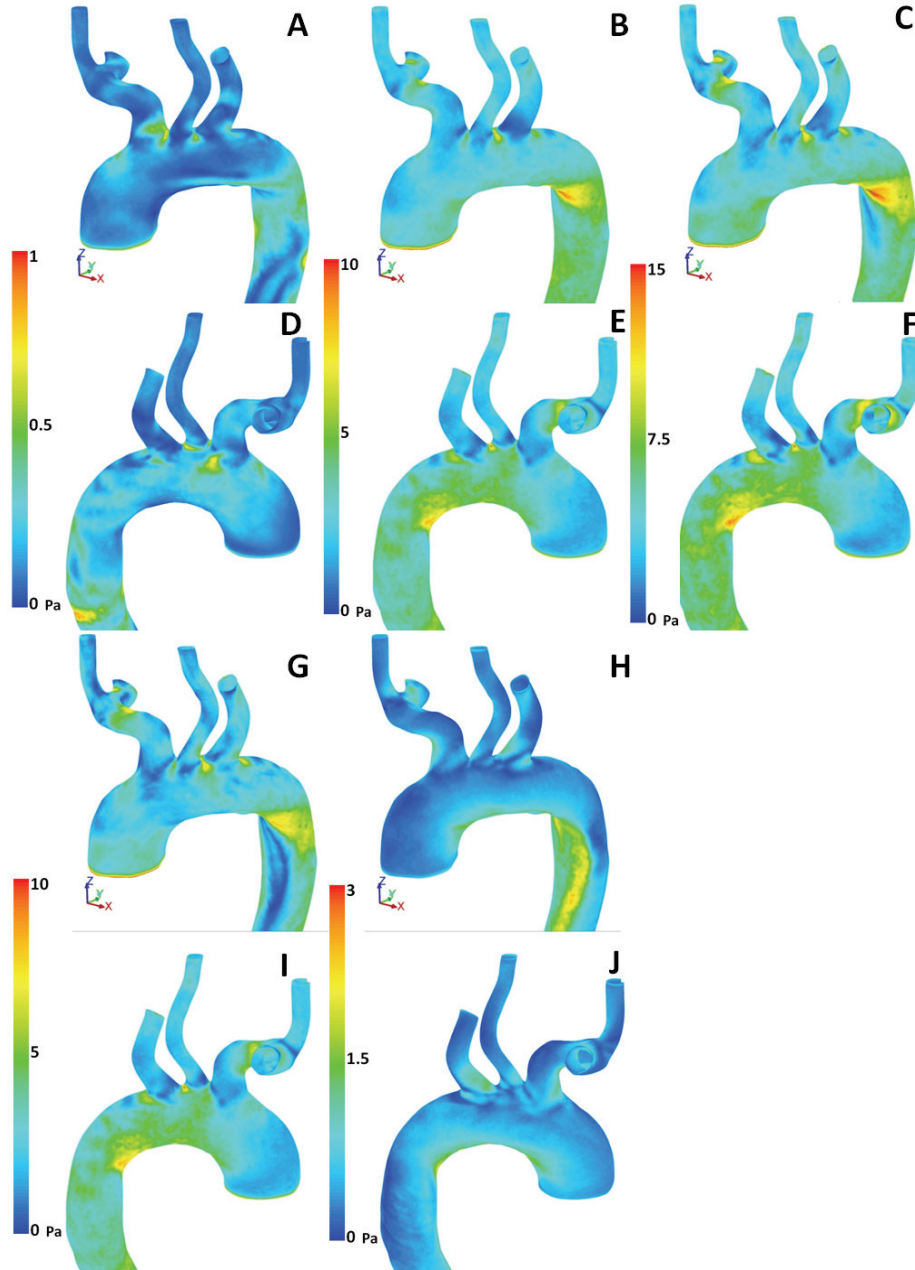


Figure 5.8: The anterior and posterior views of R1 showing the distributions of WSS at (A, D) Early systole, (B, E) Accelerating phase, (C, F) Peak Systole, (G, I) Decelerating phase, and (H, J) Flow reversal.

The overall magnitude of WSS is very low during the early systole, due to the low inflow from the ascending aorta. During the early systole, higher WSS is distributed on the upper aortic arch (between the branches) and inner wall of the distal aortic arch. Close to the branch entry region, extreme WSS is distributed on the proximal side and distal side of the branching arteries. The posterior view also suggests that extremely low WSS is distributed in the right subclavian artery. The posterior view of the WSS distribution during the early systole shows higher WSS distributed on the posterior side of the brachiocephalic artery, while extremely low WSS is distributed on the proximal side of the brachiocephalic artery. The non-uniform distribution of WSS at the brachiocephalic artery is also due to the flow cavitation and bifurcation of flow in the vicinity of the branch entry region of the brachiocephalic artery. With the acceleration of inflow, the magnitude of WSS is elevated. During the acceleration, high WSS of 10.2 Pa is distributed in the upper aortic arch (close to the right carotid artery) and the inner curvature of the distal aortic arch. In the given aorta model, the brachiocephalic artery further bifurcates into the right carotid artery and right subclavian artery. High WSS measuring about 8 Pa is also observed at the bifurcation of the right carotid artery and right subclavian artery. Extremely low WSS is distributed close to the entry region of branching arteries. During the peak systole, the distribution of WSS remains qualitatively similar to that during the acceleration, although the magnitude of the maximum WSS rises to 16 Pa. The magnitude of WSS drops during the deceleration with the maximum WSS of 9 Pa distributed in the inner wall of the distal aortic arch region. The effect of helical flow patterns in the descending aorta observed in Figure 5.5D is clearly visible in the WSS distribution in the anterior view. The distribution of WSS is highly non-uniform during the flow reversal.

5.3 Discussion

Two realistic models of thoracic aorta were constructed from CT images using medical and CAD computer codes. The numerical simulations of blood flow in the realistic models of thoracic aorta including four major branches were conducted with FVM based computer code. A flat inlet pulsatile velocity profile was deployed as inlet boundary condition in both the simulations. This boundary condition has been used in the earlier works, such as Shacheraghi et al. (2002) and Kim et al. (2004). The simulations were conducted with four cardiac cycles. The distributions of flow, pressure, and WSS were studied at five time instances in 4th cardiac cycle to understand the role of flow dynamics in the localization of atherosclerosis.

The analysis of results revealed a highly complex and non-uniform distribution of flow dynamics in the thoracic aorta. The distribution of flow and WSS were significantly different than those observed in the idealized models in Chapter 4. The flow dynamics within the artery is heavily driven by the anatomy of the respective artery. The axial flow distribution shown in Figures 4.4 and 4.6 are almost symmetric over the coronal plane. The aorta models used in these works had a uniform area of cross-section in the main trunk of the aorta and the branches. The planar and symmetric nature of the aorta models coronal plane can be blamed for the symmetric flow patterns in the axial cross-sections. Such symmetry in the flow distribution is also seen in the original work by Shahcheraghi et al. (2002), Kim et al. (2004) and Park et al (2007). However, owing to the complex, non-planar, and non-symmetric nature of the realistic aorta, the flow distributions shown in Figure 5.2s and 5.6 are not symmetric over the sagittal or coronal plane. The flow distributions in the idealized models are significantly different from those in the realistic models. Another feature which causes unrealistic flow patterns is the sharp edges at the branch entry region. Due to the lack of exact measurements, most works with idealized aorta models have assumed the branch entry region to be with sharp corners. This feature of the aorta model coupled with the pressure type of boundary condition imposed at outlet caused accelerated flow at the branch entry region. The accelerated flow at the branch entry region is demonstrated in Figures 4.3 and 4.5. The sharp edges at the branch entry region also caused flow stagnation and flow separations in the vicinity of the branch entry region. In reality, the branch bifurcations have smooth and blunt corners which tend to assist the blood flow. It can be noticed in Figures 5.1 and 5.5 that even during the acceleration and the peak systole, the flow in the branching region did not accelerate as in the idealized cases.

The difference in flow dynamics due to the difference in anatomy is intuitive. While the comparison of flow dynamics within the realistic and idealized aorta models are qualitatively conclusive, it is therefore strongly recommended to use image based aorta models which include the actual anatomy of the thoracic aorta. The results obtained from the realistic model of the aorta are more reliable than the results based on idealized models. Although with just two aorta models, an extensive discussion on the effect of anatomy on flow dynamics is beyond the scope of this study, but the differences and the common feature of flow anatomy are discussed briefly. For numerical experiments with R1 and R2, a flat inlet velocity profile was used as inlet boundary condition. As the flow moves downstream, it exhibits significant skewing, secondary flow pattern and cavitation in the proximal aortic arch region. The primary flow distributions shown in R1 and R2 were qualitatively similar. During the early systole, there is flow stagnation at the inner wall of aortic arch and close to the branch entrance region. During the acceleration, the peak systole and the deceleration phase, the flow is

uniform, although the secondary flow patterns perish, but the flow in the aortic arch remains skewed towards the inner wall of the aortic arch. Also during the deceleration the flow in the descending aorta exhibits the helical motion, while during the flow reversal, the flow is almost turbulent.

The realistic aorta models R1 and R2 were significantly different in anatomy. The major differences between the aorta models are the length of the major branches and the curvature of the aortic arch. The aortic arch in model R1 has larger curvature than that in R2; the length of the branching arteries in R2 is longer than in R1. Despite the short branches of R1, the length of the brachiocephalic artery is long enough to include the bifurcation of the right carotid and the right subclavian artery. Also R1 has a larger area of cross-section of the trunk than that in R2. The branching arteries in R1 are orientated in the same direction as that of the aortic arch, while in R2 the branching arteries are oriented almost perpendicular to the aortic arch. Despite this difference, both in R1 and R2, the brachiocephalic artery makes a 90 degree bend towards the posterior side. In R1, the extreme bend occurs after the bifurcation, while in R2 it occurs before the bifurcation.

Although the primary flows demonstrated in Figures 5.1 and 5.5 are qualitatively identical, the differences in the anatomy of R1 and R2 caused significant differences in the axial flow, especially in the secondary flow motions within the axial sections. Due to the larger curvature and large area of cross-section, the secondary flow patterns are more prominent in the axial flow patterns in R1 than in R2. In Figures 5.2A and J, the normal flow distributions appear with two vortices, while in Figures 5.6A and J, the axial flow has only one vortex with low velocity distributed in the centre. Although in R1 and R2 during the acceleration, peak systole, and deceleration, the secondary flow motion perishes, the axial flow distribution in the aortic arch is more skewed towards the inner wall of aortic arch in R2 than in R1. Despite the fact that the branches in model R1 were shorter than those in model R2, the use of similar boundary conditions allowed the comparisons of flow dynamics in both models. The outflow type boundary condition was the only boundary condition that could be deployed irrespective of the length of branches. Although the length of the branches in R1 was shorter than that in R2, the distribution of pressure was similar in R1 and R2, but due to the shorter branches of R1, flow stagnation and recirculation could not be observed. In R2, flow stagnation and recirculation occurred in the brachiocephalic artery and left subclavian artery. The helical flow in the descending aorta during the deceleration was the common feature in both aorta models.

The distribution of WSS in R1 showed the maximum WSS distributed at the branch entrance region of the brachiocephalic artery and the inner wall of the distal aortic arch. In R2, the maximum WSS is distributed at the branch entry

region of the left carotid artery, left subclavian artery, and inner wall of the distal aortic arch. In both aorta models, during the acceleration, peak systole and deceleration extremely low WSS is distributed at the bifurcation of the brachiocephalic artery. Also low WSS in the proximal part of branching and high WSS in the distal parts of the branching is common in both models. These results are in agreement with the results obtained by Liu et al. (2010) and Zhou et al. (2010). Liu et al. (2010) have simulated blood flow in a realistic aorta model with and without torsion in the ascending aorta. The comparison revealed that the high WSS remains distributed in the distal aortic arch irrespective of the torsion.

From the results shown in the above section it can be concluded that the flow and WSS distributions in the aorta are due to the complex anatomy of aorta. The complex flow dynamics is believed to have a significant effect on material transport, e.g. oxygen, LDL, through the arterial wall. The use of two aorta models allowed the comparison of flow dynamics in two individuals. The low and fluctuating shear stress in the branching arteries and aortic arch can cause the localization of atherosclerosis in these locations. The earlier studies have established that atherosclerosis is prone to develop in site in the arteries with low and fluctuating WSS. It has also been shown that the dynamics of the blood flow and distribution of shear forces heavily depend on the local anatomy of arteries. Finally, we must emphasize the use of realistic models of arteries to obtain accurate and reliable results. The validity of results heavily depends on how close an artery model is to the real artery. Although, the assumption of rigid artery wall and the neglecting of mass transport through the artery wall are the measures of simplification of the current work. Currently, work is in progress to overcome these simplifications.

6 Results from Thoracic Aorta Models with Artificial Stenosis

Based on the WSS distribution, in the realistic model R2, artificial stenosis was introduced at the location of low and fluctuating WSS. Artificial stenosis of 50% severity was introduced close to the branch entry regions in the brachiocephalic artery, common carotid artery, left subclavian artery, and aortic arch. To investigate the effect of stenosis, the shape, symmetric, and asymmetric type of stenosis profiles were used. The chapter begins with a note on the shape of the stenosis and is continued by discussion on the effects of the shape of stenosis on the distribution of WSS. In the previous chapter, it was observed that during the peak systole, the distribution of WSS is the most pronounced, thus only the distributions of WSS for the peak systole time are discussed in detail. To study the variation in WSS at the neck of the stenosis, peripheral WSS was captured at the neck of stenosis at 5 time instances in the cardiac cycle. The chapter continued with the section about the distribution of WSS in the branch entry region with asymmetric stenosis. This brief analysis is made to study the effect of the shape of stenosis. In addition to stenosis in the branches, numerical simulations were also performed in the aorta models with the stenosis in the aortic arch. This chapter also includes sections about the distribution of WSS in cases with the stenosis in the aortic arch. Finally, the chapter concludes with remarks on flow dynamics within the thoracic aorta with stenosed branches, the effect of stenosis blockage severity on WSS, and the risk of rupturing of stenosis plaque.

6.1 Atherosclerotic plaque in aortic arch and branches

There have been numerous studies about flow dynamics within the arteries under the influence of stenosis (Bark and Ku 2010, Lee et al. 2008, Li et al. 2007, Huang et al. 2010, Olgac 2010). These works have been focused on small and medium sized arteries. Although the aorta has been cited as most vulnerable to the localization of stenosis, not much attention has been paid to study the flow dynamics in the aorta with stenosis. This part of the study is a primitive attempt of investigating the flow dynamics in the aorta with stenosis at the branch entry region of three branches and the aortic arch.

Atherosclerosis is prone to develop in the location with low or fluctuating shear stress. The present study of blood flow in human thoracic aorta is further extended by the introduction of artificial stenosis at the branch entrance region in major branching arteries. The effect of stenosis is introduced by simply reducing the

diameter of the artery, as proposed by Ku (1997). The simple equation used for calculating the severity of stenosis is:

$$Stenosis \% = \left(\frac{D_{before} - D_{after}}{D_{before}} \right) 100 \quad (6.1)$$

Where D_{before} and D_{after} are the diameters of artery before and after stenosis.

In simulations with healthy aorta models, the WSS at the branch entrance region and inner aortic arch varies significantly during a cardiac cycle. Therefore, it was concluded that the branch entry region is the site vulnerable to develop atherosclerotic plaque, and thus artificial stenosis was introduced at the branch entry region of the three major branches. The aorta models with stenosed arteries were constructed using the image processing and CAD operations described in Chapter 2. To introduce the artificial plaque, the contours obtained from image processing operations were altered. The contours of the branching arteries were deflated in order to reduce the area of cross-section by 50%.

The operation of deflating was performed carefully to preserve the original shape of the contour. To introduce asymmetric plaque, the deflating operation was performed in such a way that the actual and deflated contours are in the same centre line of the artery. Earlier Kaazempur et al. (2005) and Valencia and Baeza (2009) have revealed that the flow dynamics is significantly affected differently in the arteries with symmetric and asymmetric plaques. Thus, it was also decided to introduce asymmetric atherosclerotic plaque in the branching arteries. The asymmetric plaque was introduced in two steps. In the first step, the contours obtained from the image processing were deflated as described in the previous paragraph. In the second step, the deflated contours were shifted towards the distal walls of the branches. This operation ensured that the deflated contours are in alignment with the distal walls of the respective branches. This approach was adopted from the works of Ohayon et al. (2008) and Floc'h et al. (2010). Figure 6.1 illustrates the stenosis plaque profiles created at the branch entrance region of the aorta model R2.

In addition to the aorta with stenosed branched, artificial stenosis was also introduced at the inner wall of the aortic arch. The idea was inspired from the work by Huang et al. (2010). The inner wall of the aortic arch has also been cited as vulnerable to the localization of atherosclerosis plaque. The flow dynamics with the aortic arch with atherosclerotic plaque has rarely been studied. Huang et al. (2010) used idealized models of aortic arch with a regular radius of curvature which had a uniform area of cross-section. The stenosis model used by Huang et

al. (2010) was also in the shape of an ellipse. Huang et al. (2010) concluded that the flow behavior undergoes a significant modification due to the stenosis in the aortic arch. Introducing a regular stenosis in the aortic arch model R1 was not possible, since the CT images used for the reconstruction of aorta model R2 were transverse images. In order to introduce the artificial stenosis, the contours located at the inner aortic arch were altered manually in such a way that the area of cross-section was reduced by 50%.

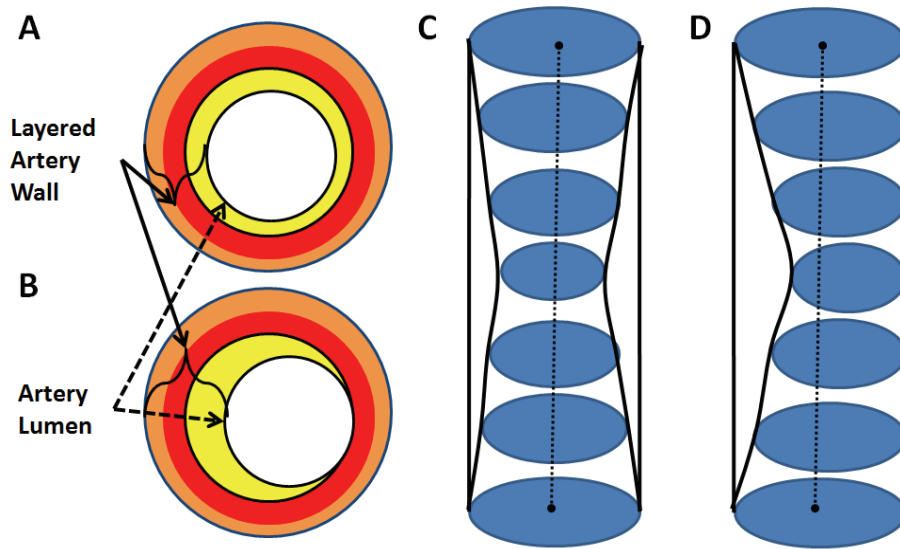


Figure 6.1: The symmetric and asymmetric stenosis plaque profiles introduced in the realistic aorta model R2.

The computational simulations with the stenosis in the branch entry regions and aortic arch were expected to give significant outcomes. The distribution of flow, pressure, and WSS are expected to affect significantly. In the following three subsections, the distribution of velocity, pressure, and WSS are discussed at the early and peak systole time instances.

6.2 Distribution of WSS in Aorta with Symmetric Stenosis in Branches

To study the effect of stenosis on flow dynamics, artificial stenosis was introduced at the branch entry regions of the brachiocephalic artery, common carotid artery, left subclavian artery and, aortic arch. The distributions of WSS in the cases with artificial stenosis are compared with the healthy case. The results of the healthy case have been discussed in the previous chapter. To study the effect of stenosis severity, stenosis with 50% and 80% blockage were introduced in each branch. To investigate the local variation in WSS at the neck of the stenosis, peripheral WSS at five time instances during a cardiac cycle were captured.

Figures 6.2 and 6.3 show the distribution of WSS in the upper aortic arch and branched under the influence of 50% symmetric plaque at the early systole and peak systole, respectively. As earlier demonstrated in Figure 5.8, the WSS at the branch entry region remained low relative to the maximum WSS observed in the healthy case. The maximum WSS during the peak systole at the branch entry region of the brachiocephalic artery, left carotid artery, and left subclavian artery is 3.3 Pa, 7.2 Pa, and 6 Pa, respectively. Shown in Figure 6.2, the WSS distributions captured during the early systole are significantly different from that in the aorta under the healthy case. The WSS magnitude in the upper aortic arch and distal aortic arch are higher than that observed in the healthy case.

The distributions of WSS in cases with symmetric plaque are significantly different even during the peak systole. The local distribution of WSS in the distal aortic arch, descending aorta, and upper aortic arch are substantially affected by the presence of stenosis in the branches. The maximum WSS at the branching region and descending aorta is distinctly visible in WSS distributions presented in Figure 6.3. Minor modifications in the WSS distributions are also observed in the inner aortic arch. In the case where the brachiocephalic artery is under 50% stenosis, the maximum WSS of 15.5 Pa is observed in the inner wall of the distal aortic arch. The distribution of WSS on the upper aortic arch region especially in the branch entry region major branches is modified significantly. At the branch entry region of both maximum and minimum WSS are more pronounced. The WSS distribution downstream of the stenosis (at bifurcation of right carotid and right subclavian) is significantly affected. In the case with 50% stenosis in the left carotid artery, maximum WSS at the inner wall of the distal aortic arch was observed to be 17 Pa, which is about 2 Pa higher than in the case with 50% stenosis in the brachiocephalic artery. Also, the WSS between the left carotid and left subclavian artery rises significantly. In this case, the WSS at the left

subclavian artery is also significantly affected. The distribution of WSS is most affected in the case with 50% stenosis in the left subclavian artery. The maximum WSS of the magnitude of 21 Pa is observed at the inner wall of the distal aortic arch and on the upper aortic arch (root of left subclavian artery).

In addition to the spatial WSS distributions, peripheral WSS at the neck of the stenosis was captured at 5 time instances during a cardiac cycle. The measurement of peripheral WSS begins from the proximal side running in anti-clockwise direction. For the sake of comparison, peripheral WSS at the location of artificial stenosis were also captured for healthy cases.

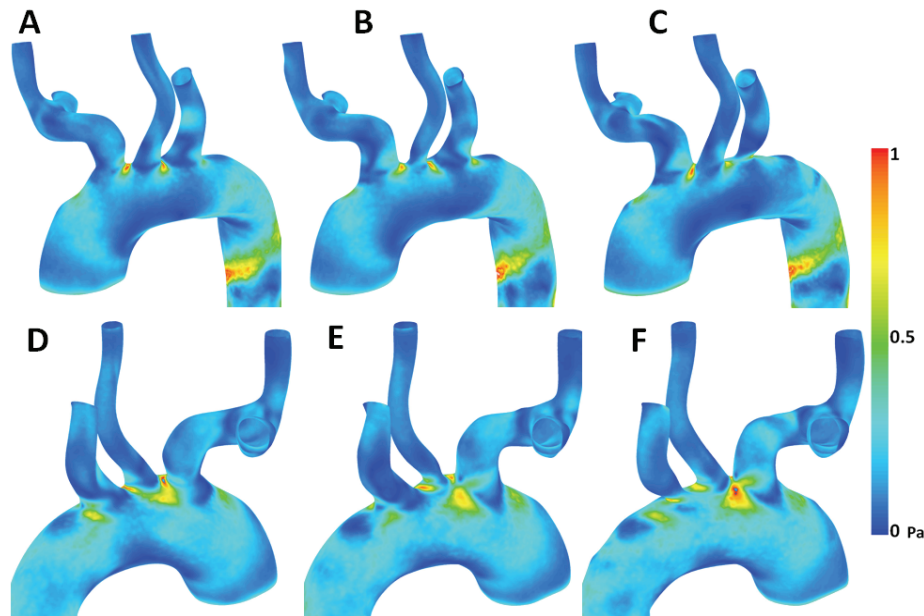


Figure 6.2: The anterior and posterior views of R2 with 50% symmetric plaque in (A, D) Brachiocephalic artery, (B, E) Left carotid artery, and (C, F) Left subclavian artery during early systole.

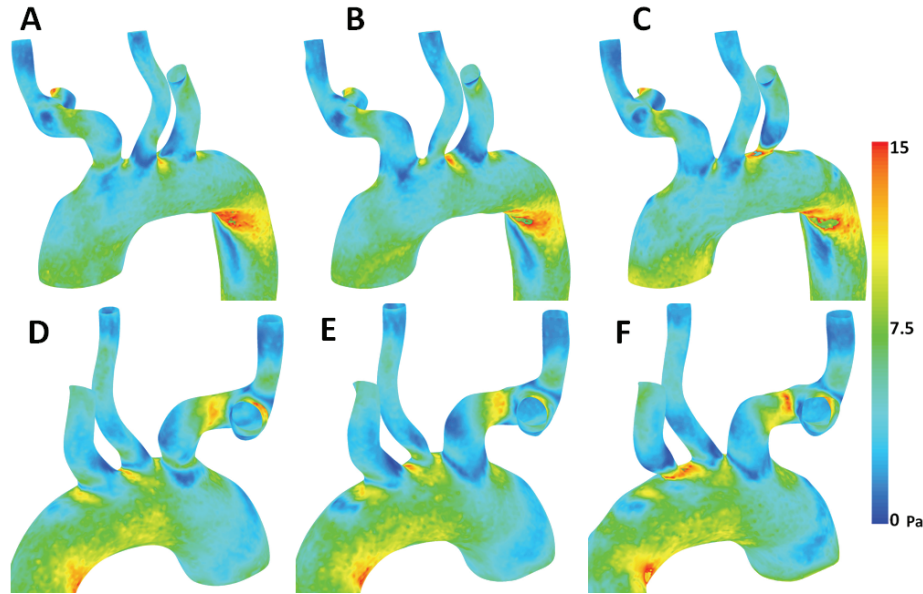


Figure 6.3: The anterior and posterior views of R2 with 50% symmetric plaque in (A, D) Brachiocephalic artery, (B, E) Left carotid artery, and (C, F) Left subclavian artery during peak systole.

Figure 6.4 and figure 6.5 show the distributions of peripheral WSS for healthy case and at the neck of the 50% stenosis respectively. The aim of the comparison is to study the extent of modification of the peripheral WSS at the location of the stenosis. During the early systole and flow reversal time, the magnitude of WSS remains low. Due to the accelerating flow, the WSS during the maximum acceleration remains low. The highest WSS is during the peak systole time. During the deceleration, the WSS distribution does not change qualitatively, although the WSS magnitude is lowered. Under the healthy condition, the WSS during the peak systole shows the maximum on the distal side and the minimum on the proximal side of the branch. Under the influence of 50% stenosis the WSS is amplified. In the brachiocephalic artery the maximum WSS during the peak systole is almost twice of the maximum WSS observed in the healthy case. However, in the left carotid artery, there are not many quantitative changes in the peripheral WSS distributions. The maximum WSS during the peak systole is 7 Pa in the healthy case, while in 50% stenosis case the maximum WSS is 8.8 Pa. In the left subclavian artery, the WSS distribution changes significantly, both quantitatively and qualitatively. The WSS distribution for the healthy subclavian artery shows skewness on the right side implicating the minimum WSS on the proximal side of the wall and the maximum on the distal side of the wall, while in

50% stenosis case the region of high WSS expands. Also the maximum shear stress in 50% stenosis in the subclavian artery during the peak systole is 15 Pa which is almost 3 times of that observed in the healthy case.

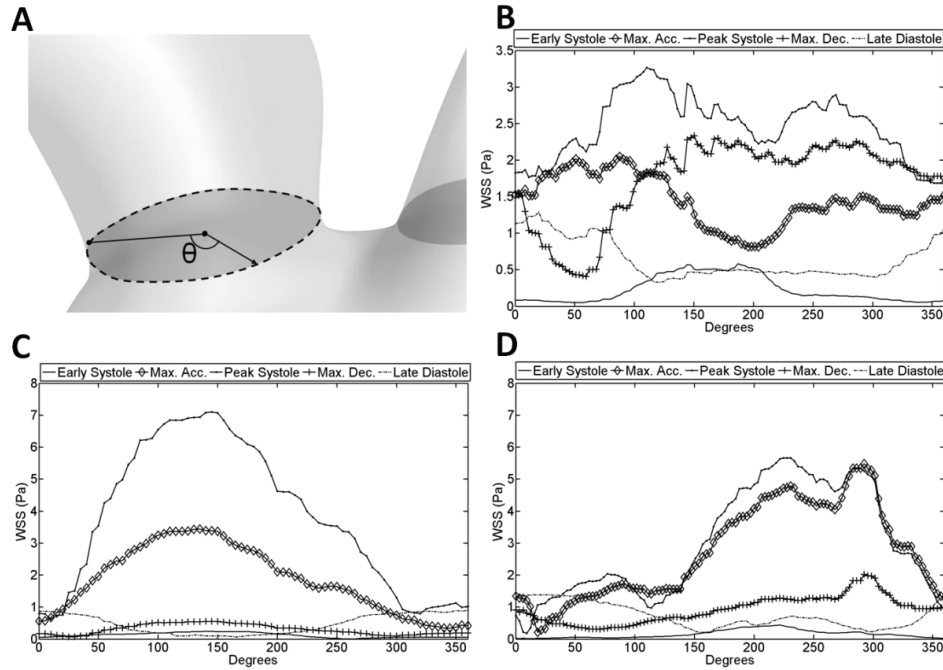


Figure 6.4: Peripheral WSS at the branch entry region neck of healthy aorta captured at 5 time instances during a cardiac cycle. (A) The measuring of WSS begins from side proximal to the ascending aorta. Peripheral WSS at the branch entrance region for healthy (B) brachiocephalic artery, (C) left carotid artery, and (D) left subclavian.

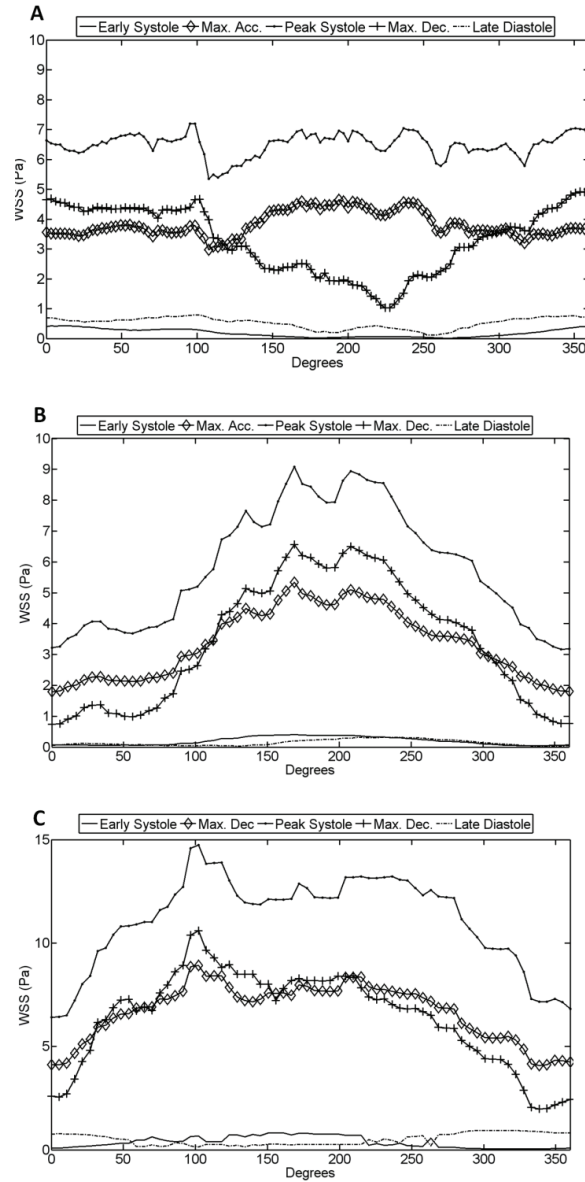


Figure 6.5: Peripheral WSS at the neck of the 50% symmetric stenosis captured at 5 time instances during a cardiac cycle. Peripheral WSS at the neck of the stenosis in (A) brachiocephalic artery, (B) left carotid artery, and (C) left subclavian under the influence of 50% symmetric plaque.

6.3 Distribution of WSS in Aorta with Asymmetric Stenosis in Branches

Figure 6.6 and Figure 6.7 show the distribution of WSS in aorta model R2 with asymmetric stenosis in three branches at the time instances of the early systole and peak systole respectively. The anterior view of the aorta model in Figure 6.7A shows that the maximum WSS of 23 Pa is distributed in the proximal side of the brachiocephalic artery. This is also shown in the Figure 6.8A where the peripheral WSS at the neck of the stenosis is presented as a graph. The WSS distributions during the accelerations and deceleration are qualitatively identical to that during the peak systole, and the maximum WSS remains localized even during the acceleration and deceleration phases. The peripheral WSS for the symmetric case as shown in Figure 6.5A is more uniform than the peripheral WSS for the asymmetric case, as shown in Figure 6.7A. The peripheral WSS for the asymmetric is higher on the proximal side and gradually decreases to the minimum on the distal side. The maximum WSS of 23 Pa in the asymmetric plaque in the brachiocephalic artery is 300% more than in the case where the symmetric stenosis was introduced in the brachiocephalic artery. The maximum WSS of 23 Pa is also significantly higher than mere 3.5 Pa in the healthy case. Thus, the peripheral WSS in the brachiocephalic artery is significantly affected by the asymmetric shape of plaque.

However, in the carotid artery, the distribution of peripheral WSS is identical with the low WSS distributed on the proximal side and high WSS distributed on the distal side. It is also noteworthy in Figures 6.5B and 6.7B that during the acceleration and deceleration, the distribution of WSS is identical to that during the peak systole. Also in the left carotid artery, the maximum WSS at the neck of the stenosis is 11 Pa which is mere 2 Pa higher than in the symmetric stenosis case, and the WSS in the asymmetric case is 4 Pa higher than in the healthy aorta case. The maximum WSS in the brachiocephalic artery and left carotid artery was higher in cases with asymmetric stenosis. However, in the left subclavian artery, the maximum WSS in the symmetric case was about 15 Pa which is about 300% higher than in the healthy case and 55% higher than in the case with asymmetric plaque in the left subclavian artery. The peripheral WSS distributions in symmetric and asymmetric cases are distinct. In the asymmetric case, the maximum WSS is more pronounced with almost a bell shaped distribution, while in the symmetric case the higher values are relatively uniform. In both cases the peripheral WSS distributions remain qualitatively same during acceleration, peak systole, and deceleration.

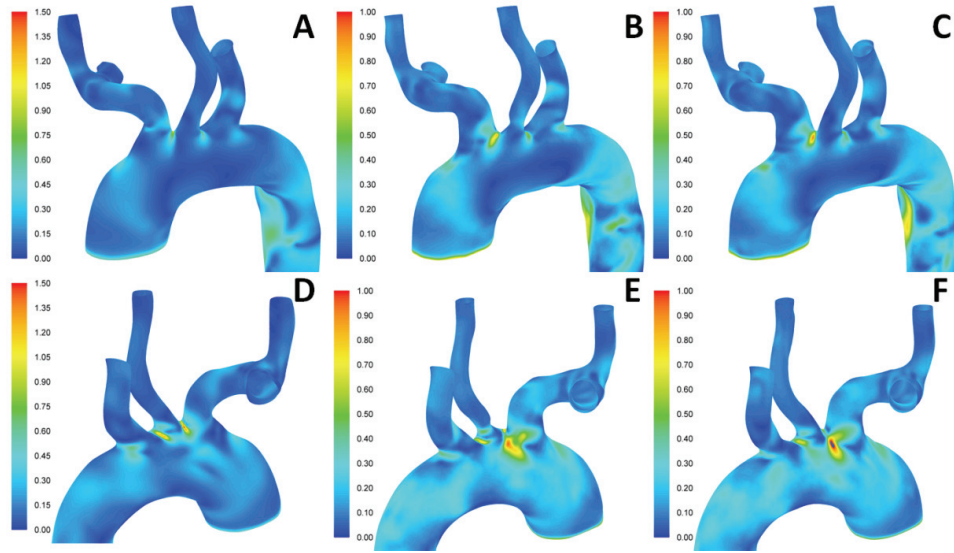


Figure 6.6: The anterior and posterior views of R2 with 50% asymmetric plaque in (A, D) Brachiocephalic artery, (B, E) Left carotid artery, and (C, F) Left subclavian artery during early systole.

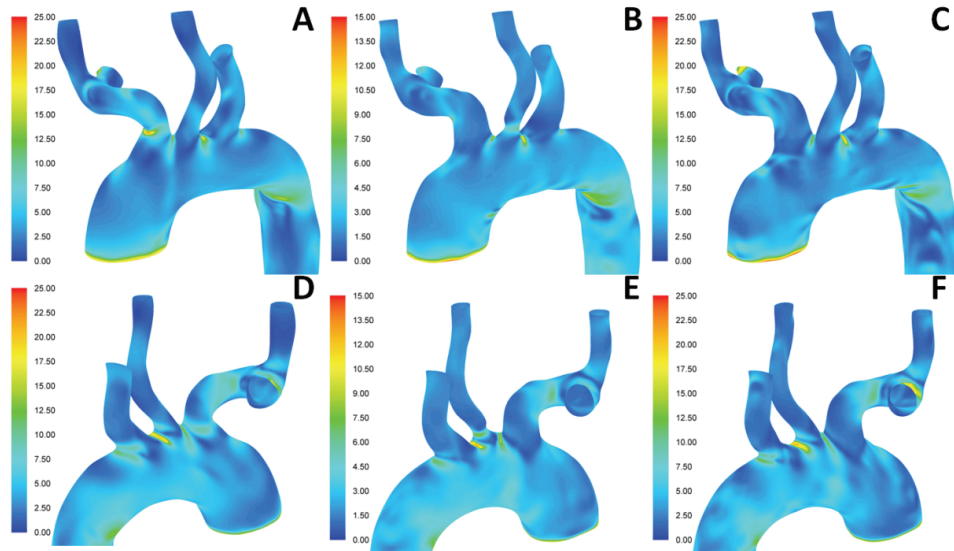


Figure 6.7: The anterior and posterior views of R2 with 50% asymmetric plaque in artery lumen blockage in (A, D) Brachiocephalic artery, (B, E) Left carotid artery, and (C, F) Left subclavian artery during peak systole.

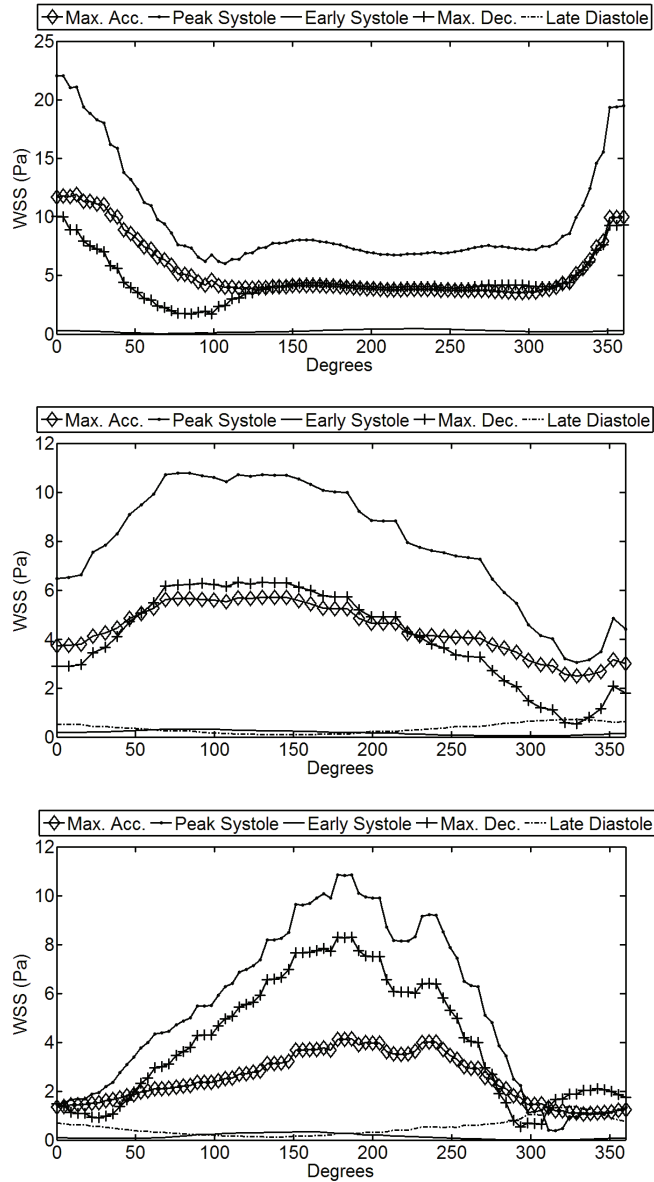


Figure 6.8: Peripheral WSS at the neck of stenosis captured at 5 time instances during a cardiac cycle. Peripheral WSS at the neck of the stenosis in (A) brachiocephalic artery, (B) left carotid artery, and (C) left subclavian under the influence of 50% asymmetric plaque.

6.4 Effect of Stenosis Severity on Distribution of WSS

To study the effect of stenosis severity, numerical simulations were performed in cases with stenosis plaques with 80% blockage at the branch entry region of three branches. Figure 6.9 and Figure 6.10 show the distribution of WSS and peripheral WSS at the neck of the stenosis for symmetric plaque in three branches respectively. Figure 6.11 and Figure 6.12 show the distribution of WSS and peripheral WSS at the neck of the stenosis for asymmetric plaque in three branches respectively. The WSS profiles for symmetric and asymmetric cases are compared directly. The section concludes with comments on the effect of the shape of plaque on the WSS.

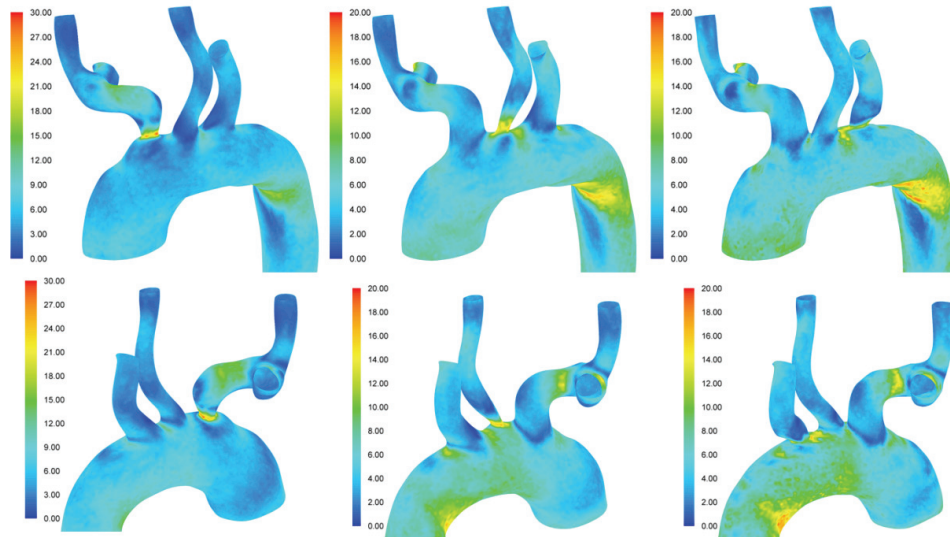


Figure 6.9: The anterior and posterior views of R2 showing the distributions of WSS in the numerical cases where symmetric atherosclerotic plaque is introduced at the branch entry region to cause 80% artery lumen blockage in (A, D) Brachiocephalic artery, (B, E) Left carotid artery, and (C, F) Left subclavian artery during peak systole.

The distributions of WSS for three arteries shown in Figure 6.9 are significantly different from the corresponding WSS for three arteries shown in Figure 6.3, especially in the stenosed region. For the brachiocephalic artery under the influence of 50% asymmetric plaque, the distribution of WSS at the stenosed region was relatively uniform without a clear maximum. This is demonstrated in Figure 6.5A. However, in the case with 80% stenosis in the brachiocephalic artery, the distribution is bell-shaped with higher WSS distributed on the distal

wall of the branch and low WSS distributed in the proximal side of the branch. Such a distribution is also followed by WSS distributions for the left carotid and left subclavian artery under the influence of 50% symmetric stenosis (see Figure 6.5B-C). For the left carotid artery under the influence of 80% symmetric stenosis, the distribution of peripheral WSS at the neck of the stenosis is more uniform. However, in both of the distributions, the maximum remains distributed in the distal side of the wall. The distribution of peripheral WSS for the left subclavian artery is substantially different in 50% and 80% cases (Figures 6.5C and 6.10C). The peripheral WSS for 80% case is a bimodal distribution with a major peak at the distal side of the wall and a minor peak at the posterior side of the wall.

The maximum WSS of 25 Pa is observed at the neck of stenosis in the brachiocephalic artery, which is significantly higher than that in the healthy and 50% stenosis case. The magnitude of maximum WSS in the left carotid and left subclavian artery is 16.2 Pa and 17.5 Pa, respectively. The magnitude of maximum WSS in the left carotid is 80% higher than that in 50% stenosis case, while the same for the subclavian artery is mere 17% higher than that in 50% stenosis case. It is of notice that in the brachiocephalic artery and the left carotid artery, the magnitude of maximum WSS at the neck of stenosis rises exponentially with the severity of stenosis.

Referring to Figures 6.7A and 6.11A, the WSS distributions are identical in the cases with 50% and 80% asymmetric stenosis. In both of the cases, the maximum WSS is localized on the proximal side of the branch, while a relatively lower WSS is distributed on the distal side of the branch. As a result of this, the graphs for the peripheral WSS distributions shown in Figures 6.8A and 6.12A follow the bell-shaped distribution. The comparison of peripheral WSS also reveals a clear difference between the scales of the distributions. While in 50% stenosis case the magnitude of maximum WSS is about 23 Pa, the magnitude of maximum WSS in 80% stenosis case is 49 Pa. Such a difference of scales is also noticed while comparing WSS distributions for the left carotid artery under the influence of 50% stenosis (Figure 6.7B) and 50% stenosis (Figure 6.11B).

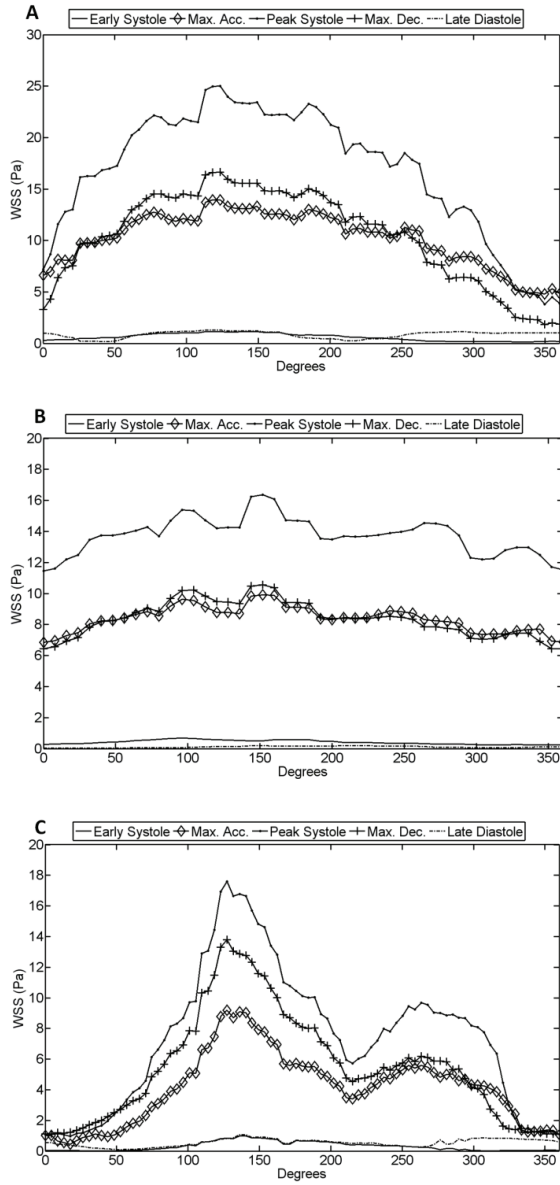


Figure 6.10: Peripheral WSS at the neck of stenosis captured at 5 time instances during a cardiac cycle. Peripheral WSS at the neck of the stenosis in (A) brachiocephalic artery, (B) left carotid artery, and (C) left subclavian under the influence of 80% symmetric plaque.

Under the influence of 50% asymmetric plaque, the distribution of peripheral WSS again follows a bell-shaped distribution with a maximum of 9 Pa, while under the influence of 80% asymmetric plaque, the distribution of peripheral WSS is relatively uniform with a maximum of 16.2 Pa. Although the distribution of peripheral WSS is bell-shaped, there are more than one maximum points distributed between 75 and 125. The severity of stenosis causes local variation in the maximum WSS as well. In 50% case maximum WSS of 11 Pa is localized in the anterior side, while in the 80% case the maximum WSS migrates towards the posterior-distal side of the wall.

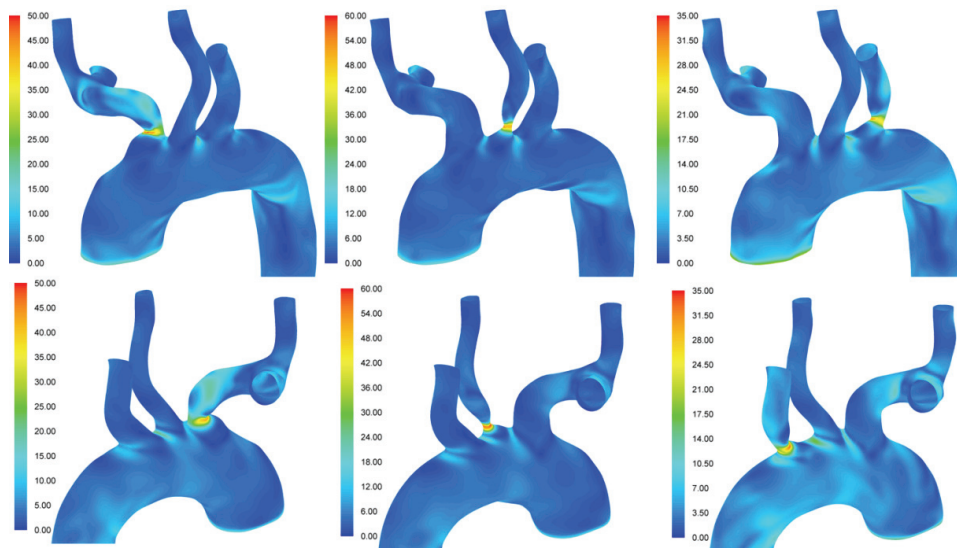


Figure 6.11: The anterior and posterior views of R2 showing the distributions of WSS in the aorta model R2 with asymmetric atherosclerotic plaque in (A, D) Brachiocephalic artery, (B, E) Left carotid artery, and (C, F) Left subclavian artery during peak systole.

For 50% asymmetric stenosis case, the distribution of WSS at the neck of the left subclavian artery also follows a bell-shaped distribution with higher WSS localized on the distal side of the wall (Figure 6.11-6.12). However, under the influence of 80% stenosis, the distribution of WSS is bimodal with a global maximum localized in the proximal side of the wall and a local maximum localized on the distal side of the wall. It is also of notice that the global maximum of 32 Pa in 80% asymmetric stenosis case is about 191% higher than that in 50% asymmetric stenosis case. The maximum WSS is localized in the proximal side of the branch, which coincides with the location of asymmetric plaque. This is in contradiction to the 80% asymmetric plaque in the left carotid artery where the maximum WSS is localized on the distal side of the branch.

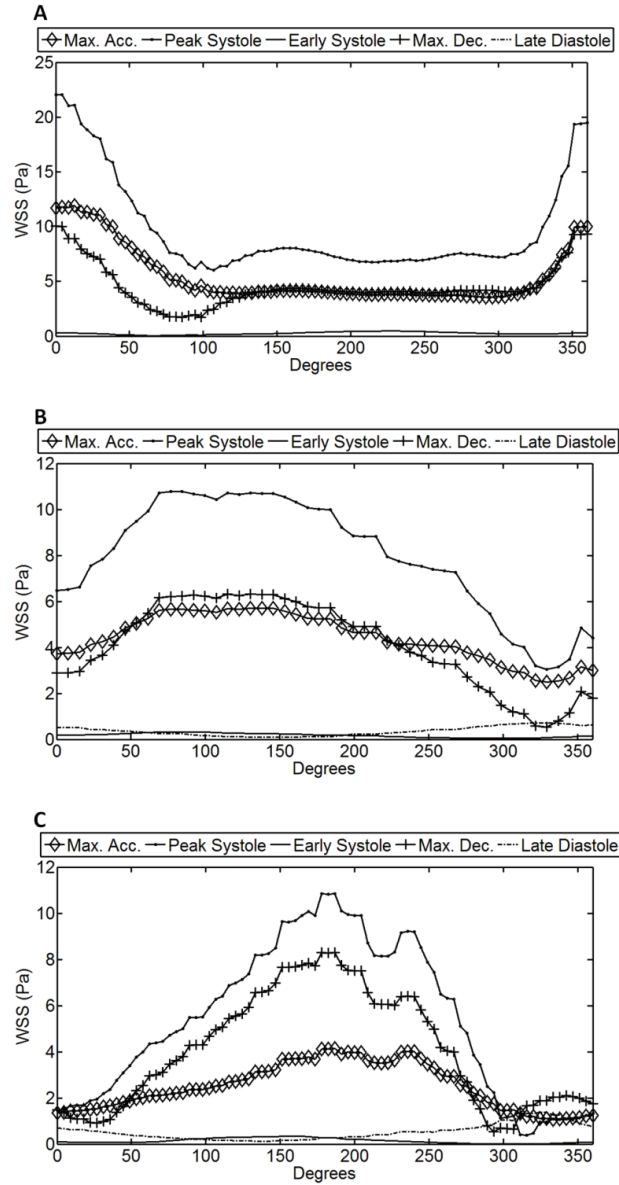


Figure 6.12: Peripheral WSS at the neck of stenosis captured at 5 time instances during a cardiac cycle. Peripheral WSS at the neck of the stenosis in (A) brachiocephalic artery, (B) left carotid artery, and (C) left subclavian under the influence of 80% asymmetric plaque.

It is now known that the severity of atherosclerotic plaque can alter WSS distributions in the vicinity of stenosis and globally. To test the extent of elevation of WSS at the neck of stenosis, a simulation case with 98% asymmetric stenosis in the brachiocephalic artery was performed. The effect of severity of asymmetric stenosis on the maximum WSS at the neck of the stenosis is presented in Figure 6.13. The graph demonstrates the exponential growth in the maximum WSS with stenosis severity. The maximum shear stress for 50% severity is 49 Pa, while for 98% stenosis the same is 781 Pa. The exponential growth in the shear rate with stenosis severity has also been demonstrated by Bark and Ku (2010), where numerical experiments have been conducted in idealized arteries with an extreme stenosis degree with stenosis blockage ranging from 75% to 99%. Under several sets of boundary conditions the shear rate followed identical exponential growth with the severity of stenosis. The numerical experiments also demonstrated that under higher degree of stenosis (75% to 95%), the growth in the shear rate is almost linear.

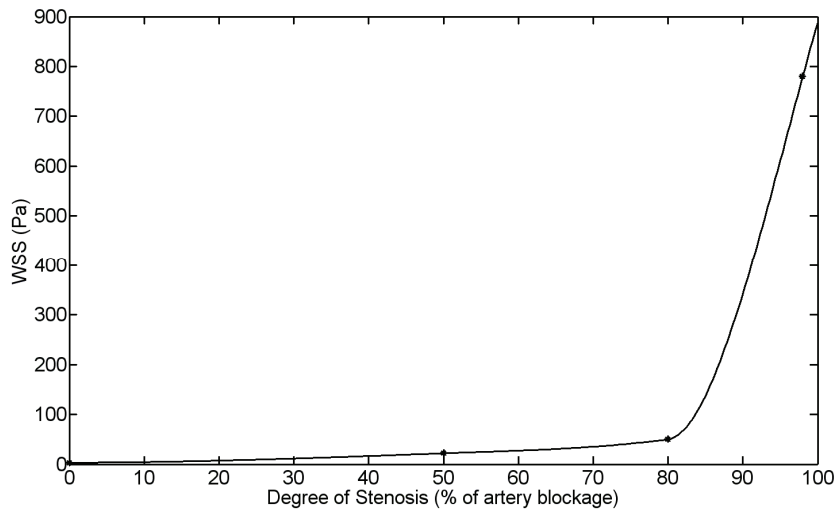


Figure 6.13: Graph of degree of the stenosis versus WSS. The WSS is the maximum WSS observed during a cardiac cycle.

6.5 Distribution of WSS in Aorta Model with Stenosis in Aortic Arch

Aortic arch is one of the preferential locations for the localization of atherosclerosis. The behavior of flow undergoes severe modifications due to the stenosis in the aortic arch (Huang et al (2010)). To investigate the effect of stenosis in the aortic arch on the distribution of WSS, the aorta model R2 was altered. Artificial stenosis of 50% and 80% severity was introduced at the inner curvature of the aortic arch. The distribution of WSS in the upper aortic arch and peripheral WSS at the neck of the stenosis are discussed briefly in this section.

Figure 6.14 shows the distribution of WSS in the upper aortic arch under the healthy condition, 50% stenosis severity, and 80% severity. The anterior and posterior views show high WSS distributed between the branching arteries and inner curvature of distal aortic arch. In 80% severity case, high WSS is also at the inner aortic arch. The view from the below the aortic arch shows high WSS also distributed at the inner wall of the aortic arch. It is of notice that in the aorta model with the healthy aortic arch the magnitude of WSS at the inner aortic arch is low. In the aorta models with 50% and 80% stenosis in the aortic arch the maximum WSS is 20.1 Pa and 33.8 Pa respectively. Thus, with the increasing degree of stenosis the WSS escalates.

For further investigation, peripheral WSS was captured at the neck of the stenosis at five time instances during a cardiac cycle. For the sake of comparison, peripheral WSS at the same axial section was captured for the healthy aortic arch case, too. Figure 6.15 shows the peripheral WSS in all three cases: healthy, 50% stenosis, and 80% stenosis. The distributions show that during a cardiac cycle high WSS remains distributed in the upper aortic arch and low WSS distributed at the inner curvature of aortic arch. This is in contradiction to the observations made in cases with stenosis at the branch entry region. In the case with stenosis in the branches, the WSS at the neck of stenosis remained maximum, which lowered down in the broadening regions pre and post stenosis. Contrary to this, in the cases with stenosis in the arch low, WSS was distributed at the neck of stenosis while high WSS is distributed in pre and post stenosis regions.

The pathlines colored with velocity magnitude show flow stagnation in the region past stenosis. The recirculation of flow in prior and post stenosis region causes large WSS. The accelerated flow in the upper aortic arch also causes accelerated flow in the branches. The flow separation in the branches causes flow stagnation towards the proximal wall of the branches. The flow stagnation in the branches

causes higher WSS distributed at the branch entry region of the brachiocephalic artery, left carotid artery, and the left subclavian artery. The regions with higher WSS correspond to the areas that are vulnerable to aortic dissection and dissecting aneurysms (Huang et al. (2010)).

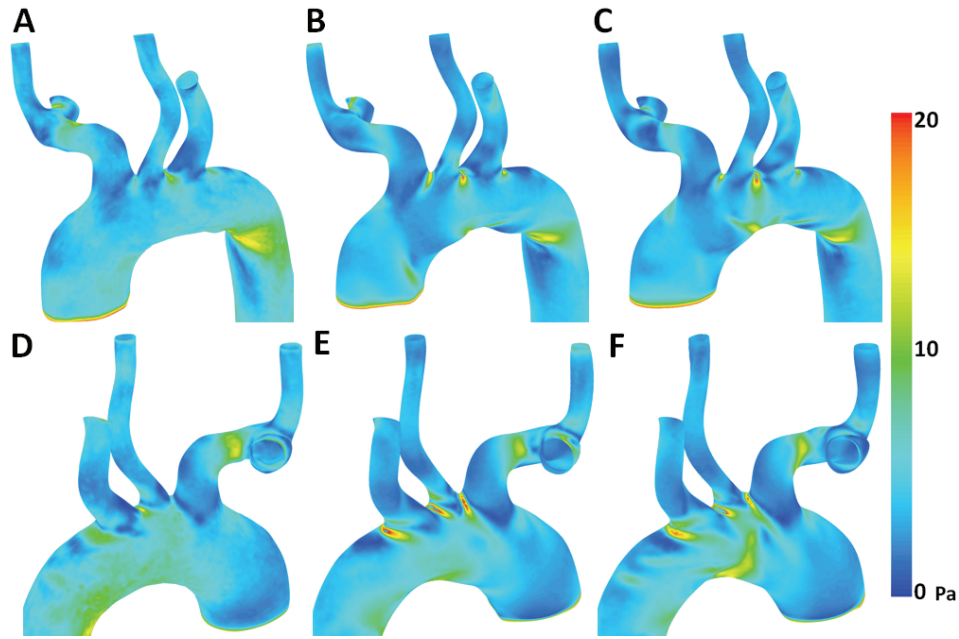


Figure 6.14: The anterior and posterior views of the aortic arch models showing the distributions of WSS for the (A, D) healthy case, (B, E) aortic arch with 50% stenosis, and (C, F) aortic arch case with 80% stenosis.

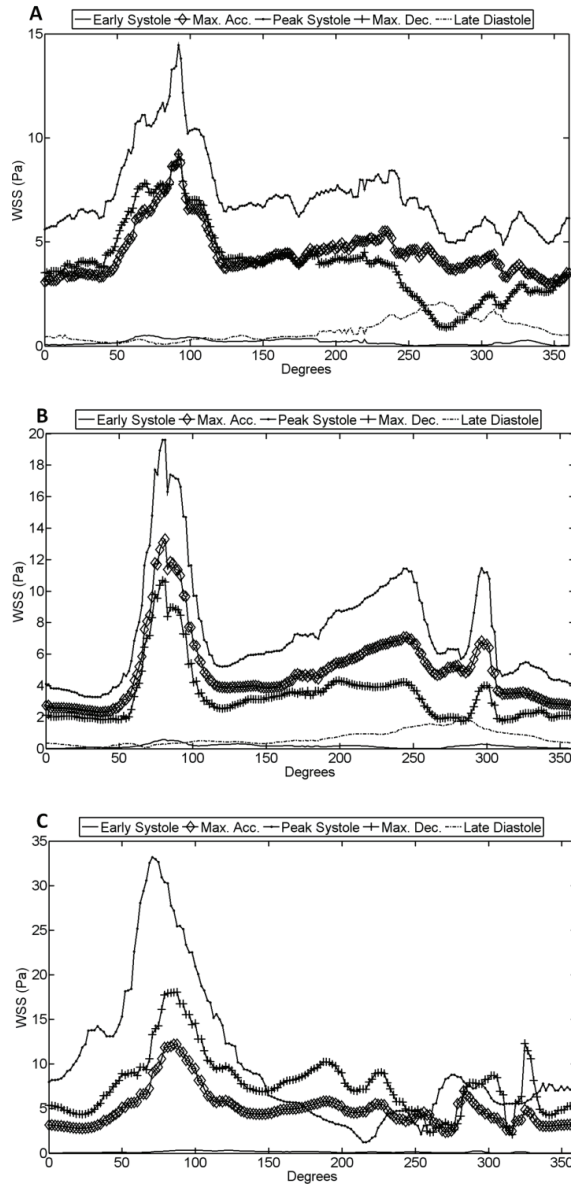


Figure 6.15: Peripheral WSS captured at 5 time instances during a cardiac cycle at the axial section at the neck of stenosis introduced in the aortic arch under (A) Healthy condition, (B) 50% stenosis plaque, and (C) 80% stenosis plaque.

6.6 Discussion

The flow dynamics in an artery with stenosis is characterized by altered WSS distribution at the stenosed region and flow stagnation past stenosis region. The recirculation of the flow may vary during the cardiac cycle. The results from blood flow simulations in the aorta with stenosis at the branch entry region and the inner aortic arch are reported in this chapter. Asymmetric and symmetric types of atherosclerosis plaque were introduced at the branch entry region of each branch, while stenosis of 50% and 80% severity was introduced at the inner wall of the aortic arch.

The distributions of WSS for symmetric atherosclerotic plaque are shown in Figures 6.3 and 6.5. The results suggest that during a cardiac cycle, the magnitude of maximum WSS at the neck of the stenosis for the brachiocephalic artery, left carotid artery, and left subclavian artery is 7 Pa, 9.2 Pa, and 14.8 Pa, respectively. These values are about 98%, 23%, and 62% higher than the corresponding WSS magnitude in the normal case (shown in Figure 6.4). The comparisons of WSS distributions in the healthy aorta and the aorta with stenosed arteries also showed significant modifications in WSS magnitudes in other sites as well. In the healthy aorta, high WSS was distributed between the junctions of two branches, distal curvature of aortic arch. In cases with stenosis in the branches, the values of high WSS further increased. The maximum WSS at the distal aortic arch is 15 Pa in the normal case while the same is 17 Pa in the case with stenosis in the brachiocephalic artery, 18.5 Pa in the case with stenosis in the left carotid artery, and 21 Pa in the case with stenosis in the left subclavian artery.

The distributions of WSS for asymmetric atherosclerotic plaque shown in Figures 6.6 to 6.8 suggest that during a cardiac cycle, the magnitude of maximum WSS at the neck of the stenosis for brachiocephalic artery, left carotid artery, and left subclavian artery is 22 Pa, 10.4 Pa, and 11 Pa, respectively. The results for the asymmetric atherosclerotic plaque are significantly different than in the normal case and cases with symmetric atherosclerotic plaque. The cases with asymmetric plaque showed higher and more localized WSS at the stenosis. The altered and elevated WSS at the neck of the stenosis can be associated with the risk of the rupturing of atherosclerotic plaque.

The inner aortic arch has been classified as one of the vulnerable sites for the localization for atherosclerosis. In their works, Gao et al. (2006), Huang et al. (2010), and Shahcheraghi et al. (2002) have demonstrated the flow separation at the inner curvature of aortic arch. In Chapters 4 and 5 the results obtained with numerical experiments with idealized and realistic models of the human aorta have demonstrated that the curvature of the aortic arch induces flow separation

and secondary flow motion. In the experiments with both types of aorta models, low WSS was distributed at the inner aortic arch and high WSS distributed at the inner wall of the distal aortic arch. Besides the risk of the rupturing of plaque, the LDL transports through the arterial wall can vary in arteries with asymmetric and symmetric stenosis (Vancia et al. (2006)).

Huang et al. (2010) conducted experiments with idealized models of aortic arch with and without stenosis. It was demonstrated that even minor stenosis in aortic arch significantly alters flow and WSS distribution. However, the model used by Huang et al. (2010) is idealized, and such a state of the aorta may not occur in real life. Adopting the idea of atherosclerosis in the aortic arch, the realistic aorta model R2 was altered to introduce arterial stenosis in the inner aortic arch. The artificial stenosis of 50% and 80% was introduced by manipulating the contours obtained with the image processing of CT images. The stenosis caused significant modifications in the flow and WSS distributions. The results demonstrated accelerated flow at the location of stenosis. Flow stagnation was observed at pre and post stenosis regions. The stenosis also caused flow stagnation at the branch entry region of three major branches. The locations of flow stagnation correspond to the regions with elevated WSS values. The higher and lower WSS upstream and downstream of the stenosed region may increase the risk of atherosclerosis localization and even aortic dissection.

The exponential growth in the maximum shear stress has been demonstrated in Figure 6.13, where the maximum WSS for 98% stenosis case is 781 Pa. Such a high force is a result of abruptly varying flow at the stenosed region and in the vicinity of the stenosed region. It has also been demonstrated that even a minor stenosis can cause significant alteration in the flow in the other sites of the aorta as well. The highly altered and abrupt flow and WSS distribution can cause the rupturing of plaque and artery occlusion. The region with extremely high shear stress is also associated with platelet adherence (Bark and Ku (2010)).

The blood flow through the stenosed arteries has been studied previously (Bark and Ku (2010), Prahlad (2004), Mustapha (2010), Valencia(2006)). However, these studies were based on idealized models of arteries. The presented work is an attempt to extend the idea with realistic artery models. The numerical investigations such as the ones presented in this chapter can help understand modification in the cases of human aorta with minor to extreme stenosis. The modification in WSS and increase in oscillation of WSS would implicate the risk of atherosclerosis and dissection in locations other than the stenosed region. Such studies can provide better understanding of flow dynamics in diseased arteries.

7 Conclusions and Discussion

Cardiovascular diseases account for the highest number of deaths in global population today. Ischemic heart and artery diseases are the major cardiovascular diseases. The ischemic arterial diseases are characterized by building up of fat and cholesterol deposits, often referred to as atherosclerotic plaque, within artery walls. Overtime the plaque within artery wall can grow larger, eventually narrowing artery lumen. The narrowing artery lumen can cause irregular supply of blood, oxygen, and vital nutrient. The irregular supply of blood and vital nutrients can also cause dysfunction of vital organs, such as heart, brain, and kidneys.

The atherosclerotic plaques are often observed in large and medium sized arteries, such as aorta and the branching arteries of aorta. Numerous studies on blood flow dynamics have demonstrated the complex distribution of flow and WSS in large and medium sized arteries. Most large and medium arteries are known to have a complex anatomy including curvature, branching, and distal narrowing of lumen area. In addition to complex anatomy, larger arteries are thick-walled with abundant elastin. The larger lumen area and elastic artery wall allows them to serve as low-resistant conduits. The large arteries expand and contract to maintain regular supply of blood flow to branching arteries and protect small arteries from being exposed to high blood pressure. The abundance of elastin also helps large arteries withstand high and fluctuating blood pressure. The elastic nature of artery wall can influence the distribution of flow and local WSS. Since the blood flow in the arteries is driven by artery anatomy, the blood flow in large and elastic arteries can be complex with extremely high and low WSS localized in certain regions. Earlier in vivo and experimental works have shown that atherosclerotic plaque is localized in the regions with low and oscillating WSS.

Human aorta is known to have the most complex anatomy with branching, tapering of lumen, curvature in aortic arch, and highly elastic wall. In the presented work, blood flow in idealized and realistic models of thoracic aorta was simulated. The distribution of flow, pressure, and WSS was investigated to understand the risk of localisation of atherosclerosis in the aortic arch and in the vicinity of major branches. The reported work was conducted in three parts.

1. In the first part, idealised models of thoracic aorta were constructed and blood flow was simulated using a FEM based computer code Comsol Multiyphysics V3.4. Three aorta models were constructed based on the measurements from the literature. The flow, pressure, and WSS distributions were studied and compared to study the role of artery anatomy on the flow dynamics. The study is further extended to understand the effect of pressure on the flow dynamics. This study helps to

obtain an estimate of flow dynamics in the real aorta. The comparison of the flow dynamics in three aorta models has been reported (Vasava et al. 2009a, Vasava et al. 2009 b). The effect of pressure on flow dynamics in the aorta has been also reported (Vasava et al. 2009, Vasava et al. 2011).

2. In the second part of the study, a realistic model of aorta was used instead of the idealized ones. Two sets of CT images were processed with medical image processing code to obtain a 3D model of thoracic aorta. The 3D model was treated with CAD programs to make the aorta model compatible for the pre-processing code to generate computational domain and mesh grid. FVM based computation code Fluent V12 and V13 were used to simulate blood flow within the realistic models of aorta. Two aorta models were used to study the role of artery anatomy on the flow.
3. Based on the results from realistic aorta models, the study was further extended to investigate flow dynamics within aorta with stenosis in branches and aortic arch. Artificial stenosis of 50% and 80% severity was introduced in the vicinity of branches and inner wall of aortic arch. The aim of these experiments was to study the extent of flow modification due to the stenosis and the risk of atherosclerosis and wall dilation in other locations of aorta.

The results from the idealized aorta models showed that the flow dynamics in aorta is significantly affected by artery anatomy and pressure. In the aorta model with smaller ratio of lumen and radius the bifurcation at branches dominated the flow in the aortic arch. In the same model, the flow in the ascending aorta was parabolic-like with a maximum velocity in the centre of the trunk. In the aorta model with a larger radius of curvature of aortic arch, the flow in the ascending aorta and proximal aortic arch remained skewed towards the outer and inner walls respectively. Despite several differences in flow and WSS distributions in the aorta models, the sites for flow stagnation, high and low WSS distribution remained the same in the aorta models. The flow separation occurred at the inner curvature of aortic arch, while high WSS distributed in the distal side of the branch entry region and inner wall of the distal aortic arch. The deformation of the aortic arch and branches under hypertension and its influence on the flow dynamics are investigated by comparison of the velocity and WSS profile under hypotension, normal pressure, and hypertension conditions. The distribution of flow amplified with the rise in pressure. Moreover, the mass flow rate at the outlet of branches increased with the rise in pressure. The comparisons of WSS distributions, peripheral WSS and axial flow distributions showed that the shear stress and other fluid mechanical characteristics deviate from their normal spatial and temporal distributions. The complex changes in the hemodynamic forces

locally lead to circumstances associated with the high risk of arterial wall diseases. This in turn highlights the role of hypertension in the localization of atherosclerosis.

The idealized models of thoracic aorta helped in obtaining an estimate of real flow dynamics in the aorta, although the idealization of thoracic aorta models and assumption of rigid walls caused several unreal flow features in the aorta models. For example, the real aorta has blunt and curved junction at the branch bifurcations. However, due to the lack of exact measurements such geometric feature could not be incorporated in the aorta models used in the presented study. The sharp edges at the junction caused flow acceleration which may not occur in the real aorta. Also, the assumptions of uniform area of cross-section along the length of aorta and the planar nature of aorta trunk caused the flow and WSS distributions to be symmetric. While the comparison of flow dynamics within the realistic and idealized aorta models are qualitatively conclusive, it is strongly recommended, therefore to use the image based aorta models which include the actual anatomy of thoracic aorta. In order to overcome the limitations offered by the idealized aorta models, realistic aorta models were constructed based on CT images.

Two realistic models of thoracic aorta were constructed from CT images using medical and CAD computer codes. The analysis of flow dynamics revealed highly complex and non-uniform distribution of flow and WSS. The distributions of flow, pressure, and WSS in the realistic models were significantly different from those in the idealized models. The details of differences are discussed in the last section of Chapter 5. Although studying the effect of artery anatomy with mere two aorta models would be beyond the scope of the work, the flow, pressure, and WSS distribution of two aorta models were compared. The primary flow distributions in R1 and R2 were qualitatively identical. The primary flow, axial flow distributions were compared at 5 time instances in a cardiac cycle. The detailed comparisons are presented in Chapter 5. From the comparisons of flow dynamics in realistic and idealized models it could be concluded that the use of realistic aorta models can yield more realistic and reliable results. The simplification of aorta models can result into incorrect inference, e.g. localization of atherosclerosis, transport of LDL or oxygen through the aorta wall. Thus, the use of realistic models of arteries to obtain accurate and reliable results is emphasized. The use of two aorta models allowed the comparison of flow dynamics in the patient specific aorta models. The comparison revealed that the behavior of the blood flow and the distribution of the shear forces heavily depend on the local anatomy of arteries. The earlier studies have established that atherosclerosis is prone to develop in site in the arteries with low and fluctuating WSS. The atherosclerosis is known to localize in the vicinity of branching and

curvature. In the present work, the sites in the vicinity of branching arteries, inner wall of aortic arch and inner wall of distal aortic arch were observed to have localized low and fluctuating WSS.

Based on the distributions of WSS in the realistic aorta models, artificial stenosis was introduced in the vicinity of branching and inner wall of the aortic arch. With the aim of studying the flow dynamics in the arteries with stenosis, the aorta model R2 was altered to introduce artificial stenosis in the vicinity of branching and inner wall of the aortic arch. The details of modification in the aorta model R2 are presented in Chapter 6. The results in Chapter 6 demonstrated significant differences in WSS distribution in cases with asymmetric and symmetric plaque. Higher and more localized WSS was observed in the branches with asymmetric plaque. The study also revealed that the magnitude of WSS at the neck of the stenosis rises with the severity of stenosis. This can be linked with the rupturing of atherosclerotic plaque. The cases with atherosclerotic plaque demonstrated that even minor stenosis in the aortic arch can alter the flow and WSS distributions significantly. The WSS at the neck of the stenosis was low which is in contradiction to the cases with stenosis in the branches. The stenosis in the aortic arch caused flow stagnation in the regions before and after stenosis. The flow stagnation caused extremely high WSS in the pre and post stenosis regions. The elevated WSS can be linked with plaque rupturing. It can thus be concluded that the risk of plaque rupturing increases in cases with higher degree of stenosis. The presence of stenosis plaque also causes significant modification in other sites of aorta, which may increase the vulnerability of localization of atherosclerosis in multiple locations in the aorta. The distribution of higher and lower WSS upstream and downstream of the stenosed region may increase the risk of atherosclerosis localization and even aortic dissection.

The assumptions of a rigid artery wall and neglecting mass transport through the artery wall are a measure of the simplification of the current work. The aorta is thick-walled and elastic. The thickness of the aorta wall varies along the length of the aorta. During the systole part of a cardiac cycle, a large amount of blood is pumped from the left ventricle of heart to the aorta. The ascending aorta walls expand to accumulate the large amount of blood pumped by the left ventricle of heart. To simulate such a complex phenomena we require a special computational code that offers to solve fluid flow as well as structural deformation. Since the computational code used during the course of the work did not offer such calculations, the aorta walls were assumed to be rigid. However, that limitation will be resolved in our future works to achieve more precise results. The details of the work in progress are briefly described in the last chapter of the thesis. Currently work is in progress to overcome these simplifications. The following

chapter contains a brief description of undergoing works and suggestions for future work.

8 Future Work and Suggestions

The reported work began with simulating blood flow in idealized aorta models. The idealized models offered a robust estimate of flow dynamics of blood flow. The limitations offered by idealized aorta models could be overcome by the use of CT image based aorta models. The results from realistic models were more reliable and helped predict blood flow dynamics accurately. In this section, several future work suggestions are listed.

Effect of Non-Newtonian Properties of Blood: Currently the group is focused on carrying out numerical experiments to study the effects of non-Newtonian properties of blood on flow dynamics. Twelve non-Newtonian models of blood are tested to investigate the effects on material properties on behaviour of flow, distributions of WSS and OSI.

Effect of Artery reconstruction algorithms and CT image resolution on Blood Flow Dynamics: During the course of the work two algorithms were used to reproduce realistic models of the human aorta. The models obtained from both the algorithms are being tested to study the effect of CT images resolution, slice thickness and the algorithm parameters on the final model and thus the flow dynamics.

Fluid structure interactions: The assumption of rigid artery wall and the absence of mass transport through artery wall remain. The aorta is an artery with thick wall and elastic wall. The distensible artery wall significantly altered flow and WSS distribution. Figure 8.1 shows the distribution of flow in simplified artery. Notice the altered flow direction close to artery wall, which would not exist in the simulation with rigid wall. Currently the reported work is being extended to include flexible artery wall and analyze with the flow dynamics with flexible artery wall via flow simulations with fluid-structure interactions.

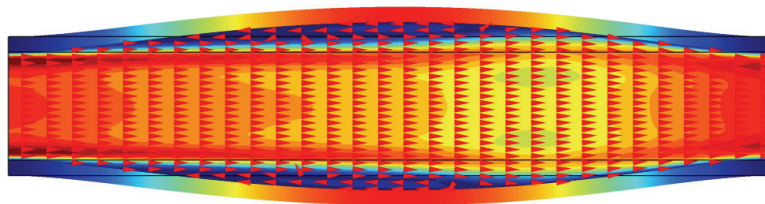


Figure 8.1: Wall displacement and flow field in an idealized artery.

Mass transport through artery wall: The atherosclerosis is triggered with complex flow dynamics. The passage of material such as macrophages and LDL

stimulates the formation of plaque within artery walls. The mass flow of such species transport through arterial wall could be coupled with blood flow in thoracic aorta. Such a study can help understand the effects of blood flow on species transport.

Inlet boundary conditions: The aorta is attached to the left ventricle of heart with aortic valve between the two. The opening and closing of aortic valve induces significant disturbance in the flow. In the current work, a flat velocity profile was used as an inlet boundary condition. The boundary conditions may need to be revised in order to include the effect of aortic valve in the inlet flow profile.

Outlet boundary conditions: In blood flow simulations the boundary conditions applied at the outlet have been subject to arguments. Pressure, target mass flow, and outflow are the most commonly used boundary conditions. The boundary conditions for blood flow simulations can vary according to the interaction between the artery and the connected organs. Some recent works have used Windkessel approach to determine the flow dynamics at the outlet. In reality, the outlet boundary condition may depend on several factors, such as the health of the patient, distal bed resistance, oxygen requirement of corresponding organ etc. Thus, to apply accurate outflow conditions specifically *in vivo* measurements must be applied.

The boundary conditions can be determined or corrected by additionally simulating the blood flow in full scale arterial tree model which includes the branching of large artery into medium and micro scale arterioles. Another way to calculate vascular resistance is to assume that the part of the branching artery at the branch outlet is a porous medium. Although, such an experiment could not be performed during the reported study, this can serve as a fundamental idea for a future research.

Gender based risk of arterial disease: In the current study only two realistic aorta models were used for simulating the blood flow. With such few models it is not possible to determine whether the atherosclerosis is more vulnerable in male or female patients. An extensive analysis of blood flow in a greater number of cases can allow the assessing of a gender based risk of arterial diseases.

Arteries with multiple stenoses: The aorta model R2 used in the present study was modified to mimic the aorta with stenosed branches and aortic arch. In the presented work only cases with stenosis in a single location were simulated. It is determined that the atherosclerotic plaque at one location can significantly increase the possibility of atherosclerotic plaque at another location. Thus, cases with multiple stenoses must also be simulated.

References

- Avolio, A.P., 1980, Multi-branched model of the human arterial system, *Med. & Biol. Eng. & Comput.*, 18, 709-718.
- Bark, D.L., Ku, D.N., 2010, Wall shear over high degree stenoses pertinent to atherothrombosis, *Journal of Biomechanics*, 43 (15), 2970-2977.
- Caro, C.G., Fitz-Gerald, J.M., Schroter, R.C., 1969. Arterial wall shear and distribution of early atheroma in man. *Nature*. 223, 1159-1160.
- Caro, L.G., Fitz-Gerald J.M., Schroter, R.C., 1971. Atheroma and arterial wall shear: observation, correlation and proposal of a shear dependent mass transfer mechanism, for atherogenesis. *Proc. R. Soc. London B*. 177:109–59.
- Conlon, M. J., Russell, D.L., Mussivand, T., 2006. Development of a Mathematical Model of the Human Circulatory System. *Ann. Biomed. Eng.* 34, 1400–1413.
- Dabagh, M., Jalali, P., Konttinen, Y.T., Sarkomaa, P., 2008. Distribution of Shear Stress over Smooth Muscle Cells in Deformable Arterial Wall. *Med. Biol. Eng. Comput.* 46, 649-57.
- Dabagh, M., Jalali, P., Tarbell, J.M., 2009. The transport of LDL across the deformable arterial wall: the effect of endothelial cell turnover and intimal deformation under hypertension. *Am. J. Phys.: Heart & Circ. Phys.* 297: H983-H996.
- DeBakey, M.E., Lawrie, M.G., Glaeser, D.H., 1985. Patterns of atherosclerosis and their surgical significance. *Annals of Surgery*, 201, 115–131.
- Floc'h, S. L., Cloutier, G., Finet, G., Tracqui, P., Pettigrew, R.I., Ohayon, J., 2010., On the potential of a new IVUS elasticity modulus imaging approach for detecting vulnerable atherosclerotic coronary plaques: *in vitro* vessel phantom study, *Phys. Med. Biol.* 55, 5701–5721.
- Fry, D.L., 1968. Acute Vascular Endothelial Changes Associated with Increased Blood Velocity Gradients. *Circ. Res.* 22, 165-197.
- Fry, D.L., 1969. Certain Chemorheologic Considerations Regarding the Blood Vascular Interface with Particular Reference to Coronary Artery Disease. *Circulation*. 40, IV-38.

- Friedman, M.H., Geometric risk factors for arteriosclerosis. 1983. *Arteriosclerosis*, 4, 85–94.
- Friedman, M.H., Deters, O.J., 1987. Correlation among shear rate measures in vascular flows. *J. Biomech. Eng.*, 109, 25–26.
- Fung, Y.C., 1996. *Biomechanics: Circulation*. Springer-Verlag, New York.
- Gao, F., Guo, Z., Sakamoto, M., Matsuzawa, T., 2006. Fluid-structure Interaction within a Layered Aortic Arch Model. *J. Biol. Phys.* 32, 435-454.
- Gharib, G., and Beizaie, M., 2003. Correlation Between Negative Near-Wall Shear Stress in Human Aorta and Various Stages of Congestive Heart Failure, *Annals of Biomedical Engineering*, 31(6), 678-685.
- Hoogstraten, H. W., Kootstra, J. G., Hillen, B., Krijger, J. K. B., Wensing, P. J. W., 1996. Numerical simulation of blood flow in an artery with two successive bends. *Journal of Biomechanics*, 29, 1075 –1083.
- Huang, R. F., Yang, T. F., Lan, Y.K., 2010. Pulsatile flows and wall shear stresses in models simulating normal and stenosed aortic arches. *Exp Fluids*, 48, 497–508.
- Ishikawa, T., Guimaraes, L. F., Oshima, S., Yamane, R., 1998. Effect of non-Newtonian property of blood on flow through a stenosed tube, *Fluid Dynamics Research*, 22, 251–264.
- Kamiya, A. and Togawa, T., 1972. Optimal branching structure of the vascular tree. *Bull Math Biophys.* 34(4), 431-8.
- Khanfar, K. M., Gadhoke, P., Berguer, R., Bull, J. L., 2006. Modeling pulsatile flow in aortic aneurysms: Effect of non-Newtonian properties of blood. *Biorheology*, 43, 661-679.
- Khodadai, J. M., Vlachos, N.S., Liepsch, D., LDA measurements and numerical prediction of pulsatile laminar flow in a plane 90-degree bifurcation. *Journal of Biomechanical Engineering*, 110 (2), 129-136.
- Kilner, P.J., Yang, G.Z., Mohiaddin, R.H., Firmin, D.N., Longmore, D.B., 1993. Helical and retrograde secondary flow patterns in the aortic arch studied by three-directional magnetic resonance velocity mapping. *Circulation*. 88, 2235-2247.

- Kim, H. J., Vignon-Clementel, I. E., Figueroa, C.A., LaDisa, J.F., Jansen, K.E., Feinstein, J.A., Taylor, C.A., 2009. On coupling a lumped parameter heart model and a three-dimensional finite element aorta model. *Annals of Biomedical Engineering*, 37 (11), 2153–2169.
- Kim, T., Cheer, A.Y, Dwyer H.A., 2004. A simulated dye method for flow visualization with a computational model for blood flow. *J. Biomech.* 37, 1125–1136.
- Ku, D.N., 1997. Blood flow in arteries. *Annual Review of Fluid Mechanics*. 29, 399–434.
- Ku, D.N., Giddens, D.P., Zarins, C.K., Glagov, S., 1985. Pulsatile flow and atherosclerosis in the human carotid bifurcation: positive correlation between plaque location and low and oscillating shear stress. *Arteriosclerosis*. 5, 293–302.
- Ku, D.N., Lipsch, D., 1986. The effects of non-newtonian viscoelasticity and wall elasticity on flow at a 90-degree bifurcation. *Biorheology*. 23, 359–370.
- Lam, S. K., Fung, G. S. K., Cheng S. W. K., Chow, K. W., 2008. Blood flow and macromolecular transport in curved blood vessels. *Applied Mathematics and Mechanics* 27, 1223–1231.
- Lee, S.E., Lee Sang-Wook, Fischer P.F., Bassiouny, S.B., Loth, F., 2008. Direct numerical simulation of transitional flow in a stenosed carotid bifurcation, *Journal of Biomechanics*, 41, 2551–2561
- Li, J.K-J., 2004. *Dynamics of the vascular system*. World Scientific Publishing Co., Singapore.
- Lipsch, D., 1986. Flow in tubes and arteries – a comparison. *Biorheology*. 23, 395–433.
- Liu, X., Fan, Y, Deng, X., 2010. Effect of spiral flow on the transport of oxygen in the aorta: a numerical study. *Annals of Biomedical Engineering*, 38 (3), 917–926.
- Lu, X., Yang, J., Zhao, J. B., Gregersen, H., Kassab, G. S., 2003, Shear modulus of porcine coronary artery: contributions of media and adventitia, *Am J Physiol Heart Circ Physiol*, 285, H1966–H1975.

- Matthys, K.S., Alastruey, J., Peiro' J., Khir, A.W., Segers, P., Verdonck, P.R., Parker, K.H., Sherwin, J.S., 2007, Pulse wave propagation in a model human arterial network: Assessment of 1-D numerical simulations against in vitro measurements, *Journal of Biomechanics*, 40, 3476–3486.
- Mitchell, J. R. A., and Schwartz, C. J. 1965. *Arterial Disease*. Blackwell Scientific Publications: Oxford.
- Michael Schachter 1997. The pathogenesis of atherosclerosis. *International Journal of Cardiology*, 62, S3-S7.
- Moayeri, M. S., Zendehebudi, G. R., 2003. Effect of elastic property of the wall on flow characteristics through arterial stenosis, *Journal of Biomechanics*, 36, 525-535.
- Mori, D., Yamaguchi, T., 2002, Construction of the CFD Model of the Aortic Arch based on MR Images and Simulation of the Blood Flow. *MIAR 2001*, 111-116.
- Morris, L., Delassus, P., Callanan, A., Walsh, M., Wallis, F., Grace, P., McGloughlin, T., 2005. 3-D numerical simulation of blood flow through models of the human aorta. *J. Biomech. Eng.* 127, 767-775.
- Mustapha, N., Mandal, P.K., Johnston, P.R., Amin, N., 2010. A numerical simulation of unsteady blood flow through multi-irregular arterial stenoses. *Applied Mathematical Modeling*. 34, 1559-1573.
- Myers, J.G., Moore, J.A., Ojha, M., Johnston, K.W., Ethier, C.R., 2001. Factors Influencing Blood Flow Patterns in the Human Right Coronary Artery. *Ann. Biomed. Eng.* 29, 109-120.
- Nakamura, M., Wada, S., Yamaguchi, T., 2006. Computational Analysis of blood Flow in an Integrated Model of the Left Ventricle and the Aorta. *J. Biomech. Eng.* 128, 837-843.
- Nerem, R. 1995. Atherosclerosis and the role of wall shear stress. In *Flow Dependent Regulation of Vascular Function*, ed. JA Bevan, G Kaley, GM Rubany. New York: Oxford Univ. Press.
- Ohayon, J., Finet, G., Gharib A. M., Herzka, D. A., Tracqui, P., Heroux, J., Rioufol G., Kotys, M. S., Elagha, A., Pettigrew, R. I., 2008. Necrotic core thickness and positive arterial remodeling index: emergent biomechanical

- factors for evaluating the risk of plaque rupture, *Americal Journal of Physiology-Heart and Circulatory Physiology* 295 (2), H717-H727.
- Padmanabhan, N., Swirling flow of a fluid in a straight tube, 1984, *Indian Journal of Pure and applied mathematics*. 8, 943-950.
- Park, Y.J., Park, C.Y., Kwang, C.M., Sun, K., Min, B.G., 2007. Pseudo-organ boundary conditions applied to a computational fluid dynamics model of the human aorta. *Comput. Biol. Med.* 37, 1063-1072.
- Padley, T.J., 2007. *The fluid mechanics of large blood vessels*. Cambridge University Press, Cambridge.
- Pekkan, K., Dasi, L.P., Nourparvar, P., Yerneni, S., Tobita, K., Fogel, M.A., Keller, B., Yoganathan, A., 2008. In vitro hemodynamic investigation of the embryonic aortic arch at late gestation, *Journal of Biomechanics*, 41, 1697–1706.
- Prahlad R.N., Schultz D. H., 2004. Modeling of arterial stenosis and its application to blood diseases, *Mathematical Bioscience*, 190, 203–220.
- Raines, E. W., Ross, R., 1993. Smooth muscle cells and pathogenesis of the lesions of Atherosclerosis, *Br. Heart J.* 69, S30-S37.
- Ross, R., 1993. Atherosclerosis: a defense mechanism gone awry. *Am. J. Pathol.* 143, 987-1002.
- Seed, W.A., Wood, N.B., 1971. Velocity patterns in the aorta. *Cardiovasc Research*.5, 319-30.
- Shahcheraghi, N., Dwyer, H. A., Cheer, A.Y., Barakat A.I., Rutaganira, T., 2002. Unsteady and three-dimensional simulation of blood flow in the human aortic arch. *J. Biomech. Eng.* 124, 378–387.
- Smedby, Ö., 1996. Geometric risk factors for atherosclerosis in the aortic bifurcation: a digitized angiography study. *Annals of Biomedical Engineering*, 24 (2), 481–482.
- Tarbell, J.M., 2003. Mass transport in arteries and the localization of atherosclerosis. *Annu. Rev. Biomed. Eng.* 5, 79–118.
- Taylor, C.A., Huges, T.J., Zarins, C.K., 1998. Finite Element Modeling of Three-Dimensional Pulsatile Flow in the Abdominal Aorta: Relevance to Atherosclerosis, *Annals of Biomedical Engineering*, Vol. 26, pp. 975–987

- Texon, M., 1986. The hemodynamic basis of atherosclerosis. Further observations: the ostial lesion. *Bulletin of the New York Academy of Medicine*, Vol. 48 (5), pp 733-740.
- Towfiq, B., Weir, J., Rawles, J., 1986. Effect of age and blood pressure on aortic size and stroke distance. *Br. Heart. J.* 55, 560–564.
- Utepov, Y.Y., 1997. Correlation between anatomic parameters of the aorta and manifestations of atherosclerosis. *Bulletin of Experimental Biology and Medicine* 124, 729-734.
- Valencia, V., Baeza, F., 2009. Numerical simulation of fluid-structure interaction in stenotic arteries considering two layer nonlinear anisotropic structural model. *International Communications in Heat and Mass Transfer* 36, 137-142.
- Van de Vosse, F. N., Mathematical modeling of the cardiovascular system, 2003, *Journal of Engineering Mathematics* 47: 175–183.
- Vasava, P., Dabagh, M., Jalali, P., 2008. Pulsatile blood flow simulations in aortic arch: Effects of blood pressure and the geometry of arch on wall shear stress. *IFMBE proceedings*, 22, 1926-1929.
- Vasava, P., Dabagh, M., Jalali, P., 2009. Effect of aortic arch geometry on pulsatile blood flow: Flow pattern and wall shear stress. *IFMBE proceedings*, 25, 1198-1201.
- Vasava, P., Dabagh, M., Jalali, P., 2009. Computational study of pulsatile blood flow in aortic arch: Effect of blood pressure. *IFMBE proceedings*, 25, 1206-1209.
- Vasava, P., Dabagh, M., Jalali, P., Kolari, P., 2011. Finite Element Modeling of pulsatile blood flow in idealized model of human aortic arch: The study of hypotension and hypertension, *Computational and Mathematical Methods in Medicine*, *Article in the press*.
- Wang, H. H., 2001. Analytical models of Atherosclerosis. *Atherosclerosis* 159, 1–7.
- Wei, L., Wen, G., Tan, W., 2006. Blood flow and macromolecular transport in curved blood vessels. *Applied Mathematics and Mechanics* 27, 1223–1231.

- Wen, C. Y., Yang, A. S, Tseng, L.Y., Chai, J.W., 2010. Investigation of pulsatile flowfield in healthy thoracic aorta models. *Annals of Biomedical Engineering*, 38 (2), 391–402.
- Zamir, M., 1976. The role of shear forces in arterial branching. *J. Gen. Physiol.* 67, 213-222.
- Zarins, C:K., Giddens, B. K., Bharadvaj, B. K., Sottiurai, V. S., Mabon, R. F., Glagov, S., Carotid bifurcation atherosclerosis: Quantitative correlation of plaque localization with flow velocity profiles and wall shear stress. *Circulation Research*53, 502–514.
- Zeng, D., Boutsianis, E., Ammann, M., Boomsma, K., Wildermuth, S., Poulikakos, D., 2008. A study on the compliance of a right coronary artery and its impact on wall shear stress, *Journal of Biomechanical Engineering*, 130(4), 0410141-04101411.
- Zhao, S.Z., Xu, X.Y., Hughes, A.D., Thom, S.A., Stanton, A.V., Ari, B., Long, Q., 2000. Blood flow and vessel mechanics in a physiologically realistic model of a human carotid arterial bifurcation, *Journal of Biomechanics*, 33, 975-984.

ACTA UNIVERSITATIS LAPPEENRANTAENSIS

- 423. PEKKARINEN, SATU. Innovations of ageing and societal transition. Dynamics of change of the socio-technical regime of ageing. 2011. Diss.
- 424. JUNTILLA, VIRPI. Automated, adapted methods for forest inventory. 2011. Diss.
- 425. VIRTÄ, MAARIT. Knowledge sharing between generations in an organization – Retention of the old or building the new 2011. Diss.
- 426. KUITTINEN, HANNA. Analysis on firm innovation boundaries. 2011. Diss.
- 427. AHONEN, TERO. Monitoring of centrifugal pump operation by a frequency converter. 2011. Diss.
- 428. MARKELOV, DENIS. Dynamical and structural properties of dendrimer macromolecules. 2011. Diss.
- 429. HÄMÄLÄINEN, SANNA. The effect of institutional settings on accounting conservatism – empirical evidence from the Nordic countries and the transitional economies of Europe. 2011. Diss.
- 430. ALAOUTINEN, SATU. Enabling constructive alignment in programming instruction. 2011. Diss.
- 431. ÅMAN, RAFAEL. Methods and models for accelerating dynamic simulation of fluid power circuits. 2011. Diss.
- 432. IMMONEN, MIKA. Public-private partnerships: managing organizational change for acquiring value creative capabilities. 2011. Diss.
- 433. EDELMANN, JAN. Experiences in using a structured method in finding and defining new innovations: the strategic options approach. 2011. Diss.
- 434. KAH, PAUL. Usability of laser - arc hybrid welding processes in industrial applications. 2011. Diss.
- 435. OLANDER, HEIDI. Formal and informal mechanisms for knowledge protection and sharing. 2011. Diss.
- 436. MINAV, TATIANA. Electric drive based control and electric energy regeneration in a hydraulic system. 2011. Diss.
- 437. REPO, EVELIINA. EDTA- and DTPA-functionalized silica gel and chitosan adsorbents for the removal of heavy metals from aqueous solutions. 2011. Diss.
- 438. PODMETINA, DARIA. Innovation and internationalization in Russian companies: challenges and opportunities of open innovation and cooperation. 2011. Diss.
- 439. SAVITSKAYA, IRINA. Environmental influences on the adoption of open innovation: analysis of structural, institutional and cultural impacts. 2011. Diss.
- 440. BALANDIN, SERGEY, KOUCHERYAVY, YEVGENI, JÄPPINEN, PEKKA, eds. Selected Papers from FRUCT 8 .2011.
- 441. LAHTI, MATTI. Atomic level phenomena on transition metal surfaces. 2011. Diss.
- 442. PAKARINEN, JOUNI. Recovery and refining of manganese as by-product from hydrometallurgical processes. 2011. Diss.
- 443. KASURINEN, JUSSI. Software test process development. 2011. Diss.

- 444. PEKKANEN, PETRA. Delay reduction in courts of justice – possibilities and challenges of process improvement in professional public organizations. 2011. Diss.
- 445. VANHALA, MIKA. Impersonal trust within the organization: what, how, and why? 2011. Diss.
- 446. HYNYNEN, KATJA. Broadband excitation in the system identification of active magnetic bearing rotor systems. 2011. Diss.
- 447. SOLONEN, ANTTI. Bayesian methods for estimation, optimization and experimental design. 2011. Diss.
- 448. JABLONSKA, MATYLDA. From fluid dynamics to human psychology. What drives financial markets towards extreme events. 2011. Diss.
- 449. MYÖHÄNEN, KARI. Modelling of combustion and sorbent reactions in three-dimensional flow environment of a circulating fluidized bed furnace. 2011. Diss.
- 450. LAATIKAINEN, MARKKU. Modeling of electrolyte sorption – from phase equilibria to dynamic separation systems. 2011. Diss.
- 451. MIELONEN, JUHA. Making Sense of Shared Leadership. A case study of leadership processes and practices without formal leadership structure in the team context. 2011. Diss.
- 452. PHAM, ANH TUAN. Sewage sludge electro-dewatering. 2011. Diss.
- 453. HENNALA, LEA. Kuulla vai kuunnella – käyttäjää osallistavan palveluinnovoinnin lähestymistavan haasteet julkisella sektorilla. 2011. Diss.
- 454. HEINIMÖ, JUSSI. Developing markets of energy biomass – local and global perspectives. 2011. Diss.
- 455. HUJALA, MAIJA. Structural dynamics in global pulp and paper industry. 2011. Diss.
- 456. KARVONEN, MATTI. Convergence in industry evolution. 2011. Diss.
- 457. KINNUNEN, TEEMU. Bag-of-features approach to unsupervised visual object categorisation. 2011. Diss.
- 458. RUUSKANEN, VESA. Design aspects of megawatt-range direct-driven permanent magnet wind generators. 2011. Diss.
- 459. WINTER, SUSANNA. Network effects: scale development and implications for new product performance. 2011. Diss.
- 460. JÄÄSKELÄINEN, ANSSI. Integrating user experience into early phases of software development. 2011. Diss.
- 461. KÄÄRIÄINEN, TOMMI. Polymer surface modification by atomic layer deposition. 2011. Diss.
- 462. KOCHURA, ALEKSEY. Growth, magnetic and transport properties of InSb and II-IV-As₂ semiconductors doped with manganese. 2011. Diss.
- 463. PUTKIRANTA, ANTERO. Possibilities and challenges of longitudinal studies in operations management. 2011. Diss.
- 464. HAPPONEN, ARI. Muuttuvaan kysyntään sopeutuva varastonohjausmalli. 2011. Diss.

